Novel, High Activity Hydroprocessing Catalysts:

Iron Group Phosphides

Xianqin Wang

Dissertation submitted to the Virginia Polytechnic Institute and State University in partial fulfillment of the requirements for the degree of

Doctor of Philosophy
in
Chemical Engineering

S. Ted Oyama, Chairman
David F. Cox
Ravi F. Saraf
Brian E. Hanson
Paul A. Deck

March 21, 2002
Blacksburg, Virginia

Keywords: Iron group phosphide, Phosphorus effect, Structure-sensitivity, EXAFS, Hydrodesulfurization, Hydrodenitrogenation, Hydrodenitrogenation mechanism.

Novel, High Activity Hydroprocessing Catalysts:
Iron Group Phosphides

by

Xianqin Wang

Committee Chairman: S Ted Oyama

Chemical Engineering

Abstract

A series of iron, cobalt and nickel transition metal phosphides was synthesized by means of temperature-programmed reduction (TPR) of the corresponding phosphates. The same materials, Fe_2P, CoP and Ni_2P, were also prepared on a silica (SiO_2) support. The phase purity of these catalysts was established by x-ray diffraction (XRD), and the surface properties were determined by N_2 BET specific surface area (S_g) measurements and CO chemisorption. The activities of the silica-supported catalysts were tested in a three-phase trickle bed reactor for the simultaneous hydrodenitrogenation (HDN) of quinoline and hydrodesulfurization (HDS) of dibenzothiophene using a model liquid feed at realistic conditions (30 atm, 370 ^{o}C). The reactivity studies showed that the nickel phosphide (Ni_2P/SiO_2) was the most active of the catalysts. Compared with a commercial Ni-Mo-S/γ-Al_2O_3 catalyst at the same conditions, Ni_2P/silica had a substantially higher HDS activity (100 % vs. 76 %) and HDN activity (82 % vs. 38 %).

Because of their good hydrotreating activity, an extensive study of the preparation of silica supported nickel phosphides, Ni_2P/SiO_2, was carried out. The parameters investigated were the phosphorus content and the weight loading of the active phase. The most active composition was found to have a starting synthesis Ni/P ratio close to 1/2, and the best loading of this sample on silica was observed to be 18 wt.%.

Extended x-ray absorption fine structure (EXAFS) and x-ray absorption near edge spectroscopy (XANES) measurements were employed to determine the structures of the supported samples. The main phase before and after reaction was found to be Ni_2P, but some sulfur was found to be retained after reaction.

A comprehensive scrutiny of the HDN reaction mechanism was also made over the Ni_2P/SiO_2 sample (Ni/P = 1/2) by comparing the HDN activity of a series of piperidine derivatives of different structure. It was found that piperidine adsorption involved an α-H activation and nitrogen removal proceeded mainly by means of a β-H activation though an elimination (E2) mechanism. The relative elimination rates depended on the type and number of β-hydrogen atoms. Elimination of β-H atoms attached to tertiary carbon atoms occurred faster than those attached to secondary carbon atoms. Also, the greater the number of the β-H atoms, the higher the elimination rates. The nature of the adsorbed intermediates was probed by Fourier transform infrared spectroscopy (FTIR) and temperature-programmed desorption (TPD) of the probe molecule, ethylamine. This measurement allowed the determination of the likely steps in the hydrodenitrogenation reaction.

Acknowledgements

I would like to thank my parents, Zhaolan and Yongxiang, my brothers and sisters, Xianyi, Xianlian, Xianzi, Xianqun and Xianqiao, and my husband Jiangbo Dang, for their love and support.

I would like to express my sincere gratitude to my advisor, Professor S. Ted Oyama for his wise and patient supervision, and his endeavor in teaching me how to think and how to work. I will always respect his hard work and enormous knowledge.

I would like to thank my committee members, Professors David F. Cox, Ravi F. Saraf, Brian E. Hanson and Paul A. Deck for their time and guidance.

I would like to thank Dr. Felix Requejo for his collaboration with the EXAFS experimental and analysis.

I also would like to thank past and current group members, Mark Abee, Juan Jose Bravo, Chad Byrd, Paul Clark, Doohwan Lee, Yongkul Lee, Wei Li, Rakesh Radhakrishnan, Corey Reed, Viviane Schwarz, Todd St. Clair, and Wangjae Chun, for their support and companionship. I especially appreciate the close cooperation with Paul Clark and Yongkul Lee.

Table of Contents

Chapter 1. Introduction

Chapter 2. Synthesis, Characterization and Hydrotreating Activity of Several Iron Group Transition Metal Phosphides

2.2. Experimental

2.3. Results and Discussion

Chapter 3. XAFS Studies of the Effect of Phosphorus Content in Nickel Phosphide Catalysts

5.4. Discussions

List of Tables

List of Figures

List of Schemes

Chapter 1

Introduction

1.1 Motivation

Demands for a cleaner environment have led to a global tightening in the allowed sulfur content in fuels and increased restrictions on the release of nitrogen oxides. For example, in the case of sulfur the U.S. Environmental Protection Agency (EPA) has issued regulations that would lower its allowed content in diesel fuel from the current 500 ppmw to 15 ppmw in 2006, and in gasoline from 300 ppmw to 30 ppmw by 2004 (1,2). For this reason there are considerable efforts being expended to develop new technologies for the production of clean fuels, like adsorption, extraction, oxidation, alkylation, and bioprocessing (3). Currently, however, hydroprocessing appears to be the technologically preferred solution (3). Hydroprocessing refers to a variety of catalytic hydrogenation processes that saturate heteroatomatic rings and remove S, N, O and metals from different petroleum streams in a refinery (4). Because of the tighter environmental regulations new types of catalysts, which are economic, have long-life, and possess high activity are highly desired. In this work we present results on a new type of hydroprocessing catalyst: transition metal phosphides.

1.2 Introduction to iron group phosphides

Iron group phosphides, a series of transition metal phosphides, are investigated in this study. Unit cell and space group data of this group phosphides are listed in Table 1.1. All of these materials have similar properties and are usually characterized by their hardness, very high melting point, high thermal and electrical conductivity, and resistance to chemical attack. The preparation method and detail properties of transition metal phosphides have been reviewed (5,6,7,8,9).

Table 1.1. Unit cell and space group data of iron group phosphides

Metal	Phos-phide	Crystal system	Structure type	Space group	Unit cell dimensions (Å)				Ref.
					a	b	c	z	
Fe	Fe_3P	tetragonal		$I\bar{4}$	9.1	9.1	4.459	8	10
	Fe_2P	hexagonal	C22	P62m	5.865	5.865	3.456	3	11
	Fe_2P	orthorhombic	C23	Pnma	5.775	3.571	6.641	-	12
	FeP	orthorhombic	B31	Pnma	5.191	3.099	5.792	4	13
	FeP	orthorhombic	AsCo	$Pna2_1$	5.193	5.792	3.099	4	14
	FeP_2	orthorhombic	C18	Pnnm	4.973	5.657	2.725	2	15
Co	Co_2P	orthorhombic	C23	Pnma	5.634	3.505	6.601	4	16
	CoP	orthorhombic	B31	Pnma	5.077	3.281	5.587	4	17
	CoP_2	monoclinic	$CoSb_2$	P21/c	5.610	5.591	5.643	4	18
Ni	Ni_3P	tetragonal		I4	8.952	8.952	4.388	8	19
	$Ni_{12}P_5$	-	$Ni_{12}P_5$	I4/m	8.646	8.646	5.070	2	19
	Ni_7P_3	cubic	-		8.64	-	-	6	20
	Ni_2P	hexagonal	C22	P62m	5.859	5.859	3.382	3	20
	Ni_2P		Ni_2P	P321	5.865	5.865	3.387	-	21
	Ni_5P_4	hexagonal		P63mc	6.789	6.789	10.986	4	22
	NiP	orthorhombic	NiP	Pbca	6.05	4.88	6.89	8	23
	NiP_2	monoclinic	PdP_2	C2/c	6.366	5.615	6.071	4	24
	NiP_2		FeS_2	$Pa\bar{3}$	5.471	-	-	-	25

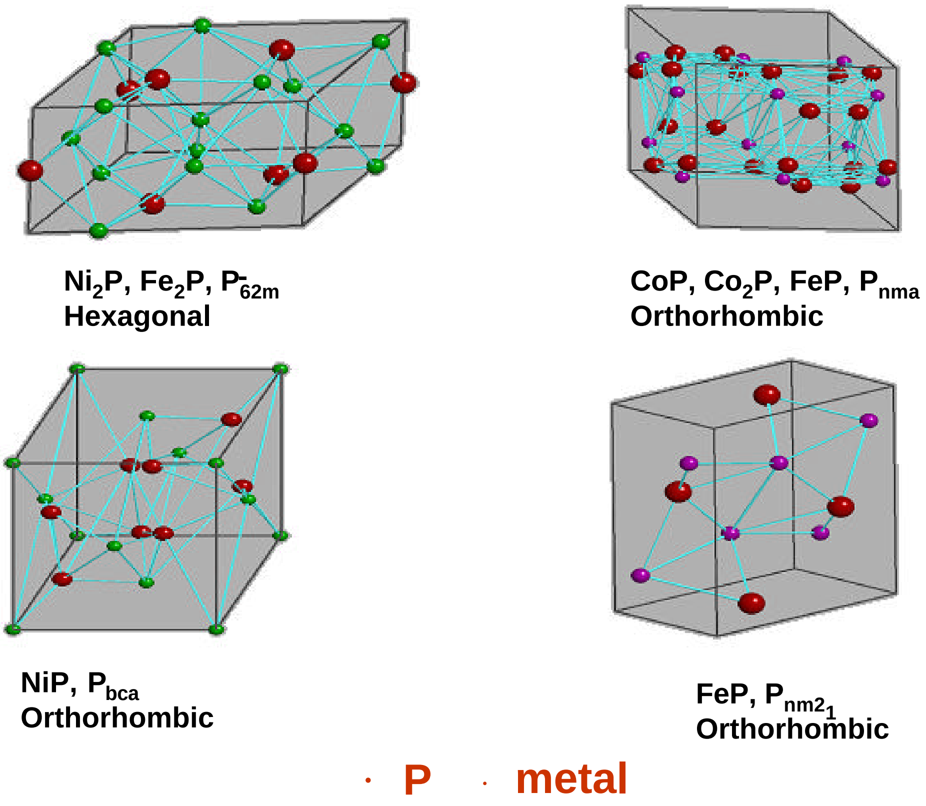

Ni_2P, Fe_2P, $P_{\bar{6}2m}$
Hexagonal

CoP, Co_2P, FeP, P_{nma}
Orthorhombic

NiP, P_{bca}
Orthorhombic

FeP, P_{nm2_1}
Orthorhombic

Figure 1.1. Crystal structures of several iron group phosphides

Crystal structures of some iron group phosphides with metal to phosphorous of 1/1, and 2/1 are shown in Figure 1.1. The compounds, Ni_2P and Fe_2P, share the same hexagonal structure with space group P_{62m}. All others have orthorhombic unit cells with different space groups.

1.3 Organization of thesis

This dissertation reports the synthesis and application of a new series of hydroprocessing catalysts, iron group phosphides. These compounds were prepared in bulk and supported forms by the method of temperature programmed reduction (TPR).

The mechanism of hydrodenitrogenation reactions on Ni_2P/SiO_2 was studies by comparing the reactivities of different methyl piperidines with different numbers of α and β hydrogens.

Chapter 1 presents a description of the motivation of the work, which is the study of new catalysts for hydroprocessing. The chapter gives a brief introduction to the crystal structures and properties of the materials.

Chapter 2 presents the synthesis, characterization and hydrotreating activity of several iron group transition metal phosphides. In this chapter, a series of bulk and silica supported iron, cobalt and nickel metal phosphides were synthesized by means of temperature-programmed reduction (TPR) of the corresponding phosphates. The activity of the silica-supported catalysts in hydrodenitrogenation (HDN) and hydrodesulfurization (HDS) was evaluated with a model feed liquid.

Chapter 3 reports the effect of P content on the structure and hydroprocessing activity of NiP_x/SiO_2 catalysts. A series of these novel catalysts with different Ni/P ratios were synthesized and characterized by BET surface area determinations, CO uptake titrations, x-ray diffraction (XRD) analysis, and extended x-ray absorption fine structure (EXAFS) measurements. The activity and stability of the catalysts were affected profoundly by the phosphorus content, both reaching a maximum at a sample starting synthesis P/Ni ratio of about 2/1.

Chapter 4 presents the effect of Ni_2P loading on the structure and activity of Ni_2P/SiO_2 catalysts. The performance of the catalysts was found to go through a maximum with loading level.

Chapter 5 presents the results of a detailed study of the mechanism of HDN using a series of piperidine and its derivatives on a Ni_2P/SiO_2 (Ni/P=1/2) catalyst. The nature of the intermediates on the catalyst was characterized by temperature programmed desorption (TPD) of the probe molecule ethylamine and diffuse-reflectance Fourier transform infrared spectroscopy (FTIR).

Chapter 6 presents the general conclusions of the work.

---

1. US Environmental Protection Agency, *Press Release*, May 1, 1999; December 21, 2000.
2. Federal Register, Vol. 65, No. 28, Thursday, Feb. 10, 2000.
3. O'Connor, P. and Mayo, S., *Preprints, Div. Fuel Chem.* **46**, 381 (2001).
4. Topsøe, H., Clausen B. S., Massoth F. E., "Hydrotreating Catalysis, Science and Technology, (Anderson, J. R. and Boudart, M., Eds.), Catalysis-Science and technology", Vol.11, Springer-Verlag, New York, 1991
5. Aronsson, B., Lundström, T, and Rundquist, S., "Borides, Silicides and Phosphides" John Wiley and Sons, London, U.K. (1965).

---

6. Toy, A. D. F., Phosphorus, *in* “Comprehensive Inorganic Chemistry” Chapter 20 (Bailar, J. C., Emeléus, H. J., Nyholm, R., and Trotman-Dickenson, A. F., Eds.) Pergamon Press, Oxford, UK (1973).
7. Corbridge, D. E. C., “Phosphorus: Studies in Inorganic Chemistry” Vol. 10, p. 71 Elsevier Press (1990).
8. Corbridge, D. E. C., Pearson, M. S., and Walling, C., “Topics in Phosphorus Chemistry”, Vol. 3, p.123, Wiley, NY (1966).
9. Clark, P., “New catalysts for hydroprocessing: molybdenum and tungsten phosphide”, Ph.D. Dissertation, 2000, Virginia Polytechnic Institute and State University.
10. Rundqvist, S., Acta Chem. Scand., 16, 1 (1962)
11. Carlson, B., et al., J. Solid State Chem., 8, 57 (1973)
12. Senateur, J. P., Rouault, A., Fruchart, R., Capponi, J. J., Peroux, M., Materials Research Bulletin, 11, 631 (1976)
13. Rundqvist, S., Acta Chem. Scand., 16, 287 (1962)
14. Sete, K., Kjekshus, A., Acta Chem. Scand., 26, 1276 (1972)
15. Holseth, H., Kjekshus, A., Acta Chem. Scand., 22, 3273 (1968)
16. Roger, A., Sénateur, J. P., Fruchart, R., Annal. Chim., Paris, 4, 79 (1969)
17. Rundqvist, S., Acta Chem. Scand., 16, 287 (1962)
18. Donohue, P. C., Mater. Res. Bull., 7, 943 (1972)
19. Rundqvist, S., Hassler, E., Lundvik, L., Acta Chem. Scand., 16(1), 242 (1962)
20. Nowotny, H., Z. Phys. Chem., 40, 281 (1938)
21. Rundqvist, S., Acta Chem. Scand., 16, 992 (1962)

---

22. Elfström, M., Acta Chem. Scand., 19, 1694 (1965)

23. Larson, E., Ark. Kemi, 23(32), 335 (1965)

24. Rundqvist, S., Acta Chem. Scand., 15, 451 (1961)

25. Donohue, P. C., Bither, T. A., Young, H. S., Inorganic Chemistry, 7(5), 998 (1968)

Chapter 2

Synthesis, Characterization and Hydrotreating Activity of Several Iron Group Transition Metal Phosphides

2.1 Introduction

Transition metal phosphides have attracted considerate interest for some time because these materials are technologically important as semiconductors, luminescent devices, and electronic components (1). A brief thermodynamic analysis of the potential stability in H_2S was carried out early in 1975 (2), and it was revealed that this group of materials is potentially stable and sulfur-resistant. However, the transition metal phosphides as a class of materials have received little attention as catalysts. This is probably because the development of synthetic methods of producing materials with a high surface area was not achieved.

The combination of the iron group metals Co and Ni with Mo and W in commercial hydroprocessing catalysts (3,4,5) and the use of phosphorus as a promoter (6,7,8) is well known. Many workers have studied the effect of phosphorus in sulfide catalysts (9,10,11,12), and the topic was reviewed by Iwamoto and Grimblot (13). In these materials, the phosphorus was found as a phosphate and primarily modified the properties of the support, only indirectly influencing the active phase. For example, phosphorus altered the acid-base character of alumina and improved dispersion of molybdenum on the support. It also enhanced the solubility of the precursor metals in the preparation stages and allowed the synthesis of high-loading catalysts (14). The effect of phosphorus strongly depended on its content, with an effect that was usually negative at high loadings. Phosphorus showed no effect or a small positive effect on the hydrodesulfurization (HDS) of thiophene, and a positive effect on the hydrodenitrogenation (HDN) of quinoline (15), pyridine (16), and piperidine (7). Notwithstanding considerable studies on promoter effects, until recently phosphorus compounds in the form of phosphides had not been examined in the hydroprocessing field. The first report of the use of the iron group metal phosphides as hydrodenitrogenation catalysts was by Robinson, et al. (17), who prepared Co_2P and Ni_2P on silica, alumina and carbon. They reported that carbon and silica were the best supports and that Ni_2P, in particular was very effective in HDN. These studies were carried out at high conversion, and an assessment of the intrinsic activity is not possible. The first studies on Mo and W phosphides were carried out by Li et al. (18, 19) and Clark et al. (20) who reported good activity for HDS and HDN. Studies in the Prins group (21) confirmed the activity in HDN, and in a recent comparison of Co_2P, Ni_2P, MoP, CoMoP, and NiMoP (22) it was concluded that the areal activity of MoP was the highest. Earlier, the olefin hydrogenation activity of Ni_2P supported on alumina and other phosphides was explored by Nozaki and Tokumi (23,24,25). It was found that the hydrogenation activity for butadiene drastically decreased in the order of $Ni_2P > Co_2P >$ FeP. They also reported that a trace of oxygen could increase the activity of Ni_2P while lowering the activity of Ni for the butadiene hydrogenation reaction. Nickel-phosphorus alloys have been reported also in amorphous form and their activities for hydrogenation have also been studied (26,27). The amorphous alloy was prepared by an electroless plating technique from mixtures of sodium citrate, nickel sulfate, sodium hypophosphite, sodium acetate and a silica gel support, or by the chemical reduction of nickel acetate and sodium phosphate with sodium borohydride. The supported material was subjected to various treatments, including oxidation at 403 K and reduction in H_2 at 553 K. The catalyst was found to be active for the hydrogenation of nitrobenzene (28) and benzaldehyde (29), with turnover rate similar to that of Ni (1 x 10^{-3} s^{-1}). In summary, although there are some reports concerning the catalytic behavior of these phosphides, few studies have concentrated on the subject of hydrodesulfurization and hydrodenitrogenation for application in petroleum refining.

The present work presents an in-depth study of the preparation of transition metal phosphides of the iron group (Fe, Co, Ni) and their evaluation in the hydroprocessing of a model feed mixture. Initially unsupported bulk materials were prepared to provide a reference for the synthesis of supported materials. Several metal to phosphorus (M/P) ratios were explored to ascertain which stable phases could be prepared and to determine the conditions for temperature-programmed reduction. Subsequently, the preparation was extended to the supported system to obtain materials of high surface area suitable for catalytic testing. Silica was chosen as the carrier to minimize support effects and make possible the elucidation of the intrinsic catalytic activity of the phosphides.

2.2 Experimental

2.2.1 Materials

The support used in this study was a fumed silica (Cabosil, L90). The precursors for iron, cobalt and nickel were $Fe(NO_3)_3{\cdot}9H_2O$ (Aldrich, 99.99 %), $Co(NO_3)_2{\cdot}6H_2O$

(Aldrich, 99.99 %), $Ni(NO_3)_2{\cdot}6H_2O$ (Aesar,99 %), respectively, while the precursor for P was ammonium orthophosphate $(NH_4)_2HPO_4$ (Aldrich, 99 %). The chemicals utilized in the reactivity study were dibenzothiophene (Aldrich, 99.5 %), quinoline (Aldrich, 99.9 %), benzofuran (Aldrich, 99.9 %), tetralin (Aldrich, 99.5 %) and tetradecane (Jansen Chimica, 99 %). The gases employed were He (Airco, Grade 5), CO (Linde Research Grade, 99.97 %), 0.5 % O_2/He (Airco, UHP Grade), H_2 (Airco, Grade 5), N_2 (Airco, 99.99 %) and 30 % N_2/He (Airco, UHP Grade).

2.2.2 Synthesis

Unsupported bulk transition metal phosphides were prepared in two steps. In the first step, phosphate precursors were synthesized by reacting metal nitrates with ammonium phosphate, and in the second step, these phosphates were reduced to phosphides by the method of temperature-programmed reduction. Because the procedures for preparing unsupported bulk iron, cobalt and nickel phosphates were similar, the preparation of iron phosphate ($FePO_4$) will be used here to illustrate the process. First, 4.9 g (37.13 mmol) of ammonium phosphate $(NH_4)_2HPO_4$ were dissolved in 300 cm^3 of distilled water to form a transparent colorless solution, and 15 g (37.13 mmol) of iron nitrate ($Fe(NO_3)_3{\cdot}9H_2O$) were then added. The clear solution immediately turned into a light color mixture with some precipitate, but stirring resulted in the formation of a transparent solution. In the case of nickel and cobalt, several drops of nitric acid were needed to give rise to a homogenous solution. The water was then vaporized from the solution on a hot plate and the resulting paste was dried at 393 K for 3 h and calcined at

773 K for 6 h in an oven. The amount collected (with some minor losses) was 5.54 g, which corresponds to 36 mmol of iron phosphate of formula $FePO_4 \cdot H_2O$. The phosphate was then ground with a mortar and pestle and sieved to 16/20 mesh (0.65-1.2 mm diameter particles). In the second step of preparation, temperature-programmed reduction (TPR) was utilized to convert the phosphate into phosphide. The reduction was carried out in a U-shaped quartz reactor placed in a furnace controlled by a temperature programmer (Omega Model CN 2000). The temperature was raised at $\beta = 0.0167 \text{ K s}^{-1}$ (1 K min^{-1}), and was monitored by a local chromel-alumel thermocouple placed in a thermowell near the center of the reactor bed. The H_2 flow rate was set at $1000 \mu\text{mol s}^{-1}$ ($1500 \text{ cm}^3 \text{ min}^{-1}$) per gram of sample. A portion of the exit gas flow was sampled through a leak valve into a mass spectrometer (Ametek/Dycor Model MA 100) and the masses 2(H_2), 4(He), 18(H_2O), 28(N_2), 32(O_2), 34(PH_3), 15(NH), 44(CO_2), 31(P), 62(P_2) were monitored during the experiment, and these were recorded together with the temperature by an on-line computer. At the end of the temperature program, the sample was cooled in helium to room temperature, and was passivated in a 0.5 % O_2/He flow for two h.

Table 2.1: Quantities used in the preparation of supported samples

Sample	Materials used			Catalyst properties	
	Silica (g)	Metal nitrate (mol)	$(NH_4)_2HPO_4$ (mol)	Phosphide loading (wt % M_xP)	Metal loading (mol % M)
Fe_2P/SiO_2	20	0.0462	0.0231	14	11
CoP/SiO_2	20	0.0231	0.0231	9.4	6.2
Ni_2P/SiO_2	20	0.0231	0.0231	9.4	6.1

Phosphide samples supported on a silica support were prepared by modifying the two-step procedure used in the synthesis of the unsupported samples. Aqueous phosphate solutions were obtained as before and were used to impregnate silica by the incipient wetness impregnation method. The quantities used for the three supported samples are listed in Table 2.1. Prior to use, the silica was dried at 393 K for 3 h and calcined at 773 K for 6 h and was found to have an incipient wetness point of 2.2 cm^3g^{-1}. After impregnation, the powders were dried at 393 K for 3 h and calcined at 773 K for 6 h. The calcined samples were ground with a mortar and pestle, pelletized with a press (Carver, Model C) and again sieved to 16/20 mesh size. The TPR process was similar to that used for the bulk samples using the same heating rate, $\beta = 0.0167 \text{ K s}^{-1}$ (1 K min^{-1}).

2.2.3 Characterization

The synthesized materials were characterized by CO chemisorption, N_2 physisorption and x-ray diffraction (XRD) measurements. Irreversible CO uptake measurements were used to titrate the surface metal atoms and to provide an estimate of the number of active sites on the catalysts. Uptakes were obtained after passivated samples were rereduced and are denoted *ex situ* in this work. Usually, 0.2 g of sample was loaded into a quartz reactor and treated in H_2 at 723 K for 2 h. After cooling down to room temperature in He, pulses of CO in a He carrier flowing at 27 μmol s^{-1} (40 cm^3 NTP min^{-1}) were injected through a sampling valve and the 28 (CO) signal was monitored with a mass spectrometer. Uptakes of CO were also measured for the spent samples. The procedures were the same as those used for the fresh samples. Prior to the measurement, the spent samples removed from the hydrotreating reactors were washed in hexane and dried.

BET surface area measurements were carried out right after the CO uptake determinations, using a similar technique. Adsorption at liquid nitrogen temperature was performed using a 30 % N_2/He stream, and the desorption area obtained after rapid heating was compared to the area of a calibrated volume (35.4 µmol). The surface area was calculated from the one-point BET equation, which is reasonable for non-microporous materials such as those used here. X-ray diffraction (XRD) patterns of the samples were determined with a Scintag XDS-2000 powder diffractometer operated at 45 kV and 40 mA, using Cu K_α monochromatized radiation (λ = 0.154178 nm). The crystallite size of the supported samples was calculated using the Scherrer equation: $D_c = K\lambda/\beta \cos(\theta)$, where K is a constant taken as 0.9, λ is the wavelength of the x-ray radiation, β is the width of the peak at half-maximum, corrected for instrumental broadening (0.1^o), and 2θ is the Bragg angle (30,31,32). The near-surface composition of the nickel samples was obtained by x-ray photoelectron spectroscopy (XPS) (Perkin Elmer, Model 5300 with a Mg source) operated at 15 kV and 30 mA. The 285.0 eV binding energy peak of adventious carbon was used as reference. In the case of the spent catalysts, samples were removed from the reactor, washed in hexane, heated in H_2 to 673 K, and then passivated. Since the samples were exposed to the atmosphere and not sputtered, contamination by carbon from the atmosphere was present.

2.2.4 Reactivity studies

Hydrotreating activities of the samples were obtained in a three-phase trickle bed reactor for hydrodenitrogenation (HDN) and hydrodesulfurization (HDS) with a model petroleum liquid containing 2000 ppm nitrogen (quinoline), 3000 ppm sulfur (dibenzothiophene), 500 ppm oxygen (benzofuran), 20 wt.% aromatics (tetralin), and balance aliphatics (tetradecane). The operating conditions were close to industrial conditions, 3.1 MPa and 643 K with a liquid flow rate of 5 cm^3/h and a hydrogen flow rate of 100 μmol s^{-1} (150 cm^3 min^{-1}) corresponding to a gas-liquid ratio of 9800 HSCF/bl (standard antic feet H_2/barrel). The detailed description of the testing system is reported elsewhere (33). Quantities of catalysts loaded in the reactor correspond to the same amount of *ex situ* CO uptake (35 μmol). Prior to reactivity measurements, the catalyst samples were pretreated in exactly the same manner as before the *ex situ* CO uptake determinations. Hydrotreating samples were collected every two or three hours in sealed septum vials and were analyzed off-line with a gas chromatograph (Hewlett Packard, 5890A) equipped with a 0.32 mm i.d. x 50 m fused silica capillary column (CPSIL-5CB, Chrompack, Inc.) and a flame ionization detector.

2.3 Results and discussion

2.3.1 Properties and preparation of bulk phosphides

The crystal structures of the Fe, Co, and Ni phosphides are shown in Figure 2.1 and their lattice parameters are summarized in Figure 2.2. Both Fe_2P (34) and Ni_2P (35) adopt the same hexagonal structure (Space group: $P_{\bar{6}2m}$), while CoP (36) takes on an orthorhombic structure (Space group: P_{nma}). The crystal structures (Figure 2.2.1) and lattice parameters can be used to calculate the bulk density (ρ) and the surface metal atom density ($\bar{n}$) of the solids (Table 2.2). For the Fe_2P and Ni_2P samples there are 2, 3 and 2 atoms on the ac, ab and bc unit cell faces, respectively. For CoP, every unit cell face has 2 atoms.

Table 2.2: Surface metal density and bulk density of Fe_2P, CoP and Ni_2P

Sample	Lattice parameter / nm			Surface metal density / 10^{15}atoms cm^{-2}				Compound density (ρ) g cm^{-3}
	a	b	c	ab plane	bc plane	ac plane	average ($\bar{n}$)	
Fe_2P	0.5867	0.5867	0.3458	1.01	0.986	0.986	0.994	6.67
CoP	0.5077	0.3281	0.5587	1.20	1.09	0.706	0.999	6.20
Ni_2P	0.5859	0.5859	0.3382	1.01	1.01	1.01	1.01	7.09

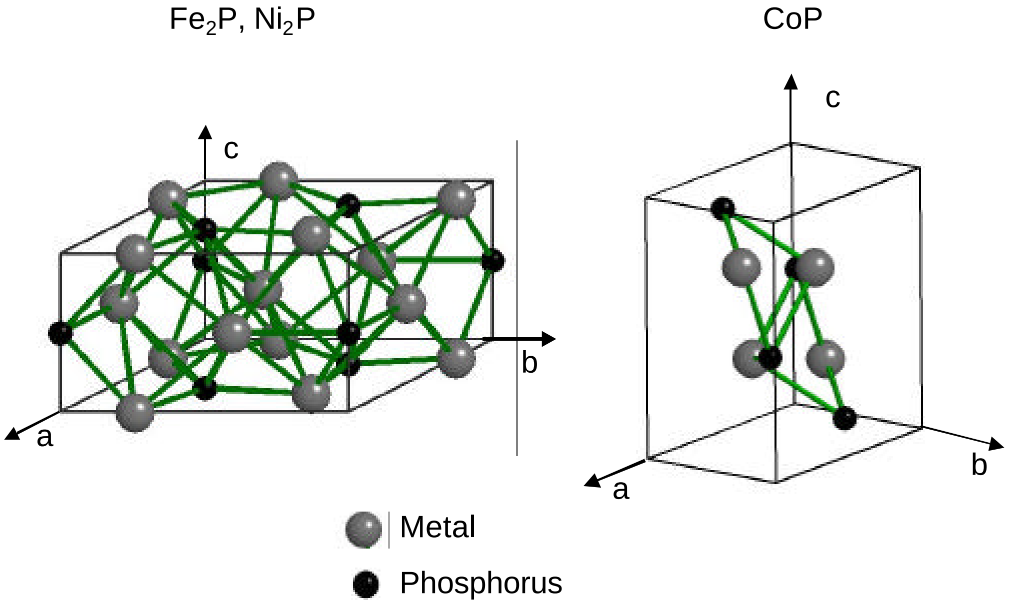

Figure 2.1. Crystal structures of Fe_2P, CoP and Ni_2P

The investigation of the phosphide materials in this study was begun by a study of the synthesis of bulk materials of various metal-to-phosphorus ratios (M/P) by the temperature-programmed method. This was carried out to prepare suitable references for the supported materials, and to evaluate the conditions of preparation needed when a support was employed.

The synthesis of the bulk phosphides involved two stages, preparation of phosphate precursors and reduction of the precursors in a temperature programmed manner. The results will be discussed first for iron. The precursors prepared in the first stage had different Fe/P ratios, set at the time of preparation by adjusting the mol ratio of the constituents. The precursors were formed by the thermal decomposition of mixtures of the metal nitrate and ammonium phosphate in air. Because the nitrate and ammonium ions are unstable at high temperature, it was expected that the mixture would decompose to a metal phosphate or metal oxide-phosphate. At high metal ratios some metal oxide was also likely. X-ray diffraction patterns of the precursors showed that they were amorphous.

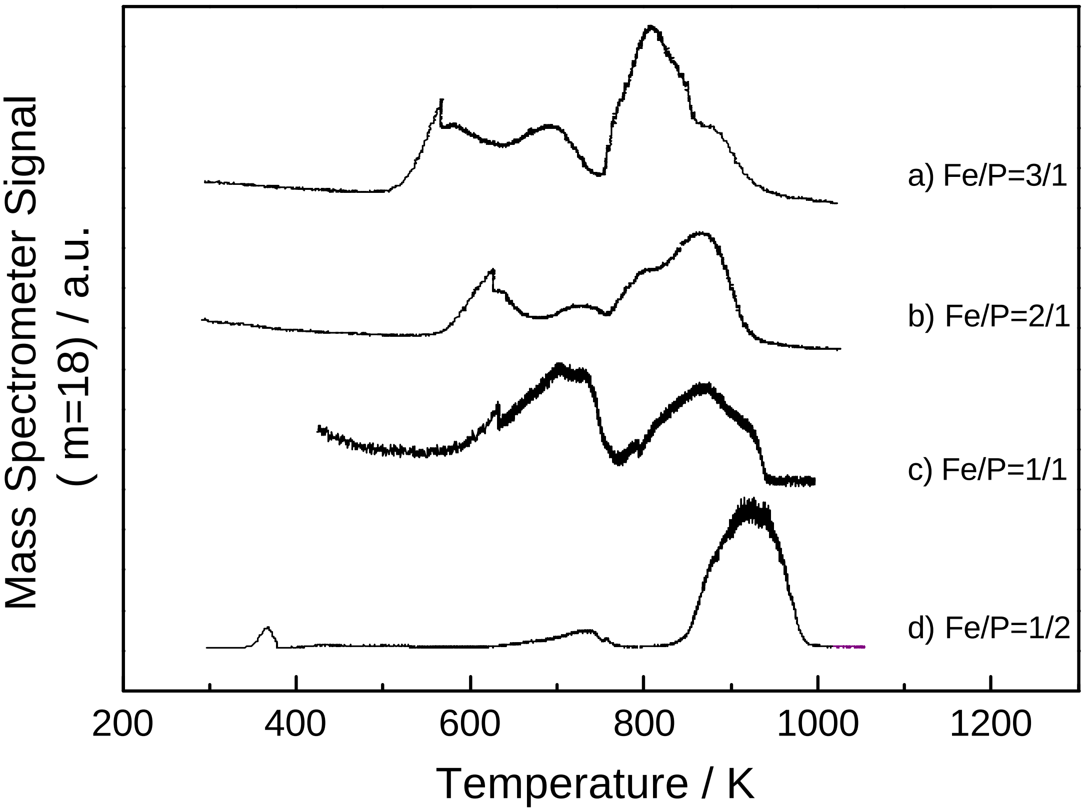

Figure 2.2. Temperature-programmed reduction of bulk iron phosphates at β= 1 K/min (0.01667 K s^{-1}) (Fe to P ratios used in the preparation are indicated)

Temperature programmed reduction (TPR) of the precursors was carried out in the second stage (Fig. 2.2). Only the results for mass 18 (H_2O) are shown, as the other monitored masses were featureless or provided little additional information. The TPR traces show two systematic trends for the samples with different Fe/P ratios. First, for higher Fe contents (Fig. 2.2a-c), the TPR traces show more peaks and a more complicated overall reduction pattern. Second, for higher Fe contents, all the reduction peaks including the initial and final features are shifted to lower temperatures. These trends are reasonable.

For higher Fe contents, the precursor is probably a mixture of iron oxide, iron phosphate and possibly other components, and their separate reduction results in different peaks. Also for these higher Fe contents, the proportion of iron oxide should increase, and since this oxide is easily reducible, its TPR peaks appear at lower temperatures. In fact, it is likely that some metallic Fe is formed and that it assists in the reduction of the other components. For low Fe contents (Fig. 2.2 d), there is no iron oxide and reaction occurs at the intrinsic reduction temperature of the main phosphate phase (~ 920 K). Because this temperature is high, even if a mixture of components other than phosphates existed, individual reduction steps cannot be resolved and the whole process appears to occur in one stage.

Analysis of the products of TPR was carried out by XRD (Fig. 2.3). The diffraction patterns all show a high background because of fluorescence by the iron. However, the presence of distinct iron phosphides can be seen easily. For the samples with Fe/P ratios of 3/1 and 2/1, the XRD results show the expected phases of Fe_3P (Fig. 2.2a) and Fe_2P (Fig. 2.3b). Comparison is made with standards from the powder diffraction file (PDF) (37) as indicated in the figure. For the sample with Fe: P ratio of 1/1, the obtained phase was still Fe_2P (Fig. 2.3c), and there was a deficiency in phosphorus. Similarly, for the sample with an Fe/P ratio of 1/2, the observed phase was FeP. Thus, although the preparations were carried out with stoichiometric quantities of metal and phosphorus, the final products tended to be metal-rich.

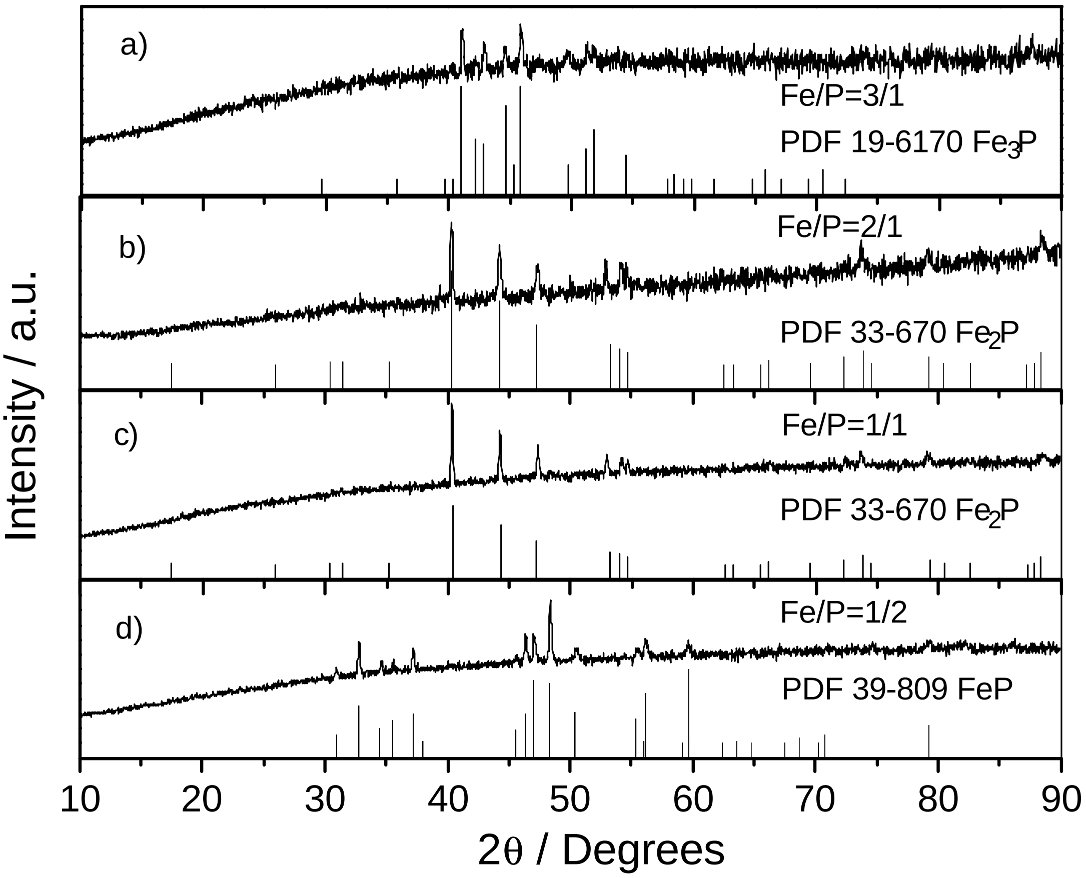

Figure 2.3. X-ray diffraction patterns of iron phosphides (PDF file references are also included)

There are probably several processes which contributed to the loss of phosphorus in these samples. Some of the loss may have occurred during the TPR process as traces of PH_3 were detected in the mass spectrometer signal and some volatile products were observed to condense at the exit of the reactor. Some of the loss probably also occurred in the calcination step at 773 K to form the phosphate precursor. A small amount of a white solid was found to have sublimed onto the lid of the ceramic calcination vessel. This was likely to be P_2O_5 with a melting point of 563 K, and sublimation temperature of 787 K. The loss of P was observed in all samples with high P levels. There is also a possibility that some extra phosphorus in amorphous form remained mixed in the samples, and that the observed phases were simply the stable ones under the preparation conditions.

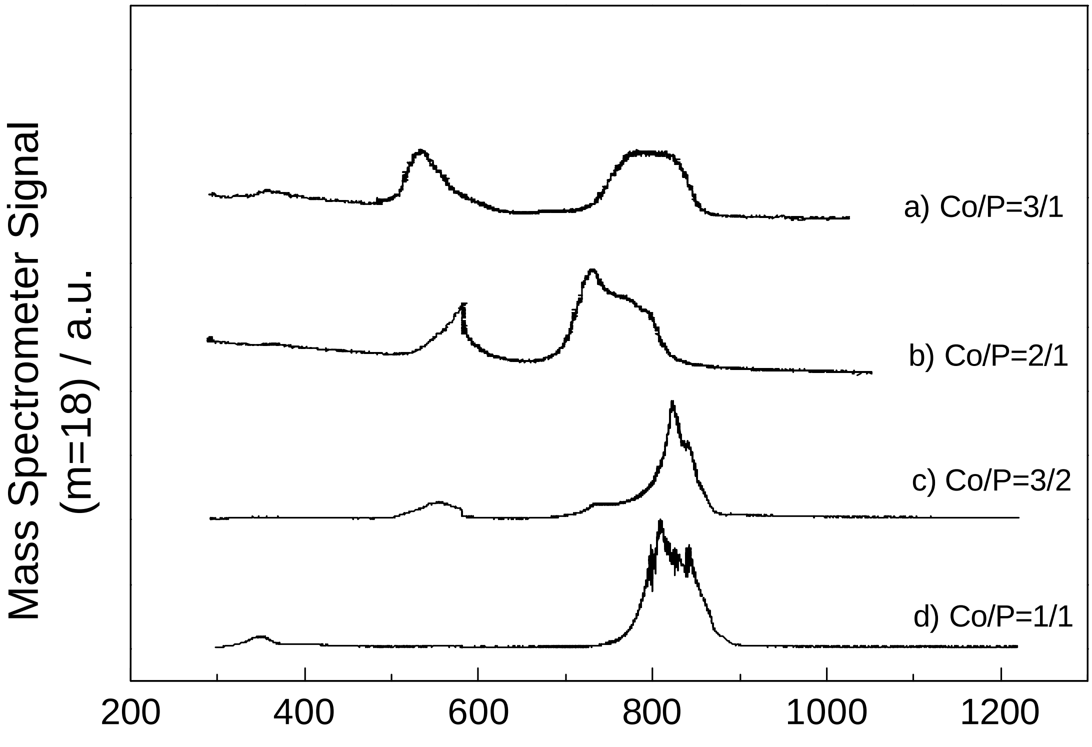

Figure 2.4. Temperature-programmed reduction of bulk cobalt phosphates at β= 1 K/min ($0.01667\ K\ s^{-1}$) (Co to P ratios used in the preparation are indicated)

The trends in the TPR results for the cobalt samples (Fig. 2.4) are similar to those of the iron samples. The reaction traces consist of two main features, a low temperature peak and a more complicated high temperature signal. (The sample with Co/P = 1/1 has a small feature at ~350 K, probably due to dehydration.) The low temperature peak appears between 500-600 K and is more intense for higher Co contents (Fig 2.4a-c). It also shifts to lower temperature with increasing Co content. This behavior is consistent with the reduction of a cobalt oxide species. The higher temperature signal appears between 700-900 K and probably corresponds to the reduction of cobalt phosphate, which is expected to be more difficult to reduce. It is the main feature for the Co/P = 1/1 sample (Fig. 2.4d). The XRD patterns of the reduced cobalt samples (Fig. 2.5) show that Co_2P was obtained from the samples with Co/P ratios of 3/1, 2/1, 3/2 (Fig. 2.5a-c), and CoP was obtained as expected from the sample with a Co/P ratio of 1/1 (Fig. 2.5d). It appears that Co_2P is a particularly stable phase at these conditions.

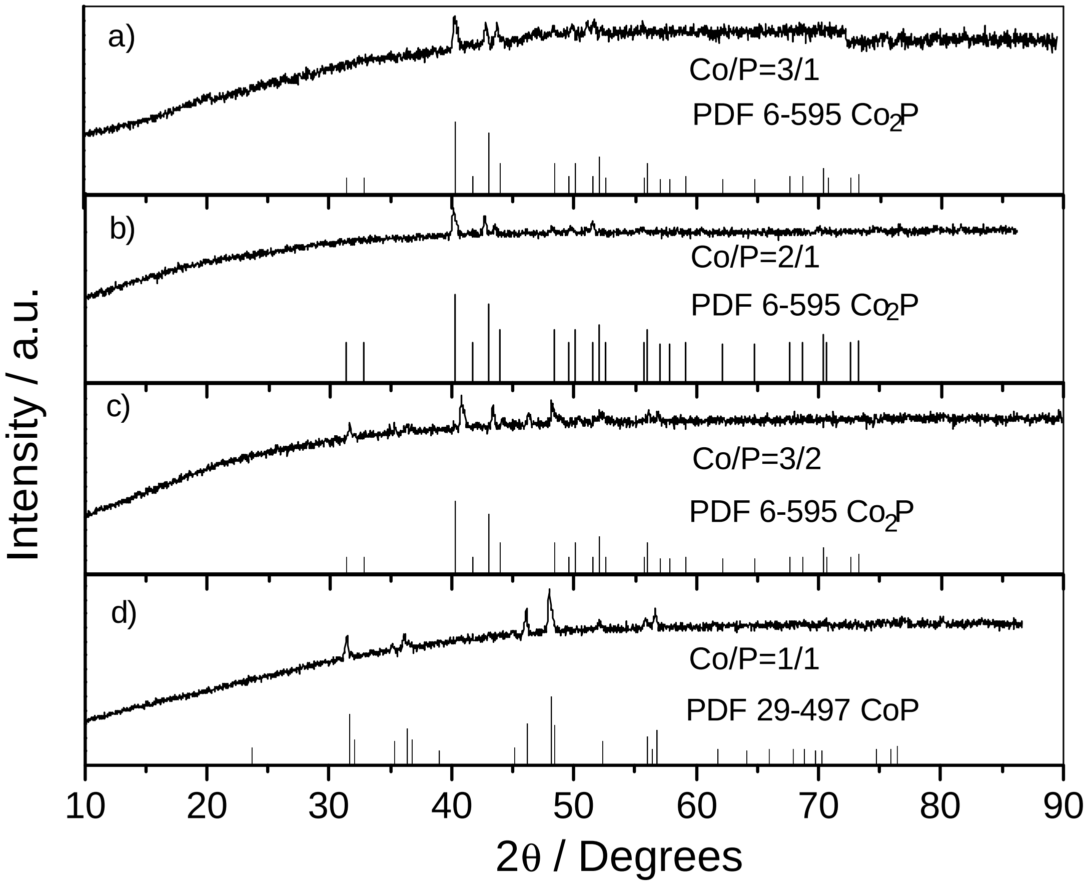

Figure 2.5. X-ray diffraction patterns of reduced cobalt phosphates (PDF file references are also included)

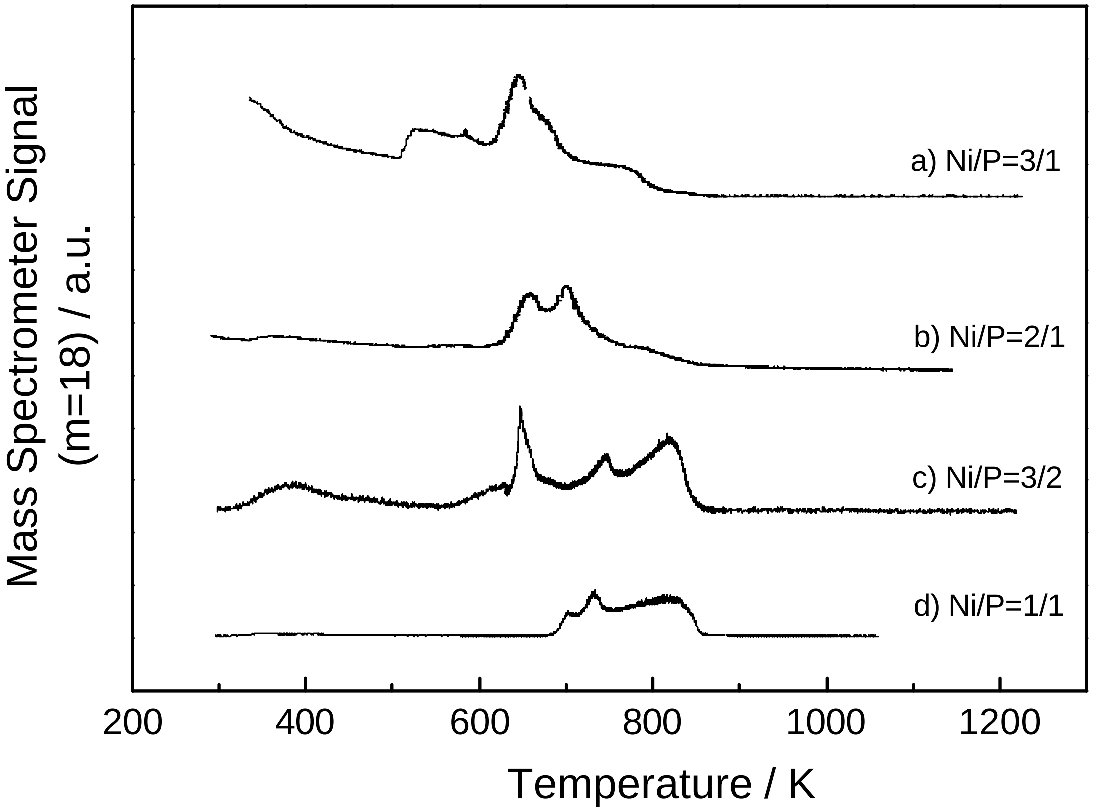

Figure 2.6. Temperature-programmed reduction of bulk nickel phosphates at β= 1 K/min (0.01667 K s^{-1}) (Ni to P ratios used in the preparation are indicated)

The same trends in the TPR traces were also observed with the nickel samples (Fig. 2.6). The reduction features were a composite of different peaks, occurring in a low temperature range at 500 – 700 K, and at a high temperature range of 700 – 850 K. These various features are attributed again to the reduction of different compounds, likely nickel oxides and nickel oxide phosphate at the low temperatures and nickel phosphate at the high temperatures. As expected, Ni_3P was observed in the sample with a Ni/P ratio of 3/1 (Fig. 2.7a). But for the Ni/P ratios of 2/1, 3/2, and 1/1 (Fig. 2.7b-d), the phase obtained was Ni_2P. Probably, this is the stable phase at the conditions of the preparation, since not all the phosphorus in the precursor phosphate mixtures is likely to have sublimed. Different from the other samples, the TPR trace of the sample with the Ni/P ratio of 1/1 did show some P and PH_3 during the reduction process. This accounts for the loss of P in this sample.

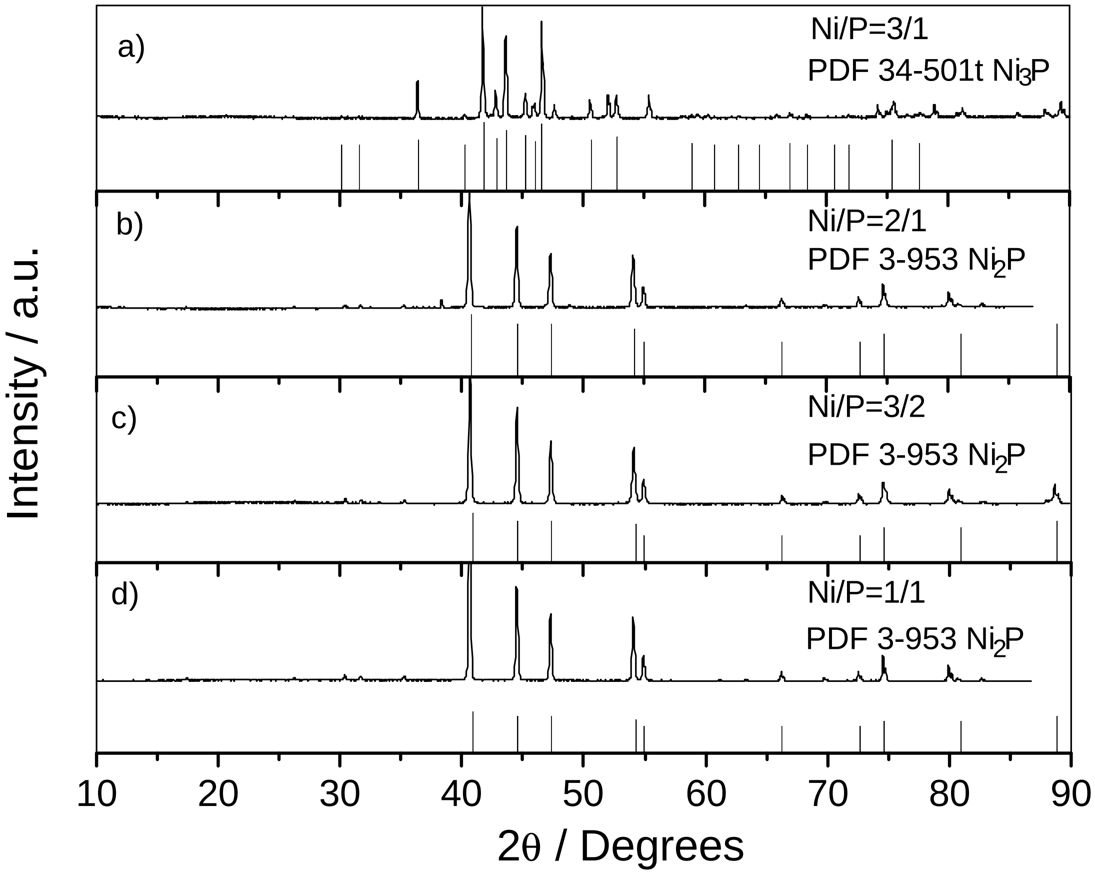

Figure 2.7. X-ray diffraction patterns of reduced nickel phosphates (PDF file references are also included)

To summarize these TPR and XRD results, the reduction of phosphate precursors occurs readily in the Fe, Co, and Ni systems, with maximum temperatures of about 900 K. A number of bulk phosphide compounds can be produced depending on the stoichiometric proportions of M/P used, but the Fe_2P, CoP and Ni_2P products are the preferred phases under the experimental conditions used in this study.

2.3.2 Properties and preparation of supported phosphides

In order to study the catalytic properties of the Fe, Co and Ni samples high surface area materials were desired, and therefore, the phosphides were prepared in supported form using silica as the carrier. The preparation involved the same steps used in the synthesis of the bulk compounds. First, phosphates were prepared on the support and then were reduced by TPR. The final temperatures for preparing hydrotreating catalysts were determined by noting the point where the intensity of the water signal returned to baseline in preliminary TPR test measurements on small samples. The final temperature for supported iron, cobalt, nickel samples were 1000 K, 900 K, and 850 K, respectively (Fig. 2.8). Silica was selected as the carrier because in dehydrated form has few acid and base sites and is likely to offer minimal support interaction to affect the properties of the phosphides. Thus, the intrinsic activity of the phosphides could be determined.

Comparison of the TPR results obtained for the bulk samples and the corresponding supported samples (Fig. 2.8) provides strong evidence that the transformation of the phosphates to phosphides proceeded in the same manner for both bulk and supported samples. Aside from a slightly more pronounced low-temperature dehydration feature for the supported samples, the TPR traces for the samples of iron and cobalt were very similar to those of the unsupported forms. The reduction trace of the supported nickel sample was somewhat simpler than that of the bulk sample, but occurred at essentially the same temperature range.

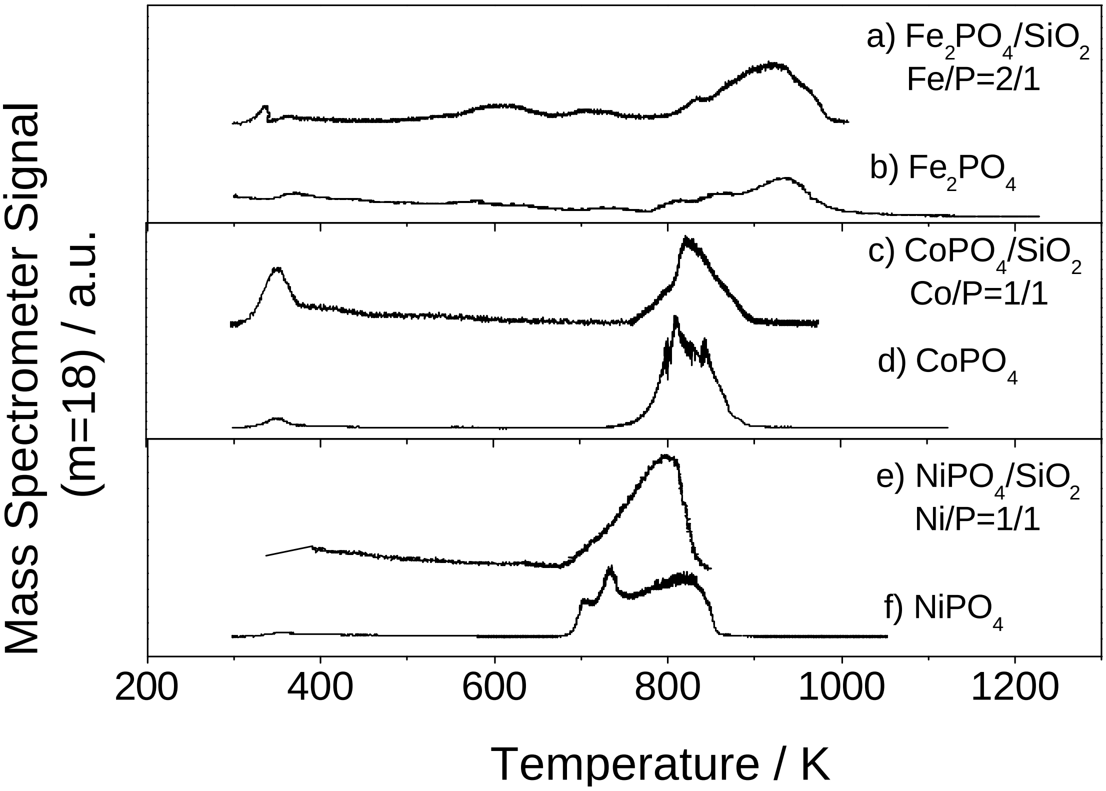

Figure 2.8. TPR comparison of supported and unsupported catalysts at β= 1 K/min (0.01667 K s^{-1}).

The characterization results for the bulk and supported samples are reported in Table 2.3. The specific surface areas (S_g) of the bulk materials were low, approximately 3 m^2g^{-1}, while those of the supported materials were close to that of the support (90 m^2g^{-1}).

The experimental CO uptakes of the samples are reported in the third column of Table 2.3. They were low for the bulk materials but increased for the supported samples.

Table 2.3. Characterization results of samples

Samples	BET Surface area S_g / m^2g^{-1}	CO uptake $\mu mol\ g^{-1}$	D_p nm	D_c nm	Metal site concentration $\mu mol\ g^{-1}$
Fe_2P	2.7	3	330	38	45
Fresh Fe_2P/Silica	97	16		23	90
Spent Fe_2P/Silica	83	0		23	90
CoP	3.1	3	310	40	51
Fresh CoP/Silica	87	16		21	72
Spent CoP/Silica	90	4		21	72
Ni_2P	3.3	4	260	36	55
Fresh Ni_2P/Silica	98	15		20	67
Spent Ni_2P/Silica	100	13		20	67

The particle diameter of the bulk materials was calculated by the equation $D_P = 6/\rho S_g$ using their surface area and the bulk density (Table 2.2). The particle sizes for the bulk Fe_2P, CoP, and Ni_2P samples were similar, about 260-330 nm (Table 2.3). The crystallite sizes (D_c) were obtained from the Scherrer equation presented in the experimental section. The crystallite sizes for the bulk phosphides were again similar, about 36-40 nm. For all the bulk samples, $D_p > D_c$, and this could be due to strain and disorder in the crystallites or crystallite agglomeration. The latter is probably the larger contributor as no support was used to stabilize the samples.

The last column in Table 2.3 reports the theoretical metal site concentration assuming that the samples were composed of uniform spherical particles. It was calculated from the equation

$$\text{Metal site concentration} = S_g \cdot \bar{n} \cdot f$$

where S_g is specific surface area, $\bar{n}$ is the surface metal atom density, and f is the fractional weight loading (e.g., g Fe_2P/g catalyst) of the sample (Table 2.2.1). For the bulk samples the actual S_g was employed, while for the supported samples it was calculated from the crystallite size using the equation $S_g = 6/\rho D_c$. The last factor, f, accounts for the loading of the active phase on the supported samples.

In all cases the experimental CO uptake was considerably smaller (average 6.6 % for the bulk samples, average 20.5 % for the fresh supported samples) than the theoretically expected metal site concentration (Table 2.3) for a clean surface. This indicates that possibly the surface is blocked by some species that prevents adsorption such as phosphorus or unreduced oxygen. In the case of transition metal carbides it is found that oxygen uptakes are considerably higher than CO uptakes (38,39), and this suggests that oxygen should be tried as a chemisorption probe.

The effect of the heating rate on the peak temperature (T_p) associated with the reduction of supported catalysts (Fig. 2.2.9) was briefly examined in this work. The peak positions for water formation shifted about 40-60 K to higher temperature as the heating rate (β) was increased from 0.0167 (1 K min^{-1}) to 0.0833 K s^{-1} (5 K min^{-1}). According to temperature-programmed reaction theory (40), the peak temperature (T_p), is related to the heating rate (β) and the apparent activation energy (E_a) (Table 2.4) by the Redhead equation ($2 \ln T_p - \ln \beta = E_a/RT_p + \text{Constant}$) (40). The activation energies found for Fe_2P/silica, CoP/silica and Ni_2P/silica were 200 kJ mol^{-1}, 220 kJ mol^{-1} and 150 kJ mol^{-1}, respectively. The results here are comparable with the activation energy of oxygen diffusion in the corresponding metal oxides, FeO, CoO and NiO, which are 126, 144 and 166 kJ mol^{-1}, respectively, with preexponential factors of 1.4×10^{-2}, 2.15×10^{-3} and 2×10^{-4} $cm^2\ s^{-1}$ (41). The correspondence is reasonable as many solid state transformations are governed by diffusion processes (42).

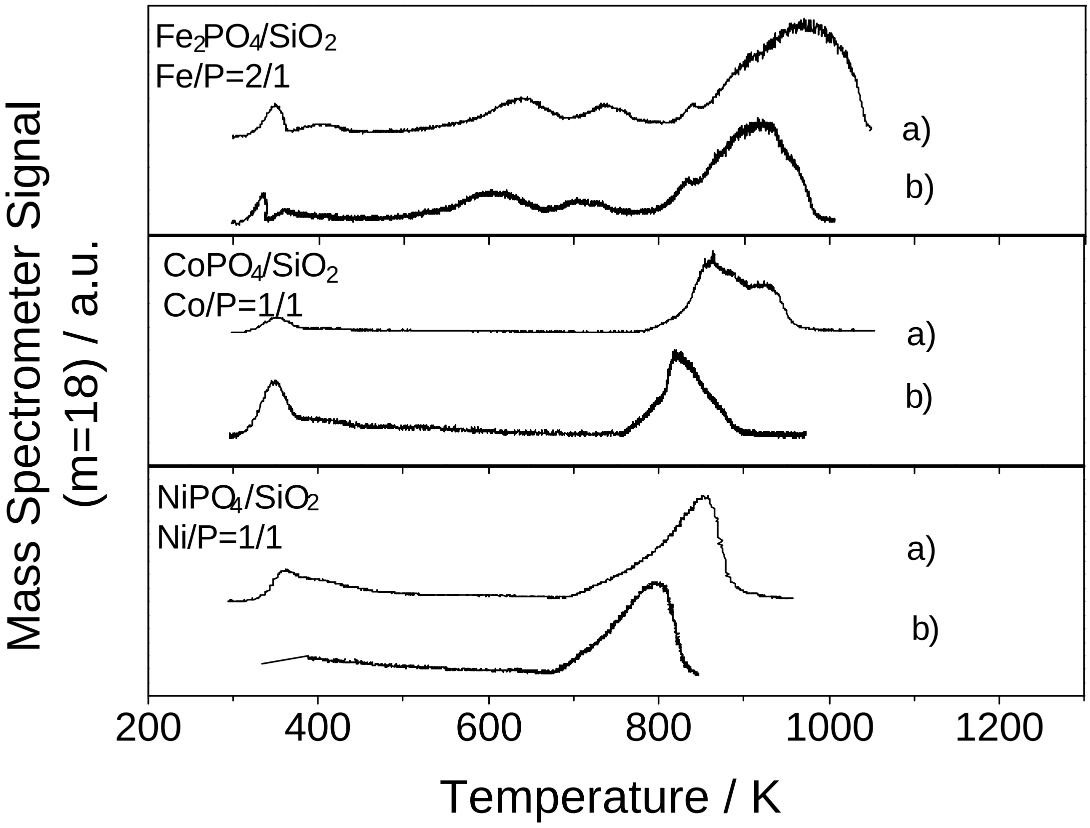

Figure 2.9. TPR profiles of supported catalysts at different heating rate (β)

a) β= 5 K/min (0.08333 K s^{-1}); b) β= 1 K/min (0.01667 K s^{-1})

Table 2.4. Apparent activation energy (E_a) of synthesis of the supported catalysts

Samples	E_a / kJ mol^{-1}
Fresh 14 wt. % Fe_2P/Silica	200
Fresh 9.4 wt. % CoP/Silica	220
Fresh 9.4 wt. % Ni_2P/Silica	150

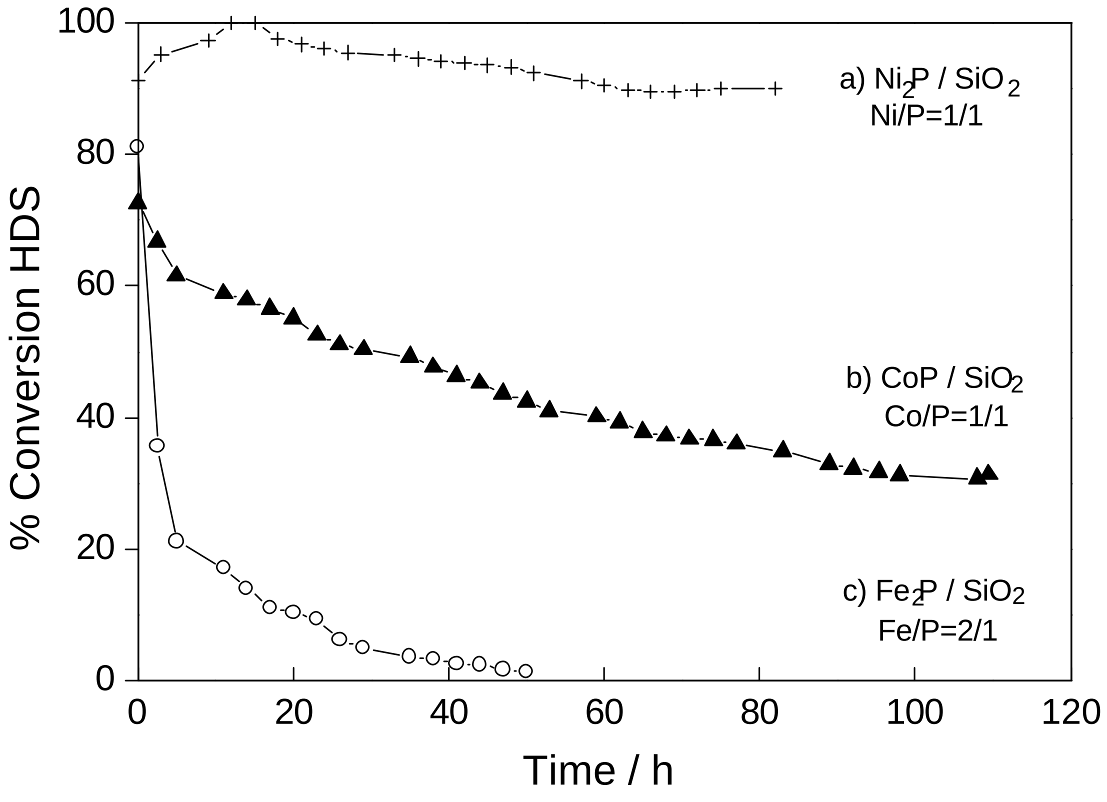

Figure 2.10. Hydrodesulfurization performance of supported catalysts. (Basis: 35 μmol of chemisorption sites)

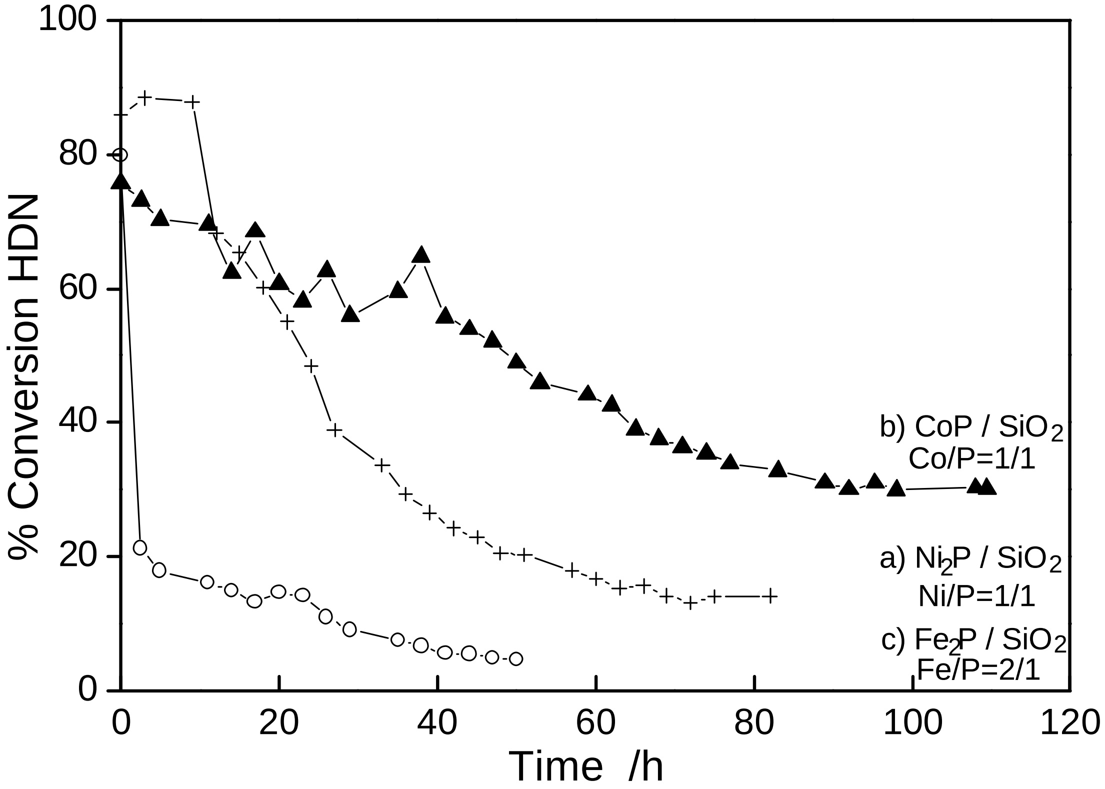

Figure 2.11. Hydrodenitrogenation performance of supported catalysts. (Basis: 35 μmol of chemisorption sites)

2.3.3 Catalytic activity in hydroprocessing

Figure 2.10 and Figure 2.11 present the HDS and HDN activities for the reactions of dibenzothiophene and quinoline, respectively. All three samples have high initial activities for HDS and HDN. However, except for the nickel sample in HDS, all catalysts undergo deactivation. The Fe_2P/SiO_2 lost all HDS and HDN activity by 60 h, while the CoP/SiO_2 appeared to reach a baseline of about 32 % HDS and 31 % HDN at around 100 h. Only the Ni_2P/SiO_2 had good, stable activity in HDS. The HDS sequence for the three samples was Ni_2P/SiO_2> CoP/ SiO_2> Fe_2P/ SiO_2, while the HDN sequence was: CoP/ SiO_2 > Ni_2P/ SiO_2 > Fe_2P/ SiO_2. Compared with a commercial Ni-Mo-S/ γ-Al_2O_3 catalyst at the same conditions (20), Ni_2P/SiO_2 had a higher HDS activity with 90 % versus 76 % conversion, but a lower HDN activity with 14 % versus 38 % conversion. The measurements were made on the basis of equal chemisorption sites loaded in the reactor (35 μmol for the phosphides, 33 μmol for the sulfide). For the phosphides CO at room temperature was used for the chemisorption and for the sulfide O_2 at dry ice/acetone temperature. It may be that the CO chemisorption underestimates sites on the phosphide, so the conversions should be taken just as an approximation of intrinsic activity.

Table 2.5. Product distribution in hydroprocessing*

Reactants	Conversion / %			Selectivity / %		
	Type	Ni_2P/SiO_2	CoP/SiO_2	Product	Ni_2P/SiO_2	CoP/SiO_2
Dibenzo thiophene	HDS	90	32	biphenyl	100	100
Quinoline	HDN	14	31	propylcyclo hexane	4	16
				propylbenzene	9	9
	HYD	44	49	5,6,7,8-tetrahydro quinoline	33	30
				orthopropyl aniline	31	23
				1,2,3,4-tetrahydro quinoline	24	22
Benzofuran	HDO	35	11	ethylbenzene	100	100
Tetralin	deHYD	31	6.5	naphthalene	98.2	91.5
	HYD	0.6	0.6	trans-decalin	0.6	3.6
				cis-decalin	1.2	4.9

*Catalyst loaded was equivalent to 35 μmol of CO uptake sites.

A listing of conversions and selectivities for all the reactions is provided in Table 2.5. For dibenzothiophene the only product observed was biphenyl. However, for quinoline a number of species were obtained, and these were categorized as HDN products and hydrogenation (HYD) products. For benzofuran, again only one product was obtained, ethylbenzene. The amount of benzofuran used was small (500 ppm) and the reaction is facile so is unlikely to interfere with the HDS and HDN reactions, as known from other studies with carbides, nitrides, and sulfides (43,44). In the case of tetralin, at the reaction conditions the major species obtained was the dehydrogenation product naphthalene, although small amounts of cis- and trans-decalin were also observed.

Table 2.6. Rates of HDS and HDN of the supported catalysts

Sample	Turnover rate[1] / 10^{-3} s^{-1}		Areal rate[2] / 10^{15} molec m^{-2} s^{-1}		Specific rate[3] / 10^{8} mol $g^{-1}s^{-1}$		Volumetric rate[4]/ 10^{9} mol cm^{-3} s^{-1}	
	HDS	HDN	HDS	HDN	HDS	HDN	HDS	HDN
Fe_2P/SiO_2(Fe/P=2/1)	0	0	0	0	0	0	0	0
CoP/SiO_2(Co/P=1/1)	0.81	1.2	1.4	2.1	1.3	1.9	4.8	7.0
Ni_2P/SiO_2(Ni/P=1/1)	1.5	0.60	3.4	1.4	2.2	0.9	8.1	0.33

[1] Calculated from r_t = QX/S, where Q is the molar rate of reactant, X is the conversion, and S is the mol of sites loaded. The basis used was 70 μmol. Conversions were adjusted using the first-order formula $X_2 = 1-(1-X_1)^{S_2/S_1}$, where S_2/S_1 = 70 μmol/35 μmol = 2, and gave higher X than reported in Table 2.5 (CoP: HDS 54%, HDN 52%, Ni_2P: HDS 99%, HDN 26%).

[2] Calculated from $r_A = QXN_A/WS_gf$, where N_A is Avogadro's number, W is the weight of catalyst, S_g is the metal phosphide surface area, and f is the fractional loading of phosphide.

[3] Calculated from $r_S = r_t$(CO uptake).

[4] Calculated from $r_V = r_S\rho$, where ρ is the apparent density of the catalysts ~0.37 g cm^{-3}.

Turnover rates and areal rates measured at the baseline levels are listed in Table 2.6. The basis of comparison is now 70 μmol of sites, to make the numbers directly comparable to others presented in this thesis and published elsewhere (45). The procedure for conversion assumes a first-order reaction and is given in the footnotes of the table. The turnover rates are based on the experimentally determined CO uptakes on the fresh catalysts, while the areal rates are based on the calculated surface area of the phosphide crystallites using $S_g = 6/\rho D_c$ and the weight loading factor f. The Fe_2P catalyst deactivated completely and its rate is reported as zero. The CoP/SiO_2 had areal rates of 1.4×10^{15} molec $m^{-2}s^{-1}$ in HDS and 2.1×10^{15} molec $m^{-2}s^{-1}$ in HDN, while the Ni_2P/SiO_2 had rates of 3.4×10^{15} molec $m^{-2}s^{-1}$ in HDS and 1.4×10^{15} molec $m^{-2}s^{-1}$ in HDN. In a recent study of the HDN on unsupported samples Stinner, et al. report areal rates of 4.8×10^{16} molec $m^{-2}s^{-1}$ on Co_2P and 5.8×10^{16} molec $m^{-2}s^{-1}$ on Ni_2P (22). The higher HDN rates on those samples can be attributed to several factors. First, Stinner, et al. studied only HDN and employed a more reactive substrate (o-propylaniline rather than quinoline), which probably led to higher rates. They also carried out their tests without using sulfur compounds in the feed. Sulfur compounds can lead to competitive adsorption and lower rates. Finally, Stinner, et al. used low surface area (1-3 m^2g^{-1}) unsupported materials in a low-conversion regime, which would tend to result in higher rates. Nevertheless, despite the differences in experimental conditions the rates are of a similar order of magnitude.

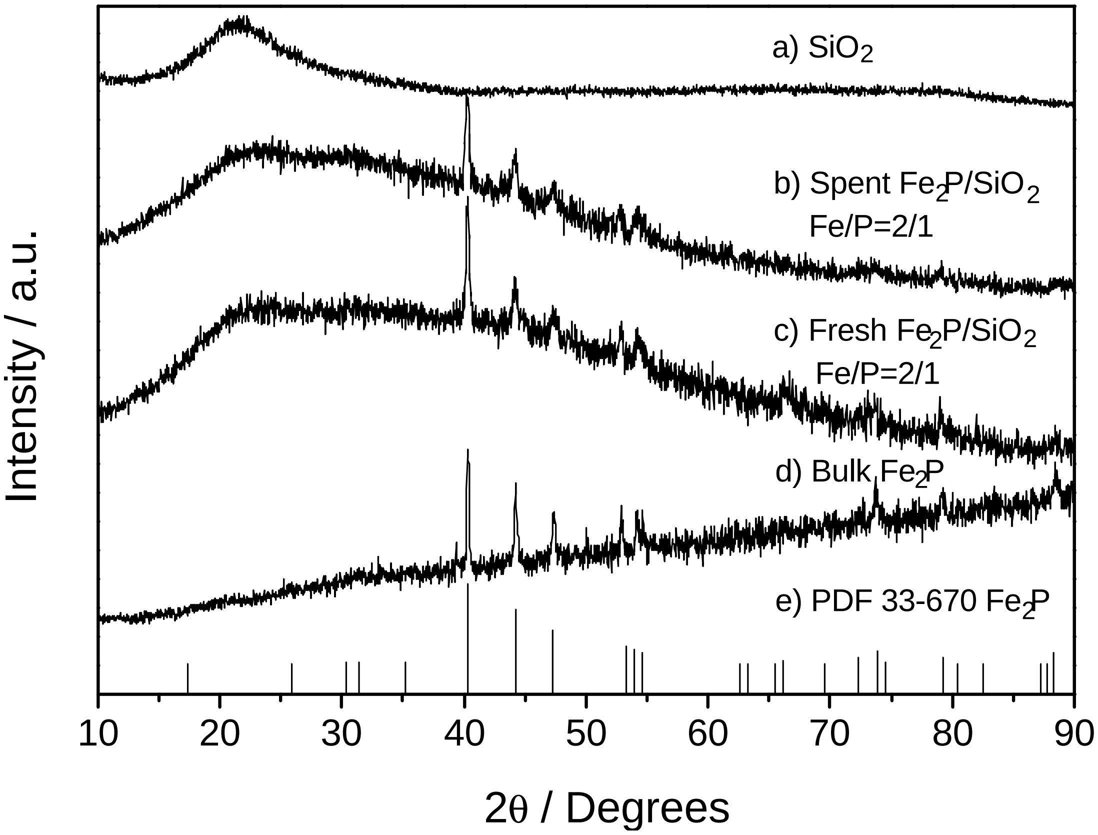

Figure 2.12. X-ray diffraction patterns of iron phosphides and references

a) Blank sample-SiO_2; b) Spent sample Fe_2P/SiO_2; c) Fresh sample Fe_2P/SiO_2; d) Bulk sample Fe_2P; e) PDF 33-670 Fe_2P (Ref. 41)

The XRD patterns of the silica support, fresh phosphide samples, spent samples, and PDF references are compared in Figures 2.12-2.14. These results show that silica did not influence the phases of the phosphides formed, which were the same as those obtained in the bulk materials, Fe_2P, CoP, and Ni_2P. The XRD patterns for the spent iron and cobalt samples were unchanged from the corresponding fresh samples, which shows that the Fe_2P phase (Fig. 2.12) and CoP phase (Fig. 2.13) are stable during the hydrotreating reaction.

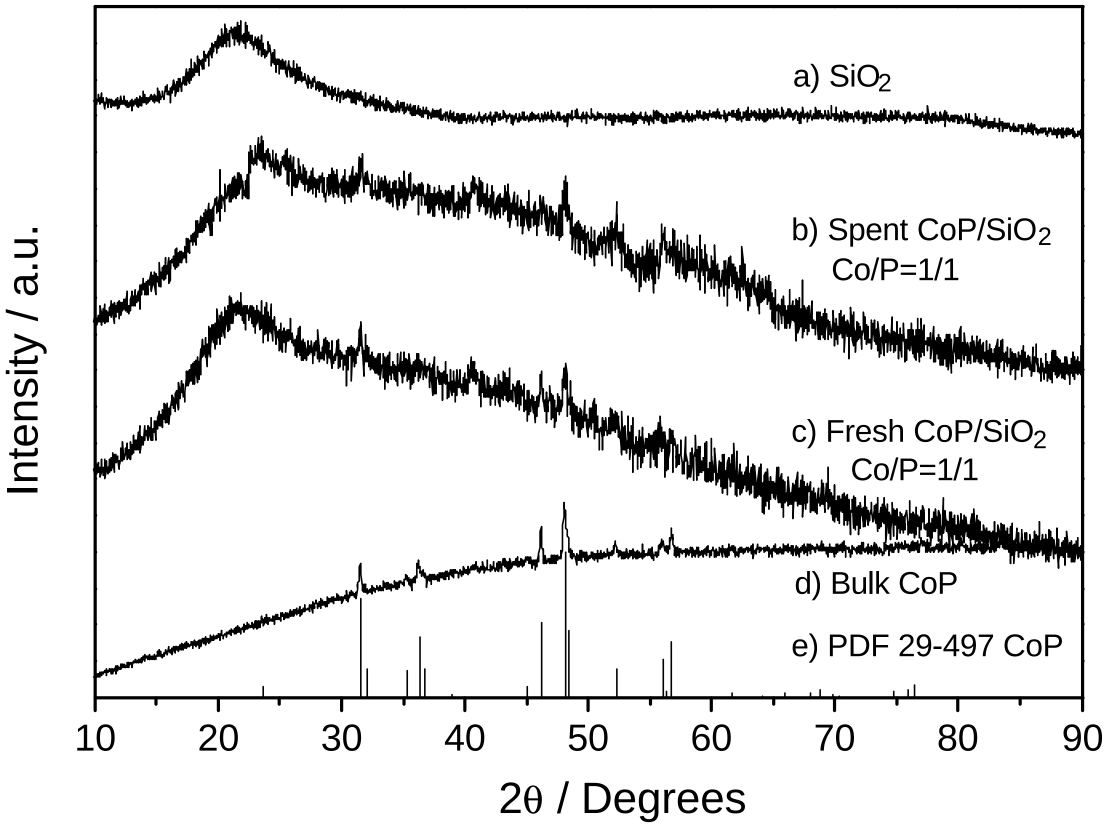

Figure 2.13. X-ray diffraction patterns of cobalt phosphides and references

a) Blank sample-SiO_2; b) Spent sample CoP/SiO_2; c) Fresh sample CoP/SiO_2; d) Bulk sample CoP; e) PDF 29-497 CoP (Ref. 41)

For the spent nickel sample, one more peak was observed (Fig. 2.14). Comparing this pattern with those of other nickel phosphide compounds, it was found that the peak (*) matched one due to $Ni_{12}P_5$. This indicated that possibly a part of the Ni_2P phase transformed to a $Ni_{12}P_5$ like phase during hydrotreating. XPS measurement for this sample (Table 2.7) showed a P/Ni ratio close to 1 for the fresh sample, which decreased to 0.77 for the spent catalyst. This decrease may be related to the drop in HDN activity for this sample. The XPS analysis surprisingly also indicated a lack of S or N on the spent sample.

The measurements were repeated on samples treated in He (just to remove volatile compounds), but the results were the same. This is likely due to lack of sensitivity by XPS at the levels expected for surface sulfur species in these supported samples. Already the signals for Ni and P were very low.

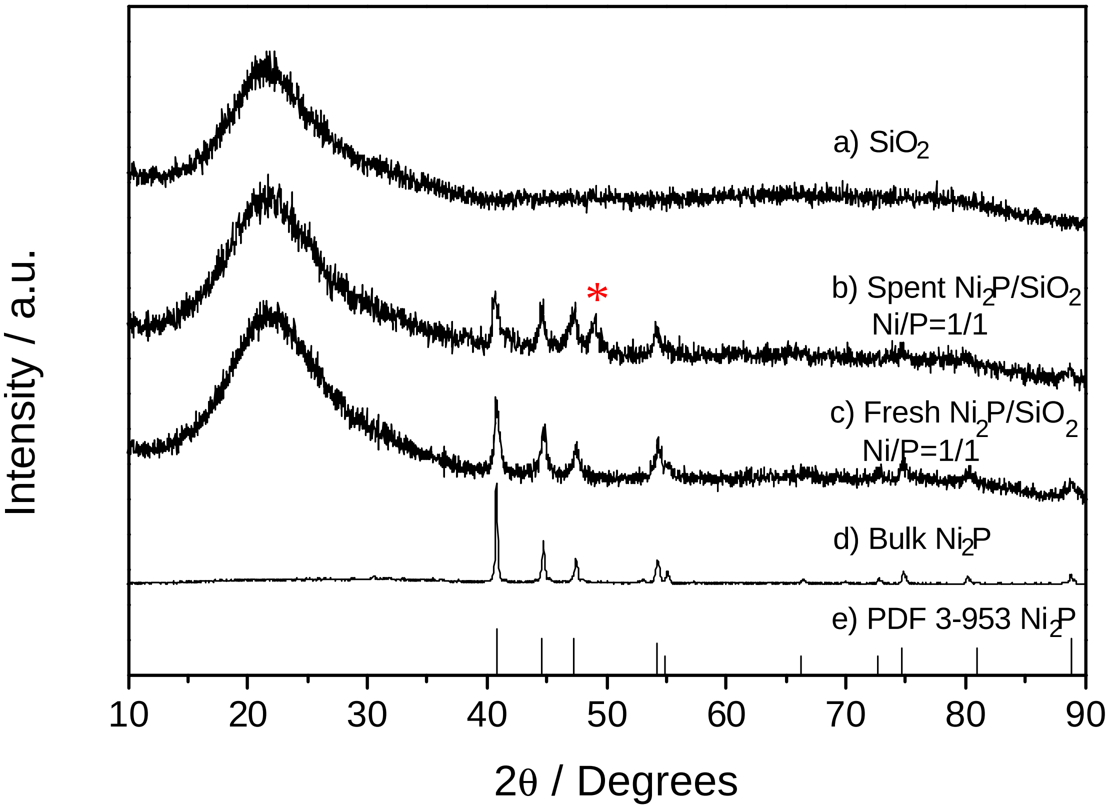

Figure 2.14. X-ray diffraction patterns of nickel phosphides and references

a) Blank sample-SiO_2; b) Spent sample Ni_2P/SiO_2; c) Fresh sample Ni_2P/SiO_2; d) Bulk sample Ni_2P; e) PDF 3-953 Ni_2P (Ref. 41)

Table 2.7. XPS results for supported nickel samples

Fresh 9.4 wt. % $\mathrm{Ni_2P}$/silica	Element	C*1s*	O*1s*	N*1s*	S*2p*	P*2p*	Ni*2p*	Si*2p*
	Concentration (%)	16.73	55.42	0	0	0.80	0.83	26.22
Spent 9.4 wt. % $\mathrm{Ni_2P}$/silica	Element	C*1s*	O*1s*	N*1s*	S*2p*	P*2p*	Ni*2p*	Si*2p*
	Concentration (%)	19.24	53.16	0	0	0.36	0.47	26.77

The results of post hydrotreating characterization are also presented in Table 2.3. For the iron sample, the CO uptake decreased to zero after the hydrotreating. The loss of the CO uptake is likely associated with the dramatic deactivation of the iron sample (Fig. 2.10c, 11c). As to the spent cobalt sample, the CO uptake also decreased substantially, but not to zero as in the case of the iron sample. This was in line with the less complete deactivation of the catalyst. In the case of nickel, again a decrease in CO uptake was observed, but the decrease was much smaller than those of the iron and cobalt samples. Overall, the trend appears to indicate that the decrease in catalytic performance is related to the loss of active sites.

The reduction in the number of active sites is apparently caused by sulfidation of the catalysts. This was investigated by extended x-ray absorption spectroscopy (EXAFS) of the fresh and spent samples (45) and the results will be presented in subsequent chapter. The results indicate that the catalysts are phase-pure and sulfidation is restricted to the surface of the phosphide crystallites, as x-ray diffraction analysis shows that the phosphide phase is retained. The surface sulfidation process appears to be more pronounced in iron and cobalt phosphide which show considerable deactivation in HDS and HDN. The nickel phosphide appears to be more tolerant to sulfur, and thus retains high HDS activity. This is entirely reproducible. It's HDN activity is lowered, probably because the latter reaction is structure-sensitive (45), and the site requirements for nitrogen removal are disrupted.

2.4 Conclusions

Pure Fe_2P, CoP, and Ni_2P, phases were successfully synthesized by means of temperature-programmed reduction of the corresponding phosphates. The silica-supported forms of these samples were also successfully prepared, with retention of the active phase and increased CO uptake and BET surface area. It was found that Fe_2P/SiO_2 had good initial activity for HDS of dibenzothiophene and HDN of quinoline, but that this activity fell to zero in about 60 h. The CoP/SiO_2 catalyst also deactivated, but appeared to reach a stable baseline of 32 % HDS and 31 % HDN conversion. Only the Ni_2P/SiO_2 had a stable and high conversion in HDS of 90 %, although its HDN was low at 14 %. The deactivation in all cases was associated with a decrease in the number of surface metal sites as titrated by the chemisorption of CO. For the most promising catalyst Ni_2P/SiO_2, HDS was higher than that of a commercial catalyst Ni-Mo-S/γ-Al_2O_3, based on equal sites loaded in the reactor as measured by CO uptake for the phosphide and low-temperature O_2 chemisorption for the sulfide. The development and improvement of this group of phosphides in the hydroprocessing field is a promising area of research.

References

---

1. Aronsson, B., Lundström, T., Rundqvist, S., "Borides, Silicides and Phosphides", Wiley, New York, 1965.

---

2. Boudart, M., Cusumano, J. A., Levy, R. B., “New catalytic materials for the liquefaction of Coal, Research project 415, final report”, p. 184, Catalytica Associates, Inc., 5 Palo Alto Square, Palo Alto, California, 1975.
3. Damyanova, S., Spojakina, A., Vit, Z., *Collect. Czech. Chem. Commun*., **57**, 1033 (1992).
4. Ozkan, U. S., Zhang, L. P., Ni, S. Y., Moctezuma, E., *J. Catal*., **148**, 181 (1994).
5. Gulková, D., Zdražil, M., *Collect.Czech. Chem. Commun*., **64**, 735 (1999).
6. Poulet, O., Hubaut, R., Kasztelan, S., Grimblot, J., *Bull. Soc. Chim. Belg. European Section*, **100 (**11-12), 857(1991).
7. Fitz, C. W., Jr., Rase, H. F., *Ind. Eng. Chem. Prod. Res. Dev.*, **22**, 40 (1983).
8. Lewis, J. M., Kydd, R. A., Boorman, P., M., Van Rhyn, P. H., *Appl. Catal. A* **84**, 103 (1992).
9. Jian, M., Rico Cerda, J. L., Prins, R., *Vth Workshop on Hydrotreating Catalysis, European Section*, 225 (1995).
10. Jian, M., Prins, R., *Catal. Lett.*, **35**, 193 (1995).
11. Atasanova, P., Tabakova, T., Vladov, Ch., Halachov, T., Lopez Agudo, A., *Appl. Catal.* A, **161**, 105 (1997).
12. Mangnus, P. J., Van Veen, J. A. R., Eijsbouts, S., De Beer, V. H. J., Moulijn, J. A., *Appl. Catal.* **61**, 99 (1990).
13. Iwamoto, R., Grimblot, J., *Adv. Catal.*, **44**, 417 (1999).
14. Chadwick, D., Aitchison, D. W., Badilla-Ohlbaum, R., and Josefsson, L., *Stud. Surf. Sci. Catal.* **16**, 323 (1982).

---

15. Eijsbouts, S., van Gestel, J. N. M., van Veen, J. A. R., de Beer, V. H. J., Prins, R., *J. Catal.*, **131**, 412 (1991).
16. López Agudo, A., López Cordero, R., Palacios, J. M., Fierro, J.L., *Vth Workshop on Hydrotreating Catalysis, European Section, Lille- Villeneuve d'Ascq*, 237 (1995).
17. Robinson, W. R. A. M., van Gestel, J. N. M., Korányi, T. I., Eijsbouts, S., van der Kraan, A. M., van Veen, J. A. R., and de Beer, V. H. J., *J. Catal.* **161**, 539 (1996).
18. Li, W., Dhandapani, B., and Oyama, S.T., *Chem. Lett*., 207 (1998).
19. Oyama, S. T., Clark P., Teixeira da Silva, V. L. S., Lede, E. J., Requejo, F. G., *J. Phys. Chem. B* **105**, 4961 (2001).
20. Clark, P., Li. W., Oyama, S. T., *J. Catal.* **200**, 140(2001).
21. Stinner, C., Prins, R., Weber, Th. , *J. Catal*. **191**, 438(2000).
22. Stinner, C., Prins, R., Weber, Th., *J. Catal.* **202**, 187 (2001).
23. Nozaki, F., Kitoh, T., Sodesawa, T., *J. Catal.*, **62**, 286 (1980).
24. Nozaki, F., Tokumi, M., *J. Catal.*, **79**, 207 (1983).
25. Nozaki, F., Adachi, R., *J. Catal.* **40**, 166 (1975).
26. Wang, W., Qiao M., Li, H., Deng, J., *Appl. Catal.* A: **166,** L243 (1998).
27. Robinson, W. R. A. M., van Gestel, J. N. Korányi, M , Eijsbouts, T. I. , S. , van der Kraan, A. M , van Veen, J. A. R., de Beer, V. H. J., *J. Catal.* **161**, 539 (1996).
28. Lee, S. -P., Chen, Y.-W., *J. Mol. Catal.* A **152**, 213 (2000).
29. Li, H., Wang, W., Li, H., Deng, J.-F. , *J. Catal.* **194**, 211 (2000).
30. Guinier, A. "X-Ray Diffraction in Crystals, Imperfect Crystals, and Amorphous Bodies", p. 121, W. H. Freeman and Company, San Francisco, 1963.

---

31. Warren, B.E., " X-Ray Diffraction", p. 254, Addison-Wesley Publishing Company, Menlo Park, California, 1969.

32. Cullity, B.D., "Elements of X-Ray Diffraction", 2nd Ed., p. 102, Addison-Wesley Publishing Company, Menlo Park, California, 1978.

33. Ramanathan, S., Oyama, S. T., *J. Phys. Chem*., **99** (44), 16365 (1995).

34. Carlsson, B., Gö lin, M., and Rundqvist, S., *J. Sol. St. Chem.* **8**, 57 (1973).

35. Rundqvist, S., *Acta Chem. Scand.* **16**, 992 (1962).

36. Rundqvist, S., *Acta Chem. Scand.* **16**, 287 (1962).

37. Powder Diffraction Data Files, JCPDS International Center for Diffraction Data, Swathmore, PA, 1992.

38. St. Clair, T. P., Dhandapani, B., Oyama, S. T., *Catal. Lett.* **58**, 169 (1999).

39. St. Clair, T. P., Oyama, S. T., Cox, D. F., *Surf. Sci.* **468**, 62 (2000).

40. Boudart M., Djéga-Mariadassou G., "Kinetics of Heterogeneous Catalytic Reactions, Physical Chemistry: Science and Engineering", p.57, Princeton University Press, Princeton, New Jersey, 1984.

41. O'Keeffe, M., Diffusion in Oxide and Sulfides, Sintering and Related Phenomena; Proc. Intl. Conf., Kuczynski, G. C., Hooton, N. A., and Gibbon, C. F., Eds., Gordon and Breach, New York, 1967.

42. Bruke, J., "The Kinetics of Phase Transformations in Metals", Pergamon, Oxford, 1965.

43. Dhandapani, B., St. Clair, T., Oyama, S. T., *Appl. Catal. A: Gen.* **168**, 219 (1998).

44. Ramanathan, S., Yu, C. C., Oyama, S. T., J. Catal. **173**, 10 (1998).

45. Wang, X., Lee, Y.-K., Oyama, S. T., Bando, K., Requejo, F. G., J. Catal., Submitted.

Chapter 3

XAFS Studies of the Effect of Phosphorus Content in Nickel Phosphide Catalysts

3.1 Introduction

For the silica-supported iron group compounds, Fe_2P, CoP, Co_2P and Ni_2P (1,2,3) activity has been found to be moderate, with Ni_2P/SiO_2 having the highest activity, especially for hydrodenitrogenation in the previous chapter. However, these catalysts suffered from a tendency to deactivate with time on stream (1). This chapter examines the effect of phosphorus content on the performance of supported Ni_2P/SiO_2. A remarkable effect was observed on increasing the phosphorus content, which greatly increased the activity and stability of the catalysts, making this one of the best performing materials for hydroprocessing.

Phosphorus in the form of phosphate has been investigated and recommended as a secondary promoter in hydroprocessing Co-Mo and Ni-Mo sulfide catalysts over a period of almost forty years, and is used in a number of commercial catalysts (4). Many researchers have studied the effect of phosphorus in sulfide catalysts (5,6,7,8), and the topic has been reviewed by Iwamoto and Grimblot (9). An extensive literature reports on various effects of phosphate in the catalysts. Many studies describe a beneficial effect of phosphorus in catalytic activity in hydrodesulfurization (HDS) (10,11,12,13,14,15,16), hydrodenitrogenation (HDN) (13,14,15,17,18,19,20), and hydrogenation (HYD) capability (21,22,23). In some instances, no improvement in reactivity by phosphorus is reported

(24). The results presented in that paper indicated that P added to MoS_2/Al_2O_3 catalysts acted directly on the support to form $AlPO_4$, and it was speculated that weaker interactions of MoS_2 with the support surface increased the stacking of MoS_2 layers. Most studies find an enhancement in activity, however, and offer several explanations for the effect of P. These include stabilization of solutions of high metal concentrations that can yield a more uniform impregnation (25), improvement of the resistance to coking and increased support strength and stability (26,27), improvement of the dispersion of the Mo and W active phases (4,10,11,12), optimization of acidity (4,28), formation of a new kind of active site with direct participation of phosphorus (29), and alteration of the reaction mechanism (15,30,31). The positive effect of phosphorus depends on the concentration and the method of catalyst preparation and may be negative when these are not properly controlled (4,15,21).

Although considerable attention has been placed on understanding the role of phosphorus in Mo- and W-based hydrotreating catalysts, until recently, phosphorus compounds themselves have not been studied in hydroprocessing (1,2). This paper discusses the importance of controlling the amount of phosphorus in the preparation of supported catalysts in order to ensure formation of the active phosphide phase without blocking sites.

3.2 Experimental

3.2.1 Synthesis

The materials and gases used in this chapter were the same as those in the previous chapter. A series of novel, high-activity hydroprocessing catalysts, NiP_x/SiO_2, was successfully prepared by means of temperature-programmed reduction (TPR), keeping the nickel content constant and varying the phosphorus content. The samples prepared had Ni/P ratios of 2/1, 1/1, 1/1.8, 1/2, 1/2.2, and 1/3 and were synthesized as before in two steps. In the first step, aqueous phosphate solutions were prepared by reacting metal nitrates with ammonium phosphate and these were used to impregnate silica by the incipient wetness impregnation method. In the second step, these phosphates were reduced to phosphides by the method of temperature-programmed reduction. The preparation of nickel phosphate on silica with Ni/P ratio of 1/1 is presented below to illustrate the process. The loadings of all samples are listed in Table 3.1.

Table 3.1. Quantities used in the preparation of the samples

Sample Ni/P	Materials Used			Phosphide Loading (wt % MP_x)
	Silica (g)	Metal Nitrate (mol)	$(NH_4)_2HPO_4$ (mol)	
2/1	20	0.0231	0.0156	7.90
1/1	20	0.0231	0.0231	9.39
1/1.8	20	0.0231	0.0416	11.68
1/2	20	0.0231	0.0462	12.23
1/2.2	20	0.0231	0.0508	12.78
1/3	20	0.0231	0.0693	14.91

Prior to use, the silica was dried at 393 K for 3 h and calcined at 773 K for 6 h. The incipient wetness point of the silica was found to be 2.2 cm^3g^{-1}. In the fist step of preparation, 3.05 g (23.12 mmol) of ammonium phosphate $(NH_4)_2HPO_4$ were dissolved in 10 cm^3 distilled water in a flask to form a transparent colorless solution, and 6.72 g (23.12 mmol) of nickel nitrate ($Ni(NO_3)_2\cdot6H_2O$) were then added. The clear solution immediately turned into a light color mixture with some precipitate. A few drops of nitric acid were added in order to dissolve the precipitate and this resulted in a clear green solution, which was further diluted to a volume of 44 cm^3. The solution was impregnated on 20 g of silica. After impregnation, the powder was dried at 393 K for 3 h and calcined at 773 K for 6 h. The calcined sample was ground with a mortar and pestle, pelletized with a press (Carver, Model C) and sieved to particles of diameter between 650 μm and 1180 μm. In the second step of preparation, temperature-programmed reduction (TPR) was utilized to convert the phosphate into phosphide. The reduction was carried out in a U-shaped quartz reactor placed in a furnace controlled by a temperature programmer (Omega Model CN 2000). The temperature was monitored by a local chromel-alumel thermocouple placed in a thermowell near the center of the reactor bed. The H_2 flow rate was set at 1000 $\mu mol\ s^{-1}$ (1500 cm^3 NTP min^{-1}) per gram of sample. A portion of the exit gas flow was sampled through a leak valve into a mass spectrometer (Ametek/Dycor Model MA 100) and the masses 2(H_2), 4(He), 15(NH), 18(H_2O), 28(N_2), 31(P), 32(O_2), 34(PH_3), 44(CO_2), 62(P_2) were monitored during the experiment, and these and the temperature in real time were recorded by an on-line computer. At the end of the temperature program, the sample was cooled in helium to room temperature, and was passivated in a 0.5 % O_2/He flow for 2 h.

3.2.2 Characterization

The synthesized materials were characterized by CO chemisorption, N_2 physisorption, x-ray diffraction (XRD) and extended x-ray absorption fine structure measurements (EXAFS). Irreversible CO uptake measurements were used to titrate the surface metal atoms and to provide an estimate of the active sites on the catalysts. Uptakes were obtained after passivation and reduction, which is referred to here as *ex situ* chemisorption. Usually, 0.2 grams of reduced sample were loaded into a quartz reactor and pretreated in H_2 at 723 K for 2 h. After cooling down to room temperature in He, pulses of CO in a He carrier flowing at 26.7 μmol s^{-1} (40 cm^3 NTP min^{-1}) were injected through a sampling valve and the mass 28 (CO) signal was monitored with a mass spectrometer.

BET surface area measurements were carried out right after the CO uptake determinations, using a similar technique. Adsorption at liquid nitrogen temperature was performed using a 30 % N_2/He stream, and the desorption area obtained after rapid heating was compared to the area of a calibrated volume (35.4 μmol). The surface area was calculated from the one-point BET equation.

X-ray diffraction (XRD) patterns of both the fresh and spent samples were determined with a Scintag XDS-2000 powder diffractometer operated at 45 kV and 40 mA, using Cu Kα monochromatized radiation (λ=0.154178 nm). Crystal size, specific surface area and metal site density were calculated by the methods described in Chapter 2.

In order to understand the effect of the phosphorus content on the structure of the catalysts, the samples were examined using EXAFS (32). Nickel K-edge EXAFS were obtained for fresh and spent samples with Ni/P ratios of 2/1, 1/2 and 1/3. The low concentration of the active phase on the catalysts made their detailed characterization by x-ray diffraction analysis difficult. For freshly prepared samples the catalysts were loaded into glass cells with Kapton windows without exposure to the atmosphere, and these were glass-blown shut to protect the samples. For the spent catalysts, samples were taken from the hydroprocessing reactions, washed with hexane, and then pretreated in He flow before loading them in the Kapton cells. The measurements were made in transmission mode at the XAS beam line at the LNLS-National Synchrotron Light Laboratory in Campinas, Brazil with a 1.4 GeV ring energy and a 100-150 mA ring current. The monochromator was equipped with a channel cut Si (220) crystal and the energy resolution was about 1 eV.

Comparison of the EXAFS spectra of the catalysts were made with bulk standards. The standards were Ni_2P (Cerac, 99.5 %), NiO (Cerac, 99 %), NiS (Cerac, 99.9 %), $NiCO_3[Ni(OH)_2]\cdot 4H_2O$ (Aldrich), NiS_2, Ni_3S_5, and $NiPS_3$. The latter three compounds were synthesized by placing stoichiometric amounts of Ni (Aldrich, 99.8 %), S (EM Science, 99 %), and red P (Aldrich, 99 %) fine powders in sealed quartz ampules and heating (1 K/min) to 1073 K and maintaining this temperature for 100 h. XRD confirmed the phase purity of the prepared standards. The EXAFS measurements of the standards was carried out in beamline BL12B at the Photon Factory, Tsukuba, Japan, and in beamline X18B at the Brookhaven National Laboratory. Both were operated at close to 2.5 GeV with a 400 mA ring current.

3.2.3 Reactivity studies

Hydrotreating activity of the samples was tested in a three-phase, packed-bed reactor operated at 3.1 MPa and 643 K for hydrodenitrogenation (HDN), hydrodesulfurization (HDS) and hydrogenation (HYD) with a model petroleum liquid containing 2000 ppm nitrogen (quinoline), 3000 ppm sulfur (dibenzothiophene), 500 ppm oxygen (benzofuran), 20 wt.% aromatics (tetralin) and balance aliphatics (tetradecane). The schematic of the testing system was shown elsewhere (33). Briefly, the testing unit consisted of three parallel reactors immersed in a fluidized sand bath (Techne, Model SBL-2). The temperature of the reactors was controlled by a temperature controller (Omega, Model 6051). The reactors were 19mm/16mm o.d/i.d. 316 SS tubes with a central thermocouple monitoring the temperature of the catalyst bed. The catalysts were in the form of pellets (16/20 mesh) and were supported between quartz wool plugs in a 13 mm i.d. 316 stainless steel basket. The hydrogen flow rate was set to 100 $\mu mol s^{-1}$ (150 cm^{-3} NTP min^{-1}) with a mass flow controller (Brooks, Model 5850E), and the feed liquid flow rate (5 cm^{-3} h^{-1}) was metered from burettes by high-pressure liquid pumps (LDC Analytical, Model NCI 11D5). Quantities of catalysts loaded in the reactor corresponded to the same amount of *ex situ* CO uptake (70 μmol). Prior to reactivity measurements, the catalyst samples were pretreated in exactly the same manner as for the *ex situ* CO uptake measurements. Hydrotreating samples were collected every two or three hours in sealed septum vials and were analyzed off-line with a gas chromatograph (Hewlett Packard, 5890A) equipped with a 0.32 mm i.d. x 50 m fused silica capillary column (CPSIL-5CB, Chrompack, Inc.) and a flame ionization detector. The product of dibenzothiophene HDS was primarily biphenyl. The products of quinoline reaction were the denitrogenated molecules propylbenzene and propylcyclohexane, and the N containing species,1,2,3,4-

tetrahydroquinoline, 7,8,9,10-tetrahydroquinoline, and propylaniline. The production of the latter is referred to as HDA.

3.3 Results and discussion

Ni_2P (34) adopts the hexagonal Fe_2P structure (Space group: $P_{\bar{6}2m}$, D_{3h}^2, Struckturbericht notation: revised C22) with lattice parameters, a = b = 0.5859 nm, c = 0.3382 nm. The crystal structure (Fig. 3.1) and lattice parameters can be used to calculate a bulk density (ρ = 7.09 g cm^{-3}) and the average surface metal atom density ($\bar{n}$ = 1.01 x 10^{15} atoms cm^{-2}) of the solids (1).

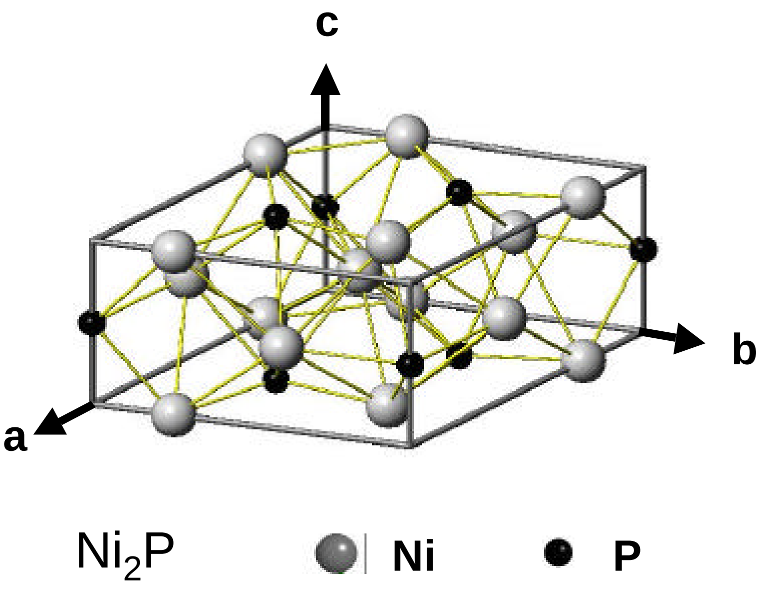

Figure 3.1. Crystal structure of Ni_2P

The preparation of the supported phosphides was carried out in two stages. First, a solution of the metal and phosphorus components was impregnated on the carrier silica support and the material was dried and calcined to form supported phosphates. Second, the phosphates were transformed into phosphides by temperature programmed reduction (TPR) (Figs. 3.2,3). Only results for mass 18 (H_2O), and 34 (PH_3) are shown, as the other monitored masses were featureless or provided no additional information. The results for the samples with Ni/P ratios of 1/1.8 and 1/2.2 are not presented in the figures since they were similar to those of the sample with Ni/P ratio of 1/2.

The TPR traces of mass 18 showed two systematic trends for the samples with different Ni/P ratios. First, for lower P contents (Fig. 3.2a-c), the TPR traces showed more peaks and a more complicated overall reduction pattern than that of higher P samples (Fig. 3.2d-f). Second, for higher P contents, all the reduction peaks, including the initial and final features, were shifted to higher temperatures. These trends are reasonable. For lower P contents, the precursor probably contains more nickel compounds like nickel oxide and nickel oxy-phosphates, and their separate reduction results in different peaks. Since nickel oxides are easily reducible, the TPR peaks appear at lower temperatures. It is possible that some metallic Ni or a nickel phosphide phase of lower P content was formed which assisted the reduction of other species. For higher P contents (Fig. 3.2d-2f), the nickel is likely to be in the form of phosphate and reaction occurs at the high intrinsic reduction temperature, T_p, of this main phosphate phase. As can be seen from Figs. 3.2d-f, the peak temperature of the reduction traces was around 800 K, and was characteristic of the reduction of bulk nickel phosphate (1). Because this temperature was high, successive reduction stages could not be resolved, and the whole process appeared to occur in one step. It should be noted that in these TPR measurements there was an inadvertent change in heating rate at ~ 630 K. This resulted in a drop in intensity, especially for Figs. 3.2a-c, but it does not affect the interpretation of the data.

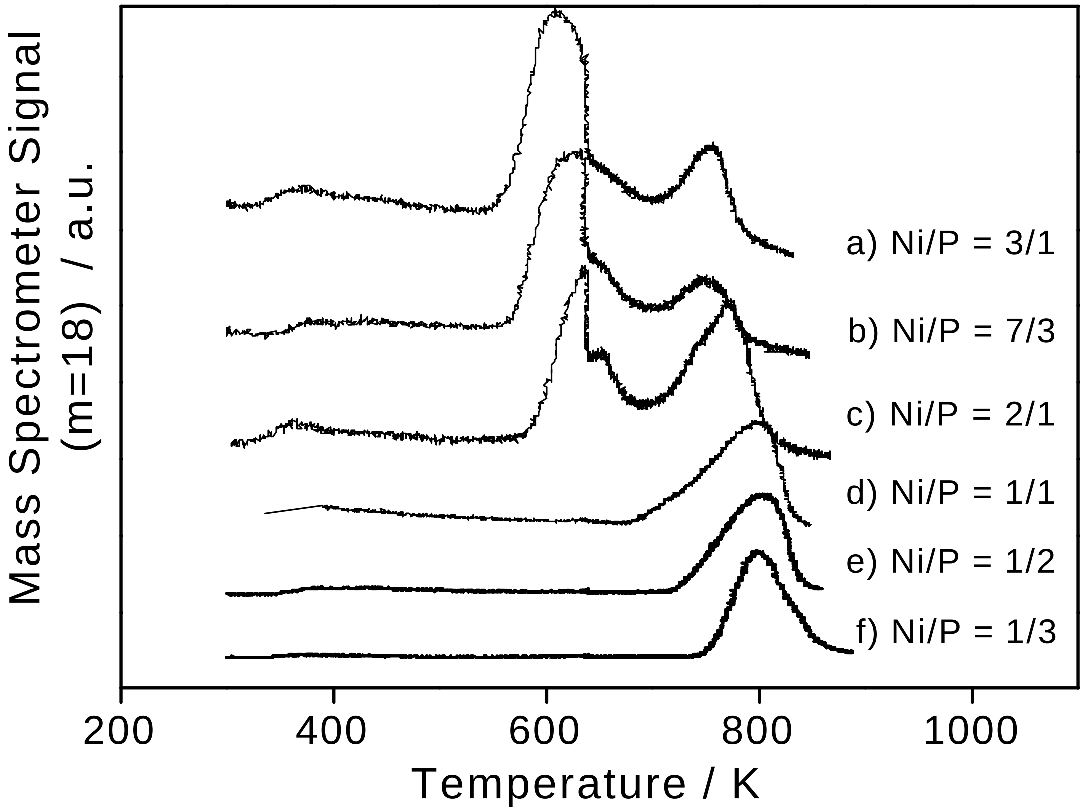

Figure 3.2. Mass 18 (H_2O) signal from temperature-programmed reduction of the samples at β= 1 K/min (0.01667 K s^{-1}).

The TPR trace for mass 31 (P) followed exactly that of mass 34 (PH_3) and is not reported here. It is likely that the P observed was a fragmentation product of PH_3. The trace for mass 62 (P_2) was completely flat and suggests that phosphorus was not volatilized from the sample.

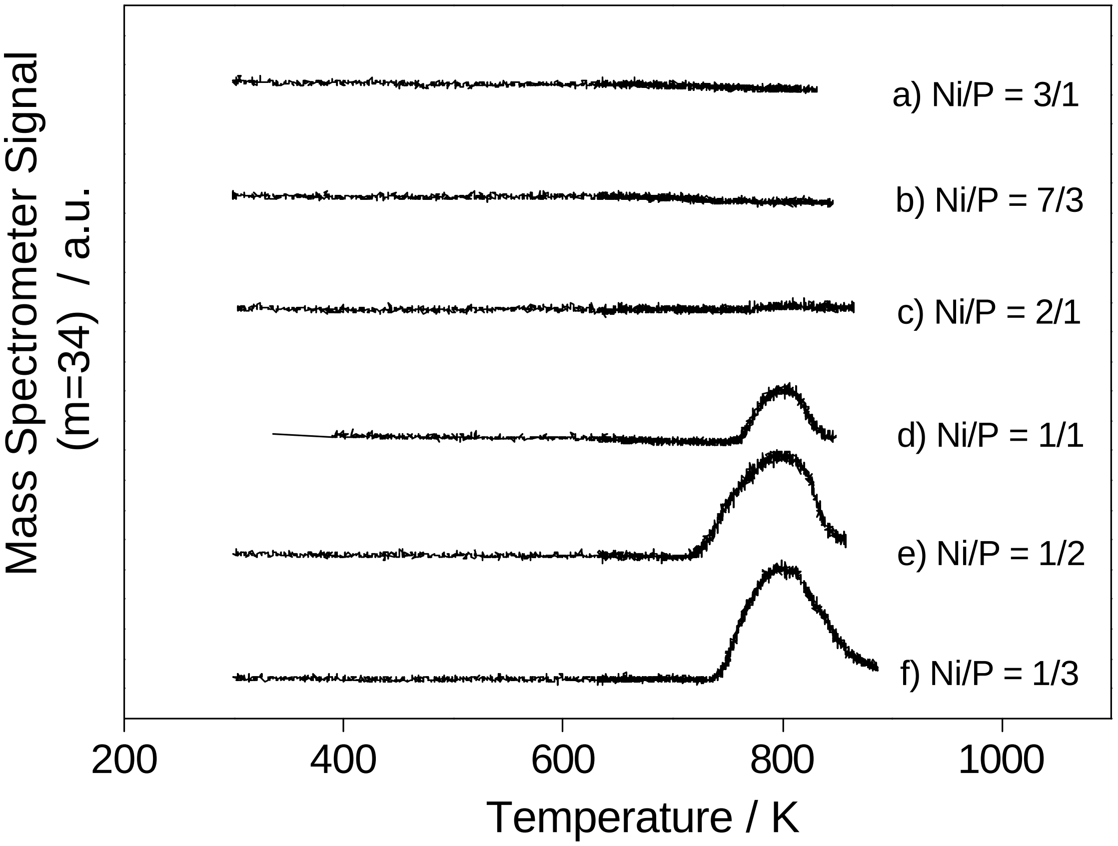

Figure 3.3. Mass 34 (PH_3) signal from temperature-programmed reduction of the samples at β= 1 K/min (0.01667 K s^{-1}).

All these samples showed the loss of P during the synthesis. For the samples with higher P contents, PH_3 was seen in the TPR traces (Fig. 3.3). For the samples with lower P contents, no P or PH_3 was obtained during the reduction. However, loss of P might have happened during the calcination at 773 K, since a small amount of a white solid was observed to have sublimed onto the lid of the ceramic calcination vessel. As explained in Chapter 2, this was likely to be P_2O_5 with a melting point of 563 K, and sublimation temperature of 787 K. There is also the strong likelihood that some extra phosphorus in amorphous form remained on the support.

Table 3.2. Catalyst characterization results

Ni:P Ratio	Sample	Surface area S_g $m^2\ g^{-1}$	CO uptake $\mu mol\ g^{-1}$	Metal site density $\mu mol\ g^{-1}$	D_c nm
2/1	Fresh	90	49	42	-
	Spent	107	18	42	26
1/1	Fresh	98	15	67	-
	Spent	100	13	67	20
1/1.8	Fresh	111	24	153	-
	Spent	110	14	153	11
1/2	Fresh	97	28	169	-
	Spent	89	24	169	9
1/2.2	Fresh	106	27	186	-
	Spent	103	30	186	9
1/3	Fresh	100	32	311	-
	Spent	75	16	311	7

The BET specific surface areas (S_g) and CO chemisorption uptakes of the samples are listed in Table 3.2. The specific surface areas (S_g) of the samples were close to that of the support (90 m^2g^{-1}). Deviations were due to experimental error with the flow technique. The experimental CO uptakes of the samples are reported in the fourth column of Table 3.2. The fresh sample with Ni/P ratio of 2/1 had the highest CO uptake (49 μmol g^{-1}), while the rest of the samples had uptakes between 15-32 μmol g^{-1}. Other fresh samples were all close. The crystallite sizes (D_c) calculated from the Scherrer equation ($D_c = K\lambda/\beta \cos\theta$), (35) are listed in the last column of Table 3.2. The analysis shows that crystallite size gets smaller with increase in P content. As explained in Chapter 2, from the crystallite size, it is possible to calculate an effective surface are a ($S = 6/\rho D_c$) of the crystallites assuming cubic or spherical geometry, and from this a theoretical metal site concentration, (L). This surface concentration is given by (L) = S $\bar{n}$ f, where f is the fractional weight loading of the sample (Table 3.1), and $\bar{n}$ is again the average surface metal atom density. The results are listed in the fifth column of Table 3.2, and show that the metal site concentration increases with increase in the P content in the samples. In fact, however, the CO uptakes for the fresh samples starting with a Ni/P ratio of 1/1 increase only slightly with P content. This indicates that the extra phosphorus is possibly blocking sites. This will be discussed further later.

X-ray diffraction patterns of the fresh samples with Ni/P ratios, 2/1, 1/1, 1/2, 1/3 are presented in Figure 3.4. Here, again, the patterns for the samples with Ni/P ratios of 1/1.8 and 1/2.2 are not shown in the figure since they were similar to the one for Ni/P = 1/2. The diffraction patterns displayed two systematic features. First, the sample with the lowest P content (Fig. 3.4a) contains two phases (Ni_2P and $Ni_{12}P_5$) in the product, while the samples with the higher P contents had just one phase, Ni_2P. The formation of $Ni_{12}P_5$ at lower P content is understandable as $Ni_{12}P_5$ contains a lower proportion of P than Ni_2P. Second, the x-ray diffraction peaks became less intense and weaker with increasing content of P. This indicates the formation of smaller crystallites of Ni_2P with increase in P content as is shown in the last of column in Table 3.2, and is a likely consequence of a greater dispersion of the precursor phosphate, which is easier to form with higher P contents.

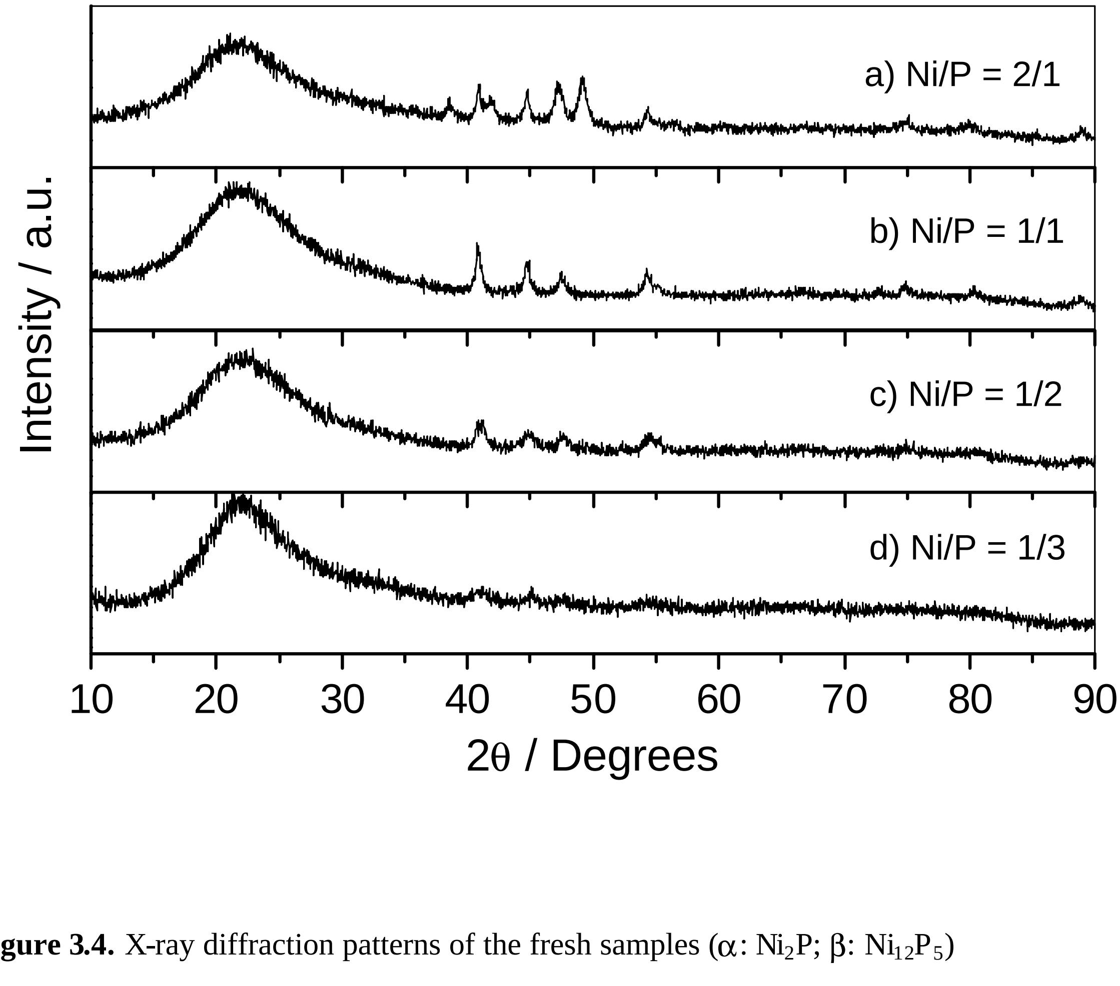

Figure 3.4. X-ray diffraction patterns of the fresh samples (α: Ni_2P; β: $Ni_{12}P_5$)

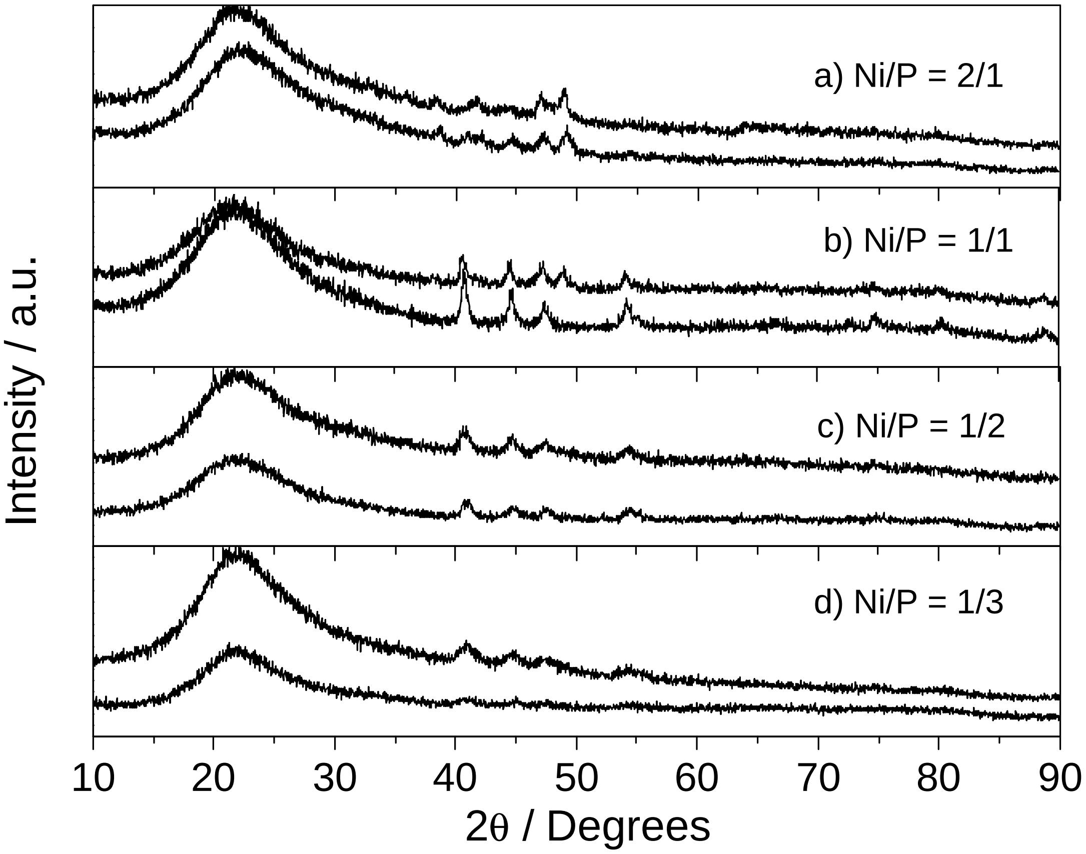

Figure 3.5. Comparison of X-ray diffraction patterns for the fresh samples and the spent samples

X-ray diffraction patterns were also obtained for the spent samples (Fig. 3.5, upper curve in each frame). The figure shows that there was no change in pattern for the sample with Ni/P ratio of 2/1 (Fig. 3.5a), indicating that the Ni_2P and $Ni_{12}P_5$ were stable phases at hydrotreating conditions. For the samples with Ni/P ratio of 1/2 and 1/3, the nickel phosphide phase became more crystallized after the hydrotreating reaction (Fig. 3.5c,d). This is understandable due to the prolonged exposure (> 100 h) to the hydrotreating temperature of 643 K. For the sample with Ni/P ratios of 1/1 (Fig. 3.5b), the x-ray diffraction pattern after reaction shows the appearance of a new peak, which is assigned to $Ni_{12}P_5$. The basis for the assignment to $Ni_{12}P_5$ is shown in Fig. 3.6, which superposes the pattern for the spent sample with Ni/P = 1/1 to the patterns of other nickel phosphide, nickel sulfide, and nickel phosphide sulfide PDF reference patterns. The main peaks match those of Ni_2P, but the minor features can be attributed to the presence of a small amount of $Ni_{12}P_5$. It is possible that the Ni/P = 1/1 sample may have been slightly phosphorus

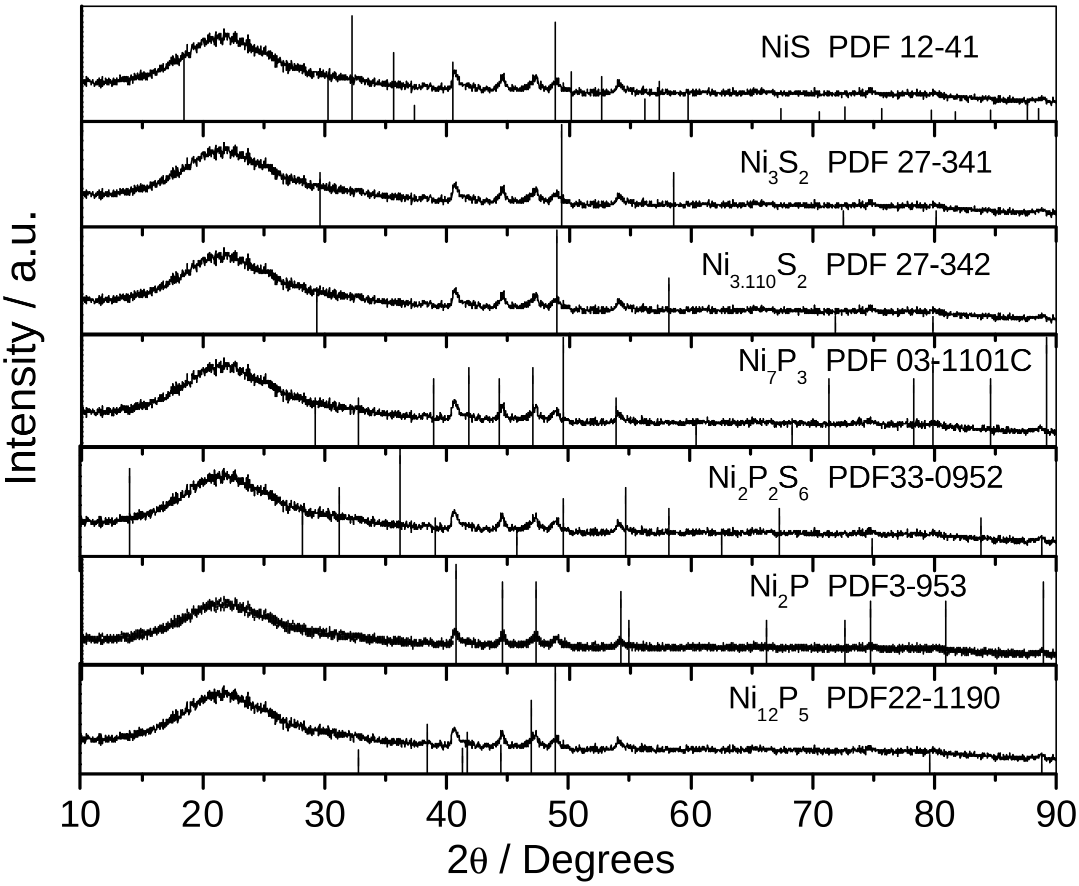

Figure 3.6. Superposition of the X-ray diffraction pattern of the spent sample (Ni/P=1/1) with different references.

deficient to start out with, and the prolonged exposure to the reaction temperature caused the $Ni_{12}P_5$ to nucleate. It is also possible that the sample lost some phosphorus during reaction, though this is less likely as it was not observed with the other samples.

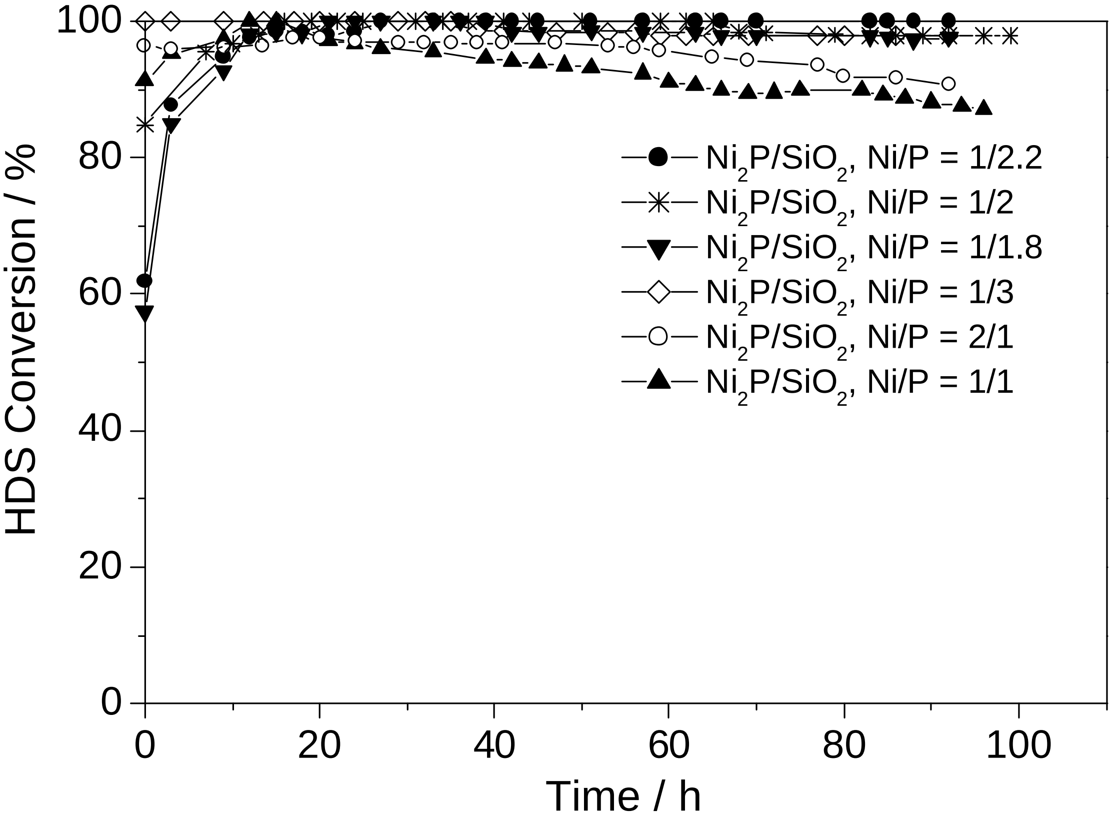

Figure 3.7. Hydrodenitrogenation performance of supported catalysts

Figures 3.7-8 present the time course of HDS and HDN activities on the series of phosphide catalysts. Figure 3.9 shows the effect of phosphorus content on the HDS and HDN activities. The HDS activity was uniformly high for all the samples, with just slight reductions for the samples with Ni/P ratios of 2/1 and 1/1. The sample with Ni/P ratio of 1/2.2 had the highest HDS conversion, essentially 100 %, although the other three samples with Ni/P ratios of 1 /1.8, 1/2 and 1/3 had the very close HDS conversion of 98 %. The small effect of the P content was close to the error in the measurements of 1-2 %, but the trends are probably real as shown more clearly in the HDN reactions. In fact, the samples with Ni/P ratios of 1/1.8 and 1/2.2 were prepared and tested to confirm the high activity results of the sample with Ni/P ratio of 1/2.

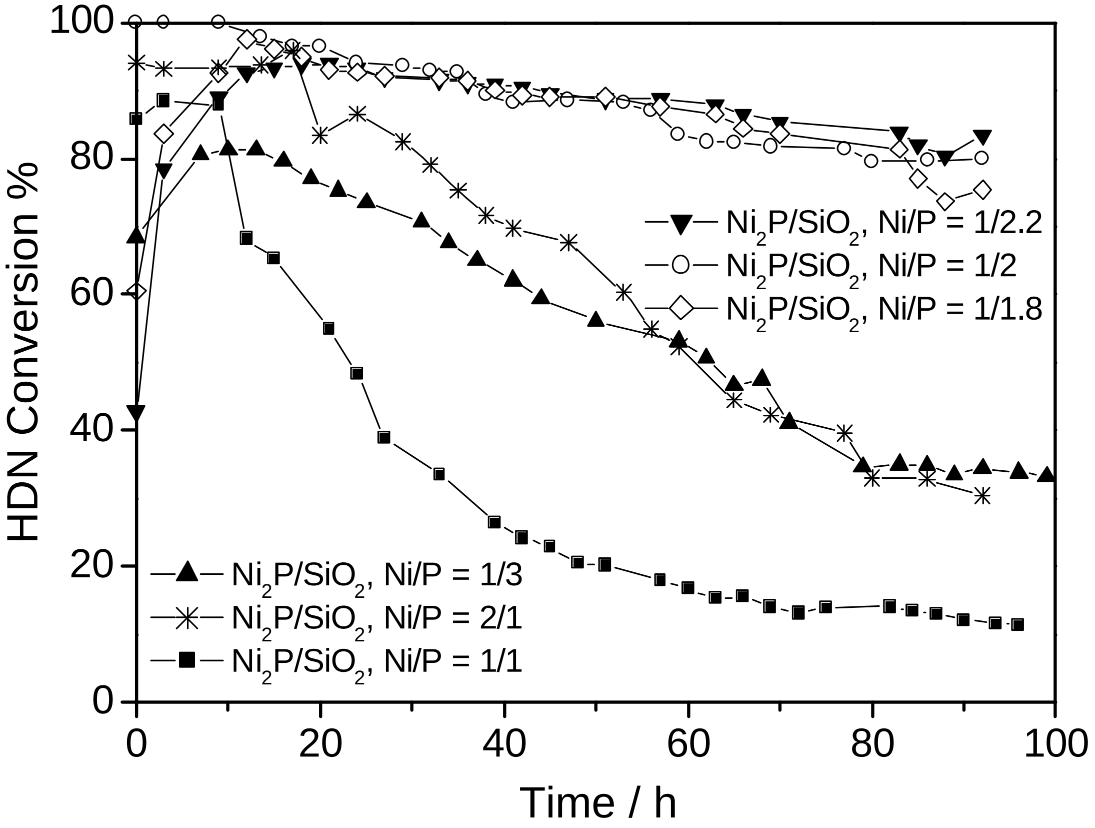

Figure 3.8. Hydrodesulfurization performance of supported catalysts

For the HDN reaction, the P content had a strong effect on the quinoline reaction. The samples with Ni/P ratios of 1/1.8, 1/2 and 1/2.2 followed similar time courses with slight deactivation resulting in final HDN conversions between 80 % to 90 % (Fig. 3.8).

The other three samples reached a far lower HDN activity, which was below 50 %, especially for the highest and lowest P content samples. A comparison of all results is presented in Figure 3.9, which shows the effect of P content on the activity of all the catalysts. The best performance was obtained at a Ni/P ratio close to 1/2.

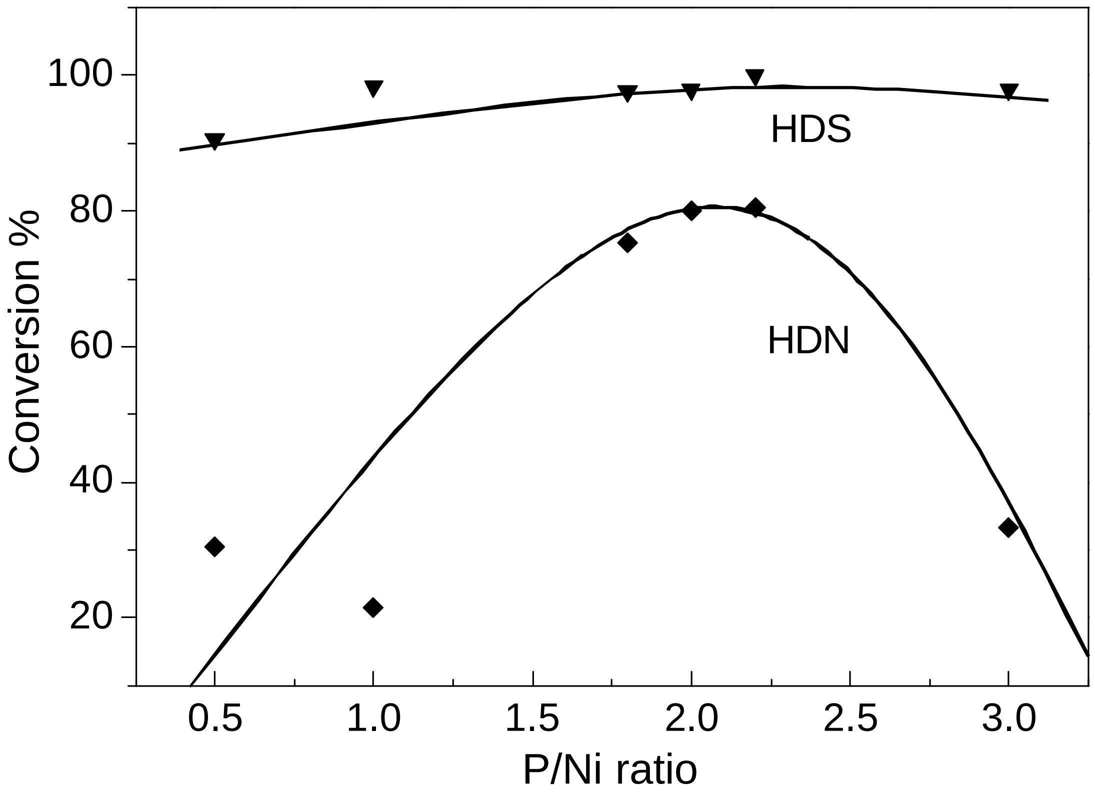

Figure 3.9. Comparison of hydroprocessing activities

The effect of P content on HDS and HDN on these samples gives insight on the nature of the active sites responsible for these reactions. The small effect of P content on HDS suggests that the reaction occurs principally on metal centers and that there is little effect of ensemble size on reactivity. Hence, the reaction is structure-insensitive. On the other hand, the relatively large effect of P on HDN suggests that P somehow participates in the reaction. HDN has been shown to proceed by β-hydride elimination on carbides and sulfides and more recently on phosphides (36). The active site requires an acid site to bind the nitrogen compound and a proximal nucleophilic site to carry out the β-H attack. Thus, the reaction is structure-sensitive. Excess P on the surface may disrupt the dual site and cause the observed maximum in activity with P content.

Previous work had shown that Ni_2P/SiO_2 (Ni/P = 1/1) was only a fair catalyst for hydroprocessing, especially for hydrodesulfurization (HDS) of dibenzothiophene (1). Also, the HDN activity declined considerably with time. In this work, the addition of excess phosphorus is seen to facilitate the formation of the active nickel phosphide phase, and to reduce deactivation.

The CO uptake for the post hydrotreating samples decreased for all samples except for the sample with Ni/P ratio of 1/2.2. This fact was more obvious for the samples with the lower P contents, as is shown in Table 3.2. For example, the CO uptake of the fresh sample with Ni to P ratio of 2/1 was 49 μmol g^{-1}, but it decreased to 18 μ mol g^{-1} after the hydrotreating. This loss of active centers may be an important reason for the deactivation of the catalysts.

In order to better understand the effect of the phosphorus content on the catalytic activity, the catalysts were examined using extended x-ray absorption fine structure (EXAFS) analysis. The top panel in Figure 3.10 shows the Ni K-edge EXAFS results for these fresh samples with Ni/P ratios of 2/1, 1/2, and 1/3. The sample with Ni/P = 2/1 (Fig. 3.10a) shows a main peak with a shoulder at lower interatomic distance. In contrast, the samples with Ni/P = 1/2 and 1/3 (Figs. 3.10b,c) display two distinct peaks. Comparison of the latter with the reference Ni_2P sample shows good agreement in the Ni-Ni and Ni-P distances. There is no such agreement with the features of NiO, $Ni(OH)_2$, and Ni metal, and this demonstrates that the predominant phase in these two supported catalysts is Ni_2P. The situation is different for the sample with the Ni/P ratio of 2/1 (Fig. 3.10a). In this case the Ni-P peak is reduced to a shoulder and the Ni-Ni peak shifts to the position of metallic Ni. It is evident that the amount of Ni_2P phase is smaller, as could be expected from the spreading of the metal and phosphorus components on the surface of the support. The lack of the Ni_2P also explains the low activity. With the Ni_2P/SiO_2 sample with the excess phosphorus (Ni/P = 3/1), the FT peak positions duly correspond to those of bulk Ni_2P. However, the intensity of the Ni-P relative to the Ni-Ni peak is now increased over that of bulk Ni_2P. The extra phosphorus probably resides on the surface of the highly dispersed particles, breaking up the catalytically active ensembles and again reducing activity.

Figure 3.11 compares the EXAFS spectra of the fresh and spent samples with Ni/P ratios of 2/1, 1/2, and 1/3. In all cases changes can be discerned in the catalysts after reaction. For the spent sample with Ni/P = 2/1, a small feature appears in between the main Ni-Ni peak and the Ni-P shoulder (Fig. 3.11a). For the spent sample with Ni/P = 1/2, the two-peak structure is retained, but there is a reduction in the Ni-Ni peak intensity (Fig. 3.11b). For the spent sample with Ni/P = 1/3, the Ni-Ni peak is almost entirely attenuated and a broad feature at lower interatomic distance appears (Fig. 3.11c). Clearly, in all cases there is disruption of the original Ni_2P phase, and this is likely due to the formation of sulfur compounds. Nickel carbide and nickel nitride are unstable at the conditions of reaction (37).

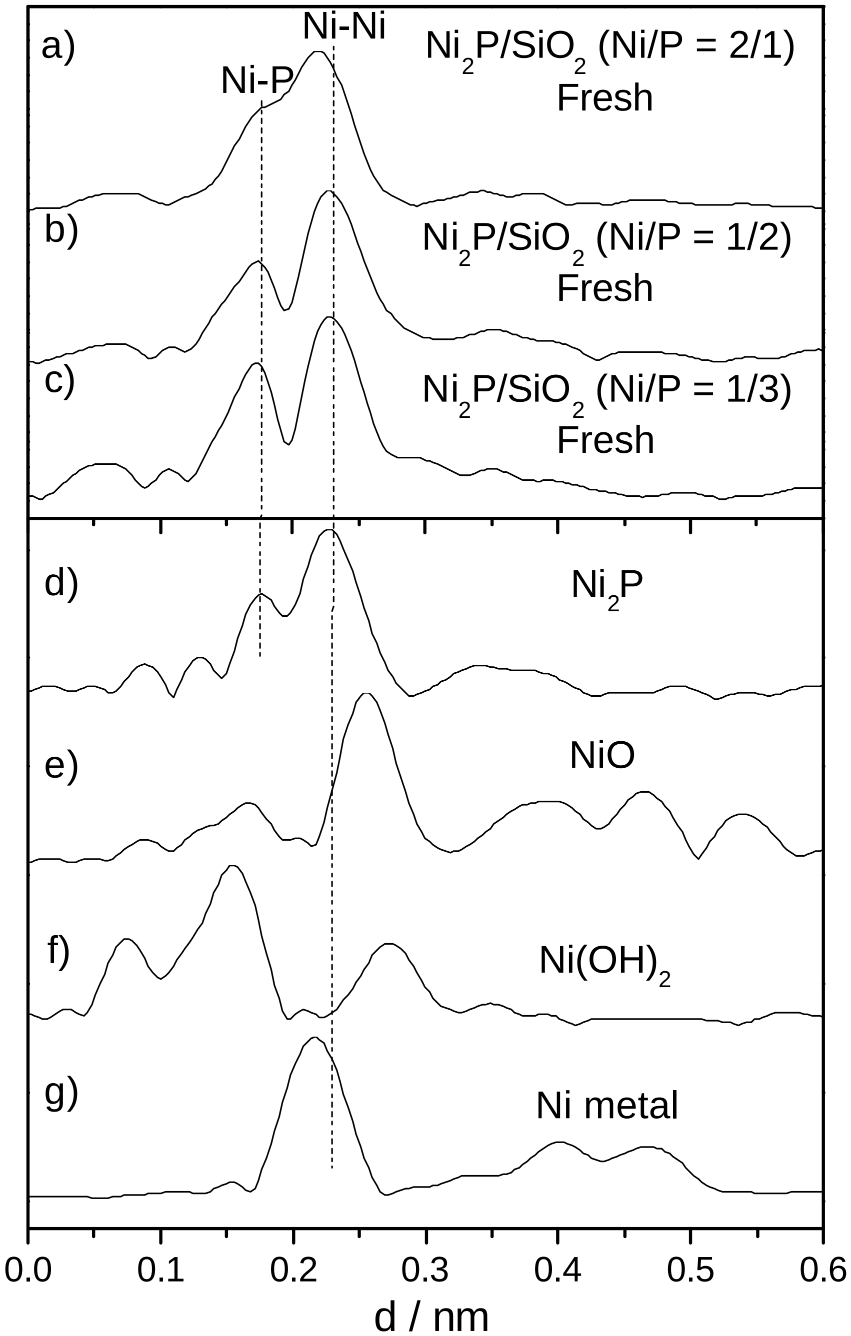

Figure 3.10. Comparison of Nickel K edge EXAFS for the fresh samples with Ni/P ratios of a) 2/1, b) 1/2, c) 1/3 and references d) Ni_2P, e) NiO, f) $Ni(OH)_2$, g) Ni metal.

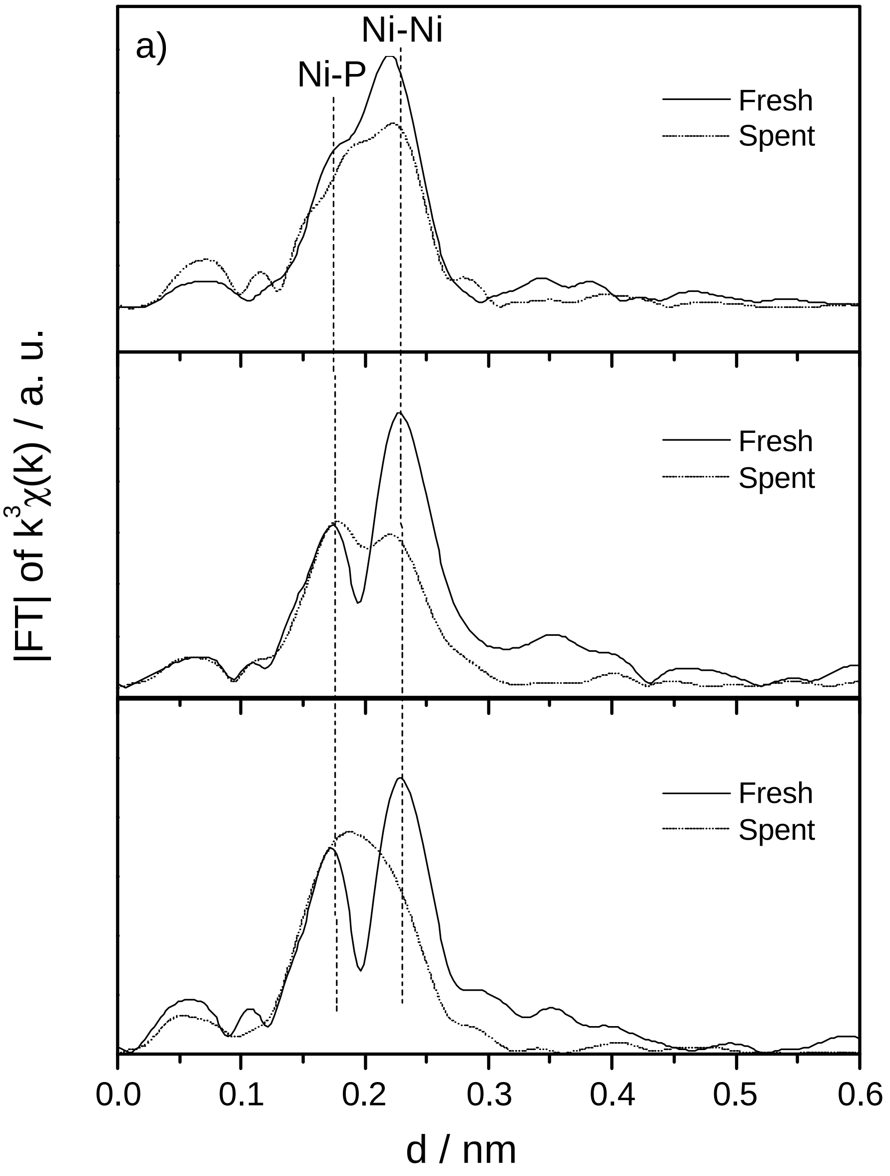

Figure 3.11. Nickel K-edge EXAFS of the fresh and spent samples with different Ni/P ratios: a) Ni/P = 2/1, b) Ni/P = ½, c) Ni/P = 1/3.

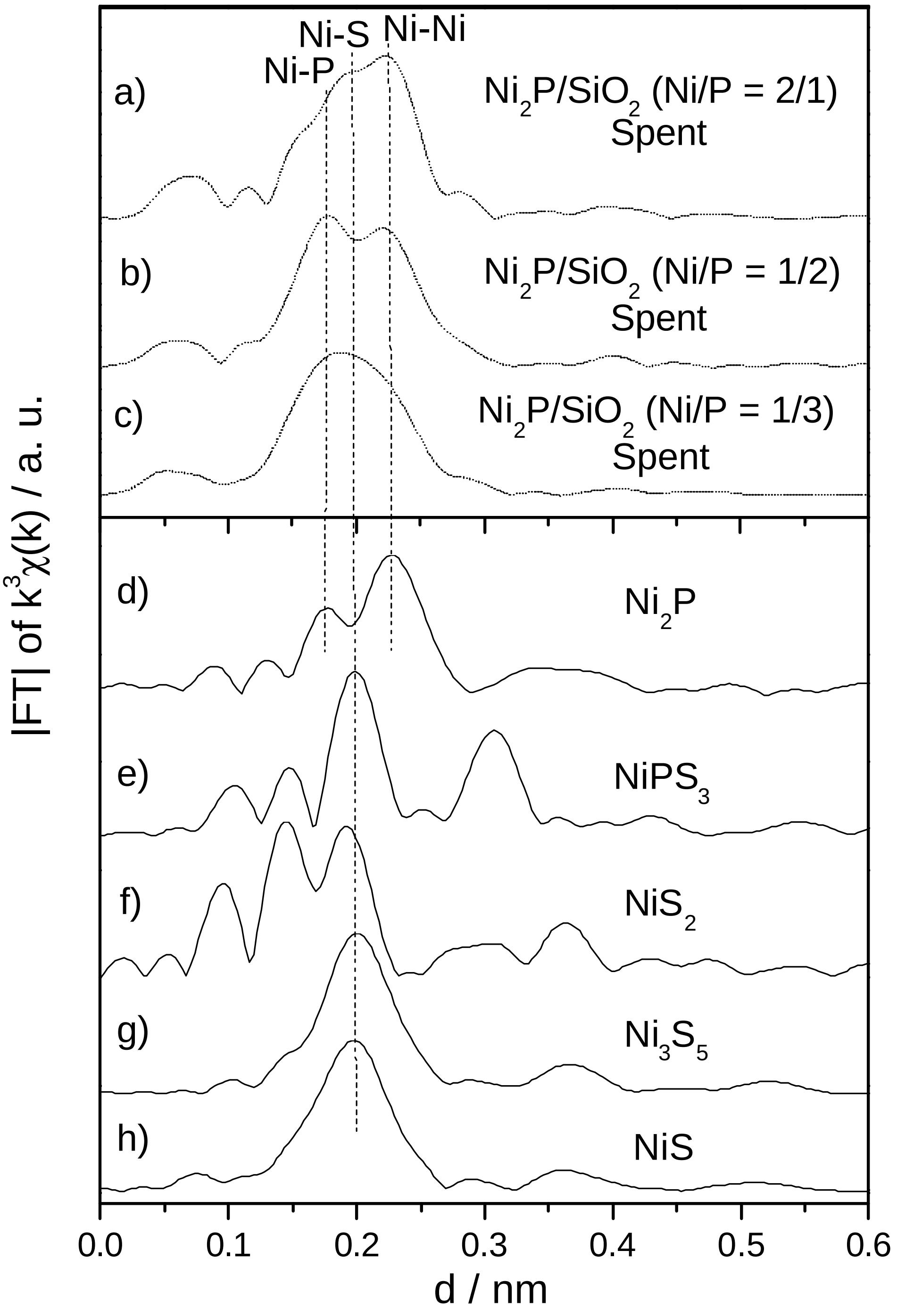

Figure 3.12. Comparison of Nickel K-edge EXAFS for the spent samples with Ni/P ratios of a) 2/1, b) 1/2, c) 1/3 and references d) Ni_2P, e) $NiPS_3$, f) NiS_2, g) Ni_3S_5, h) NiS.

The identification of the changes occurring in the spent samples was carried out by comparing their spectra to those of bulk sulfide references (Fig. 3.12). For the spent sample with Ni/P = 2/1 (Fig. 3.12a), the small feature in between the Ni-Ni peak and the Ni-P shoulder corresponds to a Ni-S distance in one of the sulfide references (Figs. 3.12e-h). The sulfide is likely a lower sulfur content material like Ni_3S_5 or NiS, because of the lack of a prominent peak at a shorter distance as appears in NiS_2 (Fig. 3.12f), or longer distance as appears in $NiPS_3$ (Fig. 3.12e). Interestingly, the sample now shows Ni-Ni and Ni-P distances that correspond to Ni_2P whereas the fresh sample showed distances displaced toward Ni metal. It is likely that the metallic portion of this sample was sulfided, but the phosphide portion was retained.

For the spent Ni_2P/SiO_2 sample with Ni/P = 1/2 (Fig. 3.12b), a two-peak spectrum with the characteristic distance of Ni_2P (Fig. 3.12d) is visible. However, peaks are broadened in comparison to the fresh sample (Fig. 3.10b) and the Ni-Ni peak is attenuated. Although not directly visible, it is likely that a Ni-S signal is hidden between the two peaks, broadening the spectra and reducing the Ni-Ni contribution. Still, the main features of the Ni_2P remain and the conclusion is that the active phase is a surface phospho-sulfide. It is unlikely to be a high-sulfur phase like $NiPS_3$, as the strong feature at long interatomic distance is missing.

For the spent Ni_2P/SiO_2 (Ni/P = 1/3), the spectrum consists of a broad feature that is likely formed from a combination of different peaks. The most likely interpretation is that there is a dominant Ni-S signal and smaller peaks due to Ni-P and Ni-Ni on both sides. It is difficult to understand why this sample should undergo greater sulfidation than the sample with Ni/P = 1/2, as it contained more phosphorus in the fresh state. However, recalling the XRD results (Fig. 3.5), that showed the sample with Ni/P = 1/3 to be more highly dispersed than the sample with Ni/P = 1/2, it can be conjectured that the smaller particle size results in a greater degree of sulfidation.

The catalytic testing showed that the activity of the phosphides was uniformly high for HDS, but went through a maximum with P content for HDN (Fig. 3.9). Separate tests with NiS_2/SiO_2 showed that it has very low activity in both HDS and HDN in agreement with results from the literature (38). These results indicate that in the supported Ni_2P/SiO_2 sample the phosphorus plays an important role in the catalytic phase and supports the conclusion that Ni-P bonding is present in all the spent samples, even though a substantial amount of Ni-S bonding is seen in the spectra. The best sample Ni_2P/SiO_2 (Ni/P = 1/2) represents an optimum where the phosphorus content and the particle size are balanced to give some sulfur tolerance with the maintenance of high catalytic activity.

The significant finding of this study was the very high activity of the nickel phosphide catalysts with Ni/P ratios close to 1/2. The sample with the Ni/P ratio of 1/2.2 had 100 % HDS and 81 % HDN conversion, which is much higher than that of a commercial catalyst, Ni-Mo-S/Al_2O_3 (Shell 324) with 76 % HDS and 38 % HDN (39). This is the highest activity which has been reported in the hydrotreating field for dibenzothiophene in the presence of a nitrogen compound.

3.4 Conclusions

Phosphorus content has a profound effect on the structure and activity of NiP_x/SiO_2 catalysts. Ratios of Ni/P $\approx$ 1/2 result in materials with excellent activity in hydroprocessing with HDS conversion of 100 %, and HDN conversion of 81 %, which are much higher than those of a commercial Ni-Mo-S/Al_2O_3 catalyst with HDS conversion of 76 % and HDN conversion of 38 %. Phosphorus content has a small effect on HDS indicating that the reaction is structure-insensitive, but a substantial one on HDN indicating that the reactions are demanding. Characterization of the catalysts by EXAFS measurements before and after reaction indicates that the active phase in the catalysts is a phospho-sulfide. The catalysts inactive for HDN, on the other hand, have pronounced sulfur content. Overall results indicated that on these novel, high activity hydroprocessing catalysts, the HDS and HDN reactions are not promoted by nickel on its own, but that phosphorus plays an important role in the reaction.

References

---

1 Wang, X., Clark, P., Oyama, S. T., *J. Phys. Chem*. 2002. In press.

2. Stinner, C., Prins, R., Weber, Th. , *J. Catal.*, **202**(1) (2001).

3. Robinson, W. R. A. M., van Gestel, J. N. M., Koranyi, T. I., Eijsbouts, S., van der Kraan, A. M., van Veen, J. A. R., de Beer, V. H. J., *J. Catal.* **161**(2), 539 (1996).

4. Lewis, J. M., Kydd, R. A., Boorman, R. M., Van Rhyn, P. H., *Appl. Catal.* A., **84**, 103 (1992).

5. Jian, M., Rico Cerda, J. L., Prins, R., *Vth Workshop on Hydrotreating Catalysis, European Section*, 225 (1995).

6. Jian, M., Prins, R., *Catal.Lett.*, **35**, 193 (1995).

7. Atasanova, P., Tabakova, T., Vladov, Ch., Halachov, T., Lopez Agudo, A., *Appl. Catal.* A, **161**, 105 (1997).

---

8. Mangnus, P. J., Van Veen, J. A. R., Eijsbouts, S., De Beer, V.H.J., Moulijn, J.A., *Appl. Catal*. **61**, 99 (1990).

9. Iwamoto, R., Grimblot, J., *Adv. Catal.*, **44**, 417 (1999).

10. Lewis, J. M., Kydd, R. A., *J. Catal.*, **136**, 478 (1992).

11. Morales, A., de Agudelo, R., *Appl. Catal.*, **23**, 23 (1986).

12. Atanasova, P., Vchyti, J., Kraus, M., Halachev, T., *Appl. Catal.*, **65**, 53 (1990).

13. Cruz Reyes, J., Avalos-Boria, M., López Cordero, R., López Agudo, A, *Appl. Catal.*, A, **120**, 147 (1994).

14. van Veen, J. A. R., Colijn, H. A., Hendriks, P. A. J. M., van Weisenes, A. J., *Fuel Proc. Tech*., **35**, 137 (1993).

15. Eijsbouts, S., van Gestel, J. N. M., , L., van Veen, J. A. R., de Beer, V. H. J., Prins, R., *J. Catal.*, **35**, 137 (1991).

16. Fitz, C. W., Rase, H. F., Ind. Eng. Chem. Prod. Res. Div., **22**, 40 (1983).

17. Dhandapani, B., Ramanathan, S., Yu, C. C., Fruhberger, B., Chen, J. G., Oyama, S. T., *J. Catal*. **176**(1), 61 (1998).

18. Tisher, R. E., Narain, N. K., Stiegel, G. J., Cillo, D. L., *Ind. Eng. Chem. Prod. Res.Div.*, **26**, 422 (1987).

19 Mickelson, G. A., Patent, 3 755 150 (1968)

20. López Agudo, A., López Cordero, R., Palacios, J. M., Fierro, J. L., *Bull. Soc. Chim. Belg*. **104**(4-5), 237 (1995).

21. Fierro, J. L. G., López Agudo, A., Esquivel, N., López Cordero, R, *Appl. Catal.*, **48**, 353 (1989).

---

22. López Cordero, R., Esquivel, N., Lázaro, J., Fierro, J. L. G., López Agudo, A., *Appl. Catal.*, **48**, 341 (1989).
23. Housm E.C., and Lester, R., *British Patent*, **807** 583 (1959).
24. Poulet, O., Hubaut, R., Kasztelan, S., Grimblot, J, *Bull. Soc. Chim. Belg. European Section*, **100**(11-12), (1991).
25. Colgan, J.D. and Chomitz , N., U. S. Patent, 3 287 280, (1966)**.**
26. Tolman, C. A., Druliner, J. P., Krusic, P. J., Nappa, M. J., Seidel, W.C., Williams,I. D., Ittel, S. D., *J. Mol. Catal.*, **48**, 129 (1988).
27. Goedken, V.L., Ercolani, C., *J. Chem. Soc., Chem. Commun.*, 378(1984).
28. Gishti, K., Iannibello, A., Marengo, S., Morelli, G., Titorelli, P. *Appl. Catal.* **12**, 381 (1984).
29. Craje, M. W. J., de Beer, V. H. J., van der Krann, A. M., *Catal. Today* **10**, 337 (1991).
30. Cerda, J. L. R., Prins, R., *Bull. Soc. Chim. B*elg. **100**, 815 (1991).
31. Mangnus, P. J., van Langeveld, A. D., de Beer, V. H. J., Moulijn, J. A., *Appl. Catal.*, **68**, 161 (1991).
32. Spectra were recorded in transmission mode using a Si(220) double crystal monochromator with a slit aperture of 0.5 nm at the XAS beamline of the LNLS National Synchrotron Light Laboratory in Campinas, Brasil.
33. Ramanathan, S., Oyama, S. T., *J. Phys. Chem*., **99**, 16365 (1995).
34. Rundqvist, S., *Acta Chem. Scand.* **16**, 992 (1962).
35. Cullity, B.D., Elements of X-Ray Diffraction, 2nd Ed., p. 102, Addison-Wesley Publishing Company, Menlo Park, California, 1978.

---

36. Schwartz, V., Teixeira da Silva, V., Oyama, S. T, *J. Mol. Catal. A: Chem*. **163**, 251 (2000).

37. Oyama, S. T, in Preparation of Solid Catalysts, Ertl, G., Knözinger, H., Weitkamp, J., Eds., Wiley-VCH Verlag GmbH, Weinheim, Germany, (1999), pp. 139-150.

38. Pecoraro, T. A., Chianelli, R. R., *J. Catal*. **67**, 430 (1981).

39. Oyama, S. T., Wang, X., Requejo, F., Sato, T., Yoshimura, Y., J. Catal. Submitted.

Chapter 4

Active Phase of Ni_2P/SiO_2 in Hydroprocessing Reactions

4.1 Introduction

The effect of Ni/P ratio on the structure and hydroprocessing behavior of NiP_x/SiO_2 (1) was studied in Chapter 3. It was found that increasing the phosphorus content to give a Ni/P ratio of 1/2 substantially enhanced conversion in both HDS and HDN to unprecedented levels. Thus, for the reaction of dibenzothiophene an HDS conversion of 100% was obtained, and for the reaction of quinoline an HDN conversion of 81% was observed. Even in the conversion of a real feed, this material showed better activity, selectivity, and stability than a commercial Co-Mo-S/Al_2O_3 (2). The objective of the present chapter is to examine the effect of Ni_2P loading on the surface properties, structure, and reactivity of Ni_2P/SiO_2 catalysts in order to identify an optimal Ni_2P loading for activity and stability.

4.2 Experimental

4.2.1 Synthesis and characterization of catalysts

The materials and gases employed in this chapter were the same as those in Chapter 2. Detailed preparation procedures have been described in Chapter 3 and only a synopsis need be presented here. Briefly, the synthesis of the catalysts involved two stages. First, intermediate precursors of nickel phosphate on silica were obtained by incipient wetness impregnation of aqueous phosphate solutions from metal nitrates and ammonium phosphate, followed by drying and calcination at 773 K. Second, the precursor materials were reduced to phosphides in H_2 flow by the method of temperature-programmed reduction (TPR) to 850 K, and were subsequently passivated in 0.5 % O_2/He at room temperature. The amounts of the reagents used and the weight of the precursors collected after calcination are listed in Table 4.1. In the study of these materials in the previous chapter, the metal loading was kept constant at a level corresponding to the 12.2 wt.% Ni_2P/SiO_2 sample used here. For this reason, this loading level will be referred to in this paper as a loading level of 1.0. Relative to this level, other loading levels are designated as 0.5, 1.5 and 2.0 (Table 4.1).

Table 4.1. Quantities used in the preparation of the samples

Loading level	Materials Used			Phosphide Loading (wt % MP_x)	Product after calcined/ g	x* experimental
	Silica /g	Nickel Nitrate /mol	$(NH_4)_2HPO_4$ /mol			
0.5	20	0.0115	0.0231	6.1	22.5	1.0
1.0	20	0.0231	0.0462	12.2	25.0	2.2
1.5	20	0.0387	0.0693	18.3	27.7	1.8
2.0	20	0.0462	0.0924	24.5	30.4	2.3

*: x in $Ni_2O_{0.5}(PO_4)$ + x H_3PO_4

The catalysts were characterized by CO chemisorption, BET surface area determinations, x-ray diffraction (XRD) and extended x-ray absorption fine structure (EXAFS) measurements. Irreversible CO uptake measurements were used to titrate the surface metal atoms and to provide an estimate of the active sites on the catalysts. They were obtained by pulsing calibrated volumes of CO into a He carrier and measuring the decrease in the peak size caused by adsorption. Uptakes were obtained after passivation and rereduction of samples, and are denoted as *ex situ* uptakes. BET surface area measurements were carried out right after the CO uptake determinations, also using a flow technique (1). The areas were calculated from the one-point BET equation, which is applicable for the non-microporous samples used here. X-ray diffraction (XRD) patterns of both the fresh and spent samples were determined with a Scintag XDS-2000 powder diffractometer operated at 45 kV and 40 mA, using Cu Kα monochromatized radiation (λ = 0.154178 nm). Crystallite sizes of the spent catalysts were determined from the line-broadening of the two most intense peaks at $2\theta = 40.8^{o}$ (h k l = 1 1 1) and at $2\theta = 44.6^{o}$ (h k l = 2 0 1). Use was made of the Scherrer equation, $D_c = K\lambda/\beta \cos(\theta)$, where K is a constant taken as 0.9, λ is the wavelength of the x-ray radiation, β is the width of the peak at half-maximum corrected for instrumental broadening (0.1^{o}), and 2θ is the Bragg angle (3).

In order to determine whether the structure of the catalysts changed with loading and with reaction, the catalysts were examined using EXAFS analysis. Nickel K-edge EXAFS spectra were obtained for both the fresh and spent samples. The spent samples were removed from the reactors, washed with hexane, dried and treated in He flow at 723 K. The prepared samples were transferred to glass cells with Kapton windows and sealed without exposure to the atmosphere. Comparisons were made with several reference materials, Ni_2P (Cerac, 99.5 %), NiO (Cerac, 99 %), NiS (Cerac, 99.9 %), $NiCO_3[Ni(OH)_2]\cdot 4H_2O$ (Aldrich). The measurements were made in a transmission mode at the BL12C beamline in the Photon Factory, High Energy Laboratory in Tsukuba, Japan, and at the X18B beamline in Brookhaven National Laboratory. Both were operated at close to 2.5 GeV with a 400 mA ring current. The monochromator in Tsukuba was equipped with a channel cut Si (311) crystal and gave an energy resolution of about 1 eV, while that in Brookhaven used a Si (111) crystal and resulted in an energy resolution of 2 eV.

FEFF simulations to obtain phase shifts and amplitude functions of Ni_2P and $Ni_{12}P_5$ were done with FEFF 8.0 code (4). The FEFF input file for the simulation consisted of the cluster size (0.6 nm), atomic positions, and type of atoms obtained from crystallographic data from the literature (5,6).

4.2.2 Reactivity studies

Hydrotreating activities of the samples were tested in a three-phase trickle bed reactor operated at 3.1 MPa and 643 K for hydrodenitrogenation (HDN), hydrodesulfurization (HDS), hydrodeoxygenation (HDO), and hydrodearomatization (HDA) of a model feedstock containing 2000 ppm nitrogen (quinoline), 3000 ppm sulfur (dibenzothiophene), 500 ppm oxygen (benzofuran), 20 wt.% aromatics (tetralin) and balance aliphatics (tetradecane). The HDS conversion refers to the transformation of dibenzothiophene to biphenyl, the HDN conversion to the reaction of quinoline to denitrogenated products, the HDA conversion to the reaction of quinoline to N-containing hydrogenated products (1,2,3,4-tetrahydroquinoline, 5,6,7,8-tetrahydroquinoline, orthopropylaniline), and HDO conversion to the reaction of benzofuran to ethylbenzene.

The schematic of the testing system was shown elsewhere (7). Briefly, the testing unit consisted of three parallel reactors immersed in a fluidized sand bath (Techne, Model SBL-2) whose temperature was controlled by a temperature controller (Omega, Model 6015 K). The reactors were 19mm/16mm o.d/i.d. 316 SS tubes with central thermocouples monitoring the temperature of the catalyst beds. The catalysts were in the form of pellets (16/20 mesh) and were supported between quartz wool plugs in 13 mm i.d. 316 stainless steel baskets. The hydrogen flow rate was set to 100 μmol s^{-1} (150 cm^{-3} min^{-1}, NTP) with mass flow controllers (Brooks, Model 5850E), and the feed liquid flow rate (5 cm^{-3} h^{-1}) was metered from burettes by high pressure liquid pumps (LDC Analytical, Model NCI 11D5). Quantities of catalysts loaded in the reactors corresponded to the same amount of *ex situ* CO uptake (70 μmol). Prior to reactivity measurements the catalysts were pretreated at 723 K for 2 h before the feed liquid was introduced into the reactors. Hydrotreating samples were collected every two or three hours in sealed septum vials, and were analyzed off-line with a gas chromatograph (Hewlett Packard, 5890A) equipped with a 0.32 mm i.d. x 50 m fused silica capillary column (CPSIL-5CB, Chrompack, Inc.) and a flame ionization detector.

4.3 Results and discussion

The preparation of the supported phosphides was carried out in two stages. First, supported phosphates were obtained by impregnation of a solution of the metal and phosphorus components onto a carrier silica support, followed by drying and calcination. Second, the phosphates were transformed into phosphides by temperature programmed

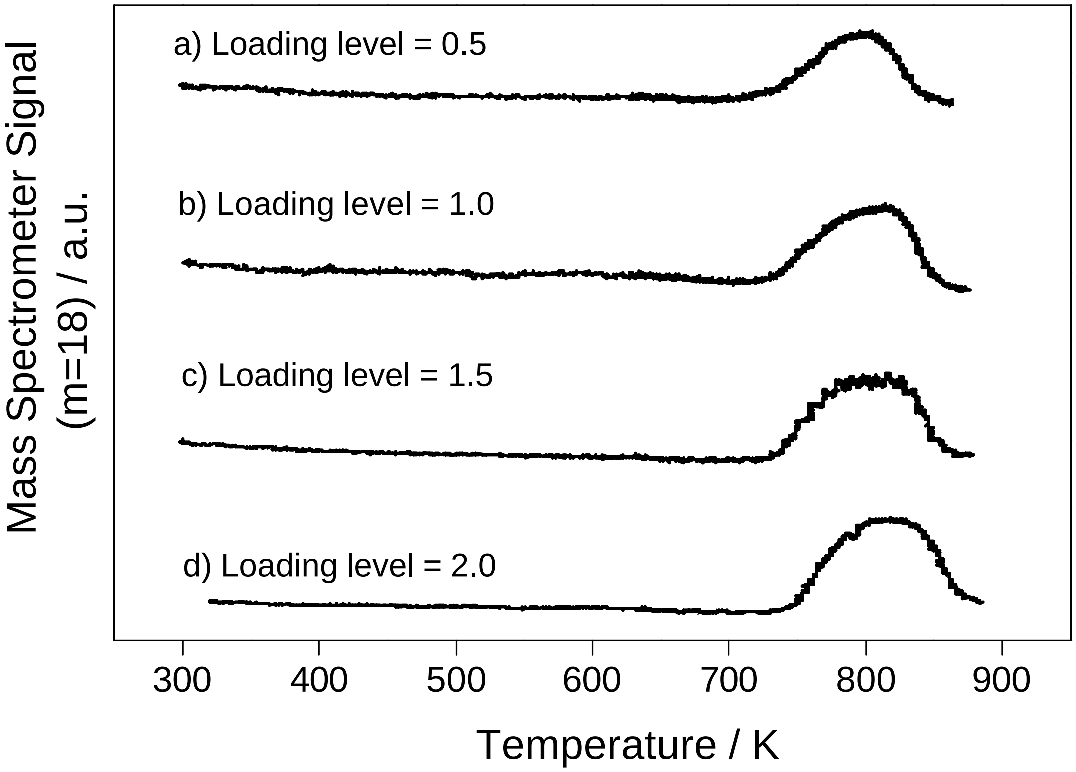

Figure 4.1. Mass 18 signal from temperature-programmed reduction of the samples at β= 1K/min (0.01667 K s^{-1})

reduction (TPR). There was some loss of phosphorous during the calcination stage, as evidenced by the observation of a solid deposit on the lid of the calcination vessel. This was likely to be P_2O_5 whose sublimation point (673 K) was lower than the calcination temperature (773 K). The amount of product collected after calcination (Table 4.1) can be used to estimate this loss. Assuming that after calcination the product is a mixture of nickel oxyphosphate ($Ni_2O_{0.5}PO_4$) and phosphate (as H_3PO_4), the theoretical moles of phosphate would be x = 3 (since total Ni/P = 1/2). The calculated amount ranged from x =

1.0 for the low loading sample to x = 2 for the higher loading samples, confirming that there was some loss of phosphorous.

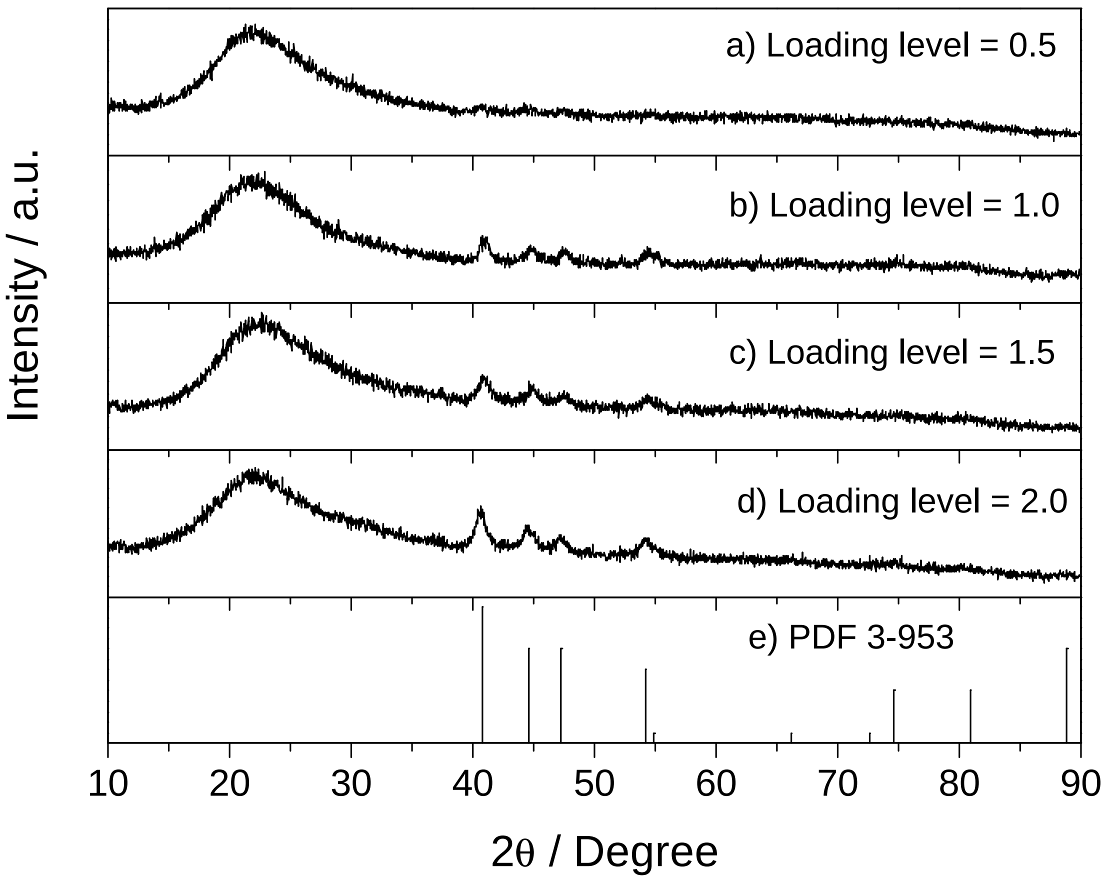

Figure 4.2. X-ray diffraction patterns of the fresh samples (α: Ni_2P; β: $Ni_{12}P_5$ or Nickel sulfide)

Figure 4.1 shows the water evolution during the temperature programmed reduction stage of the synthesis. Mass 34 (PH_3) followed the same trend as the water signal, and is not displayed. Evidently there is some loss of phosphorous during reduction as well as calcination. Other masses gave no additional information. It is clearly seen that the reduction reactions for all the samples essentially occurred in the same temperature range, except that a slightly higher temperature was required for the higher loading samples (Fig. 4.1c-d). This is understandable since larger phosphate particles are probably present on the higher loading samples, which present larger pathways for diffusion in the solid-state reduction process.

X-ray diffraction patterns of the fresh samples are presented in Figure 4.2. The patterns all show a broad feature at $2\theta \sim 22^o$ due to the amorphous silica support. At higher angles, peaks due to Ni_2P are visible at all loadings. The phase corresponds to hexagonal Ni_2P (8) which adopts the Fe_2P structure with a space group of $P_{\bar{6}2m}$. The pattern is represented in the powder diffraction file PDF 3-953 (Fig. 4.2e) (9).

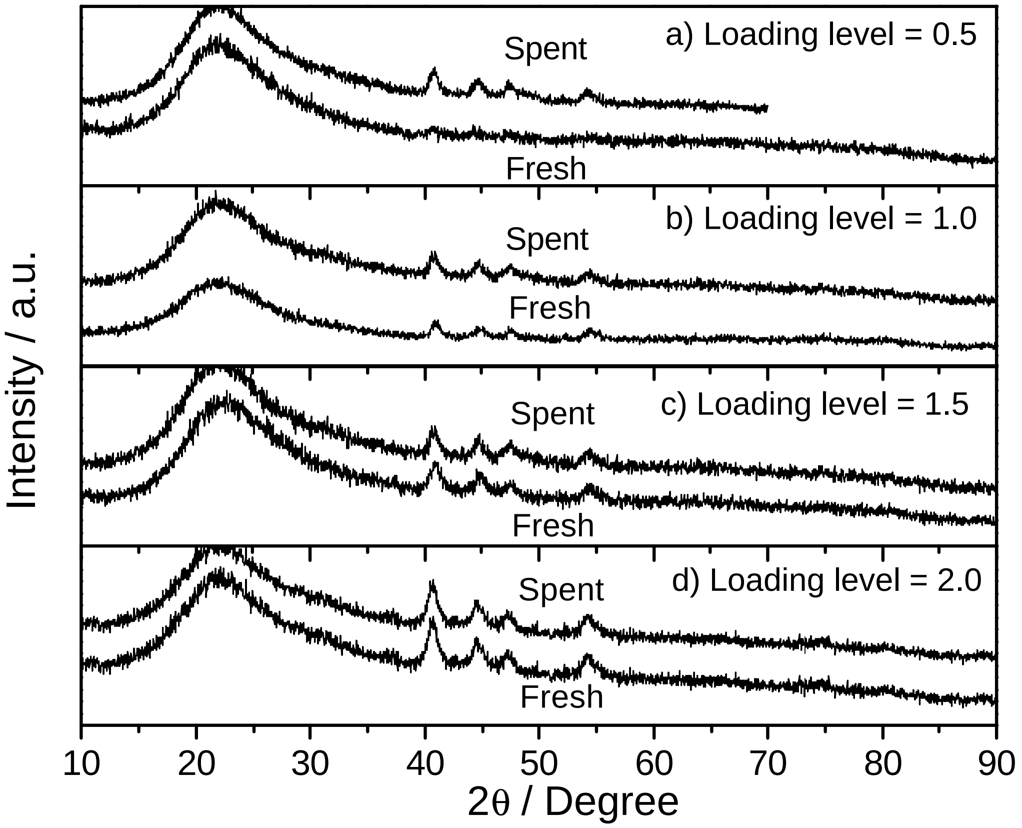

Figure 4.3. Comparison of X-ray diffraction patterns for the fresh samples and the spent samples

X-ray diffraction patterns were also obtained for the spent samples (Fig. 4.3). The figure shows that there is no change in the pattern for all the samples, demonstrating that the Ni_2P was relatively stable at the hydrotreating conditions. The intensity of the XRD peaks for the spent samples increased, which indicates that the samples became more crystallized after the hydrotreating reaction. The crystallization was likely a consequence of the prolonged exposure (> 90 h) of the samples to the hydrotreating temperature of 643 K.

Table 4.2. Characterization results of samples

Loading level[#]	Samples	BET Surface area S_g m^{2}g^{-1}	CO uptake μmolg^{-1}	Metal site density (L) μmolg^{-1}	Dc nm
0.5	Fresh	74	23	85	-
	Spent	88	7	85	7.7
1.0	Fresh	97	28	170	-
	Spent	89	24	170	8.7
1.5	Fresh	102	40	254	-
	Spent	98	45	254	9.2
2.0	Fresh	72	37	339	-
	Spent	83	27	339	9.8

[#]: the loading level of 1.0 corresponds to 12.2 wt.% Ni_2P/SiO_2

X-ray line broadening analysis of the spent samples indicates a weak trend toward larger crystallite sizes with increasing sample loading. The crystallite sizes are listed in the last column of Table 4.2 and are seen to increase from 7.7 to 9.8 nm. The surface properties of the fresh catalysts are also shown in Table 4.2. The BET specific surface areas (S_g) and CO chemisorption uptakes of the samples are listed in columns 3 and 4 of the table, respectively. The S_g values of the samples were of the order of that of the silica support (90 m^2g^{-1}) with deviations due to experimental error with the flow technique. The CO chemisorption uptake increased with increase of the Ni_2P loading, reaching a maximum value of 40 μmol g^{-1}, and then decreased. The results indicate that there is probably crystallite agglomeration on the higher loading samples, resulting in a slightly poorer dispersion of Ni_2P, and hence giving lower CO chemisorption. Metal site concentrations were obtained from the crystallite size (D_c) and the known density of metal atoms ($\bar{n}$ = 1.01 x 10^{15} atoms cm^{-2}) from the crystal structure (1). The metal site concentration was calculated from the equation, $(L) = S\bar{n}f$, where f is the fractional weight loading of the sample (Table 4.1), and $\bar{n}$ is the average surface metal atom density, S is the theoretical surface area obtained from the equation, $S = 6/\rho D_c$. The results are listed in the fifth column of Table 4.2, and are seen to increase with increasing loading amount. The number of metal sites is much higher than the sites titrated by CO uptake. This could be due in part to the agglomeration of the crystallites mentioned above. As can be seen, there is a greater difference in the two values at higher loadings, consistent with this interpretation. However, the differences are too large to be explained by just agglomeration, and it is likely that CO chemisorption sites are blocked by surface phosphorus. As described in the synthesis section, the samples here were prepared with an excess of phosphorus over stoichiometric (Ni/P = 1/2) because a previous study (Chap. 3) showed that such a composition was necessary for obtaining stable Ni_2P crystallites of high activity.

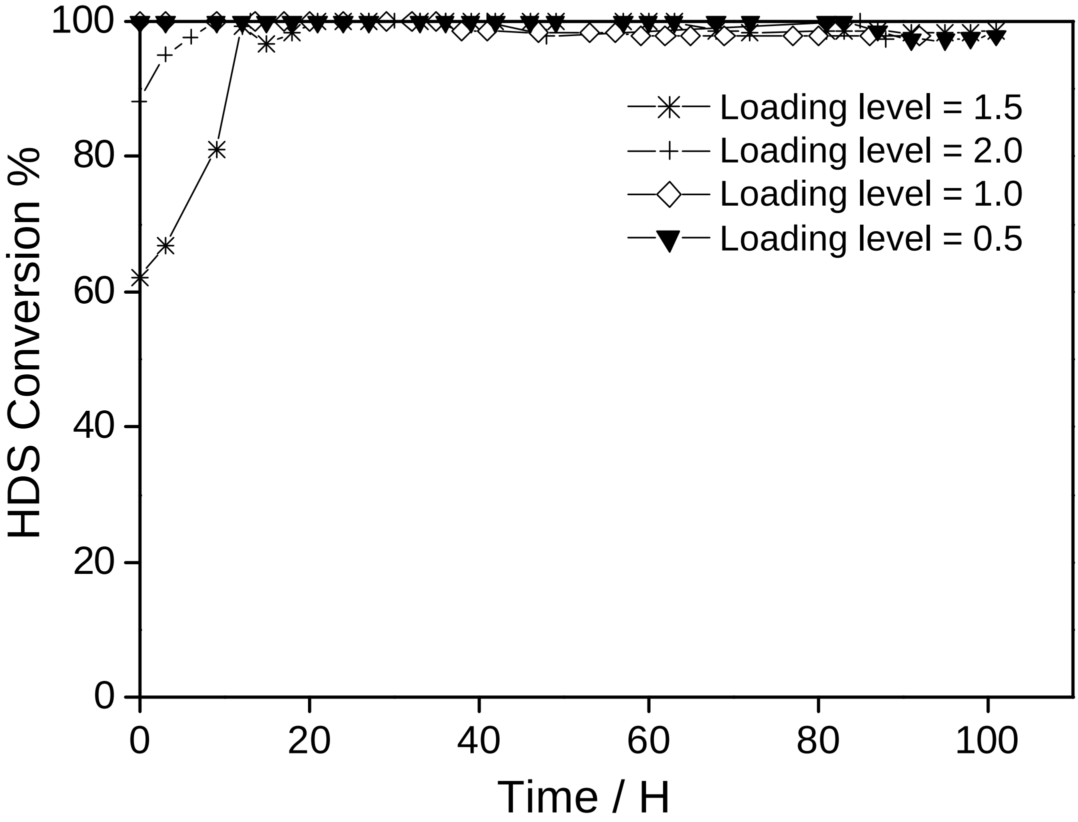

Figure 4.4. Hydrodesulfurization performance of supported catalysts

Figures 4.4-5 present the time course of HDS and HDN activities for the various catalysts, reported as the dibenzothiophene and quinoline conversions, respectively. The HDS activity was uniformly high for all the samples with an HDS conversion at 97 - 99 % (Fig. 4.4). In contrast, the HDN activity varied considerably with Ni_2P loading. The samples with intermediate loading levels of 1.0 and 1.5 followed similar time courses, with the sample of level 1.5 showing good stability. The final HDN conversions for these samples were 81 % and 91 %, respectively (Fig. 4.5). The sample with the highest and lowest loading levels deactivated quickly and reached a low HDN activity below 40 %. A summary of all the results is presented in Figure 4.6, which shows the effect of loading on the activity of all the catalysts. The best performance was obtained at a loading level of 1.5 with an HDS conversion of 99 % and an HDN conversion of 91 %.

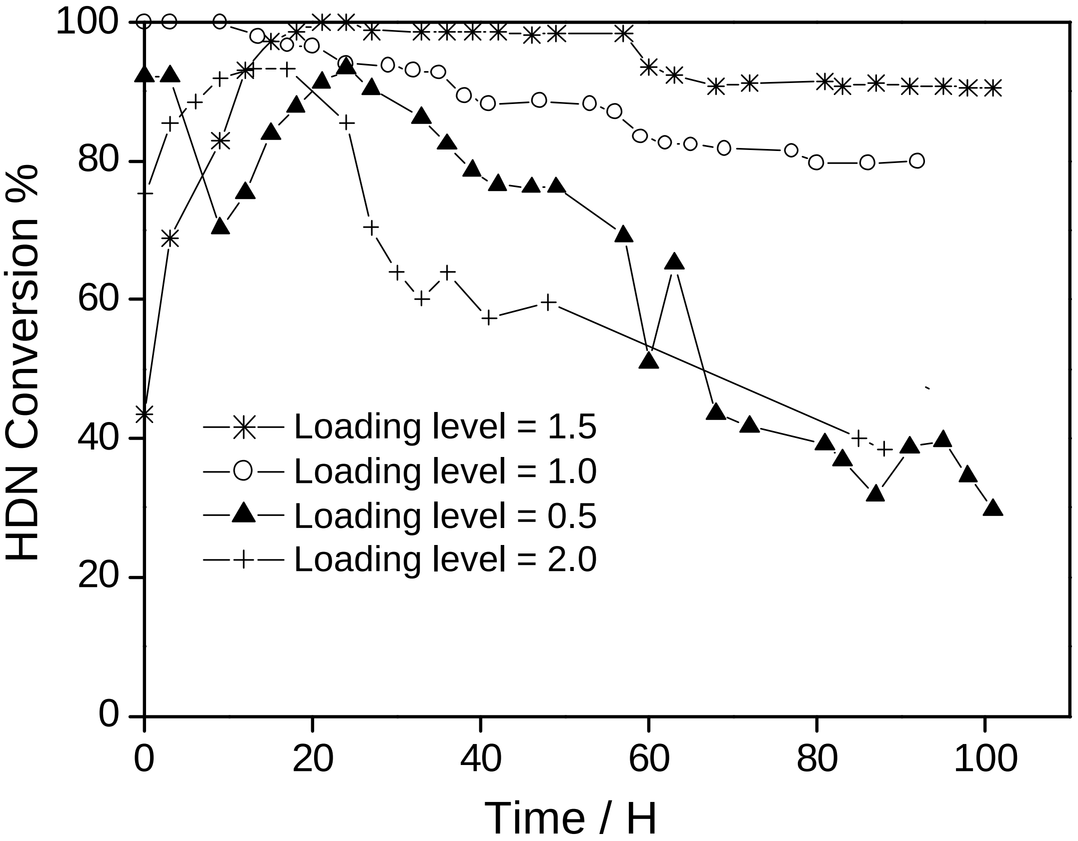

Figure 4.5. Hydrodenitrogenation performance of supported catalysts

Compared to a commercial Ni-Mo-S/Al_2O_3 catalyst which gives an HDS conversion of 76 % and an HDN conversion of 38 %, the Ni_2P/SiO_2 with loading level 1.5 is substantially more active. The comparison here was based on 70 μmol of sites loaded in the reactor, the sites counted by CO chemisorption for the phosphides and O_2

chemisorption for the sulfide. Thus, the comparison shows the intrinsic activity of the phosphide is very high.

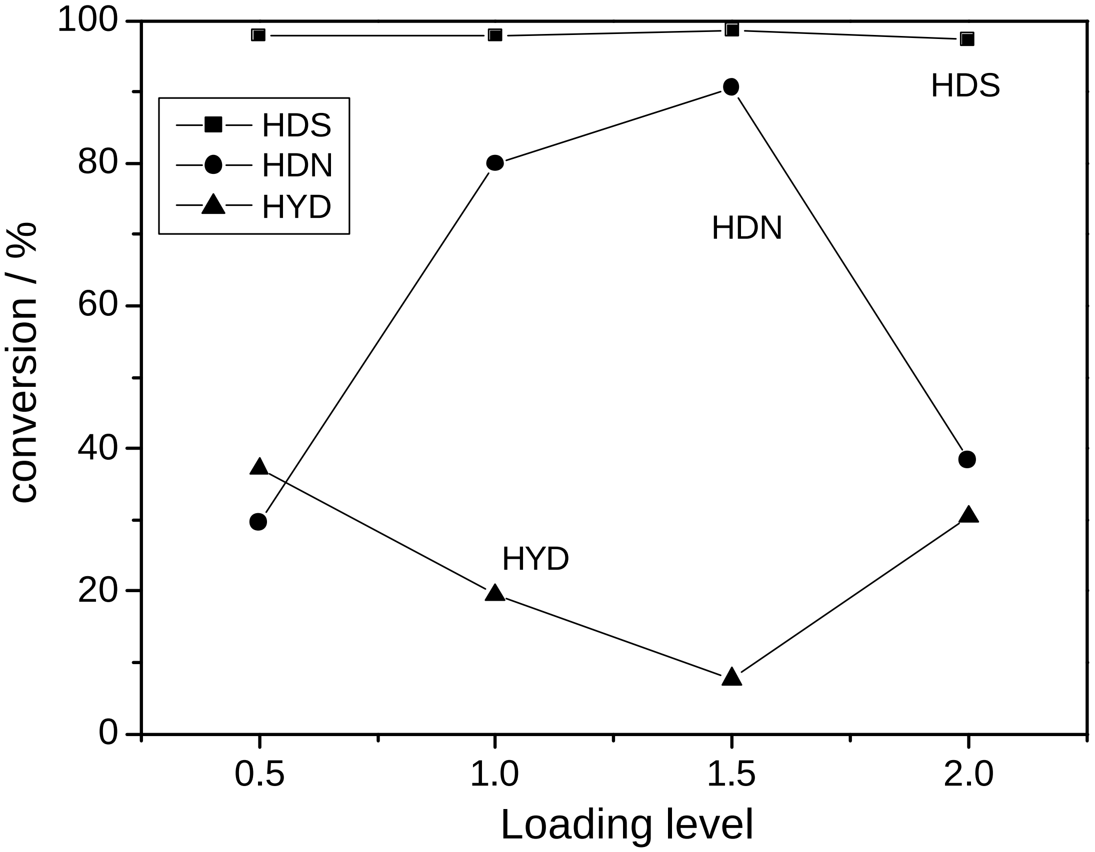

Figure 4.6. Comparison of hydroprocessing activities

Table 4.3. Product Distribution in Hydroprocessing

Reactants	Conversion / %					Selectivity / %				
	Loading level	0.5	1.0	1.5	2.0	Product	0.5	1.0	1.5	2.0
Dibenzo thiophene	HDS	98	98	99	97	biphenyl	100	100	100	100
Quinoline	HDN	30	81	91	38	Propyl cyclohexane	8.9	50	53	4.7
						propylbenzene	17	28	38	22
	HYD	37	19	7.7	31	5,6,7,8-tetrahydro quinoline	27	3.9	2.0	22
						orthopropyl aniline	37	15	4.8	33
						1,2,3,4-tetrahydro quinoline	11	3.7	1.8	18
Benzofuran	HDO	37	46	100	50	ethylbenzene	100	100	100	100
Tetralin	De HYD	44	23	36	55	naphthalene	98.8	94.9	96.6	99.0
	HYD	0.5	1.2	1.2	0.6	trans-decalin	0.5	2.7	2.2	0.3
						cis-decalin	0.7	2.4	1.2	0.7

Catalyst loading based on 70 μmol CO uptake

A full report of the activity and selectivity of the catalysts is presented in Table 4.3. The reaction of dibenzothiophene occurs with very high conversion (97 – 99%) on all catalysts and gives total selectivity to biphenyl. The conversion of quinoline is low at the smallest and largest loading level but is high (81 – 91 %) at intermediate loading levels. The products can be classified as hydrogenated molecules (5,6,7,8-tetrahydroquinoline, orthopropylaniline, 1,2,3,4-tetrahydroquinoline) and denitrogenated species (propylcyclohexane, propylbenzene). At high HDN conversions propylcyclohexane is favored because of the likely need to hydrogenate the two aromatic rings prior to nitrogen removal. Benzofuran is completely deoxygenated to ethylbenzene on all catalysts, notably with 100 % conversion for the catalyst with intermediate loading level of 1.5. For thermodynamic reasons, at the conditions of reaction tetralin is mostly dehydrogenated to naphthalene. Small amounts of cis- and trans-decalin are formed.

The CO uptakes for the spent samples are listed in Table 4.2. The values decreased for all samples except for the active sample with loading ratio of 1.5. The decrease was particularly pronounced for the catalysts with the lowest and highest loadings. This loss of active centers may be an important reason for the deactivation of the catalysts (Figure 4.5).

Figure 4.7 presents the HDN and HDS turnover rates (TORs) based on CO uptakes before reaction and the CO chemisorption values themselves for both the fresh and spent samples as a function of loading level. The CO uptakes of the fresh samples increase with loading, but not as much as expected from the crystallite size and concentration. As discussed previously this indicates some crystallite agglomeration on the higher loading samples, especially in the sample with the loading level of 2.0. The hydroprocessing TORs results indicate that HDS reactions are not affected by the surface properties of the catalysts, while the HDN reactions are very sensitive to the structure or composition of the catalyst surface. In a previous study of the mechanism of HDN on MoP and WP (10) it was established that denitrogenation occurred through an E2 elimination involving dual acid and nucleophilic centers on the surfaces. The need for such surface centers also in the case of Ni_2P would make the reaction sensitive to the exact arrangement of Ni, P and possibly S atoms on the surface, and would explain the strong effect of loading on HDN.

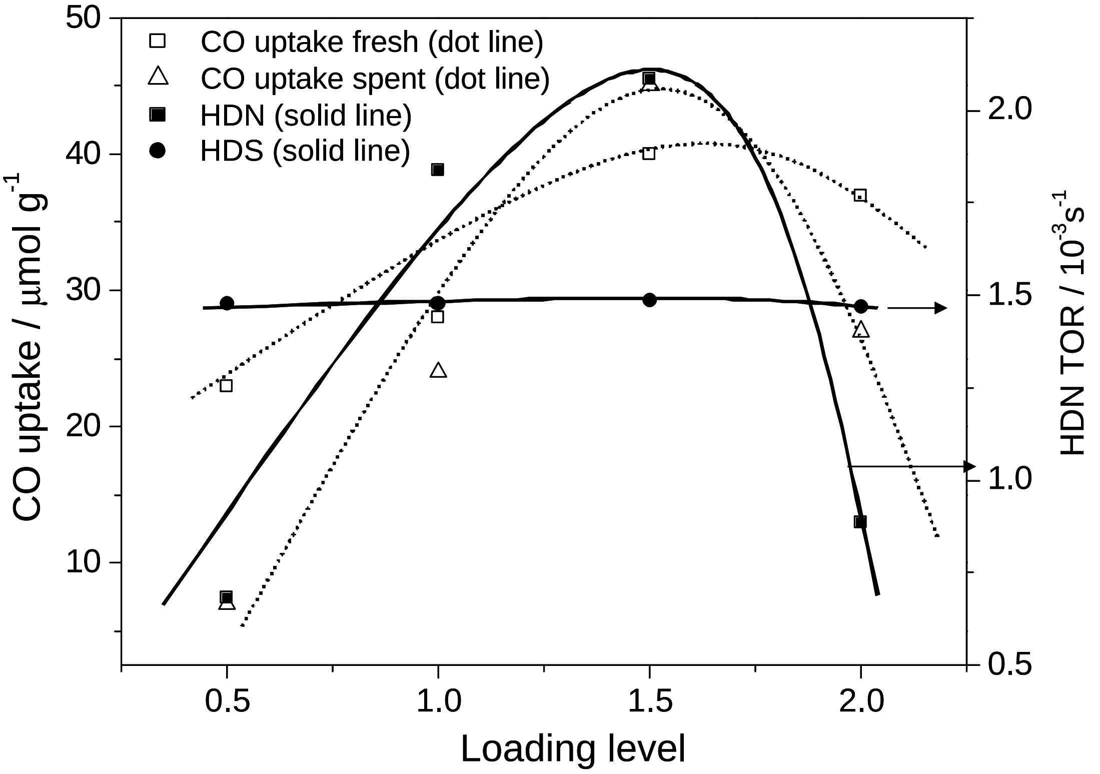

Figure 4.7. Curves of HDN and HDS turnover rates and CO uptakes

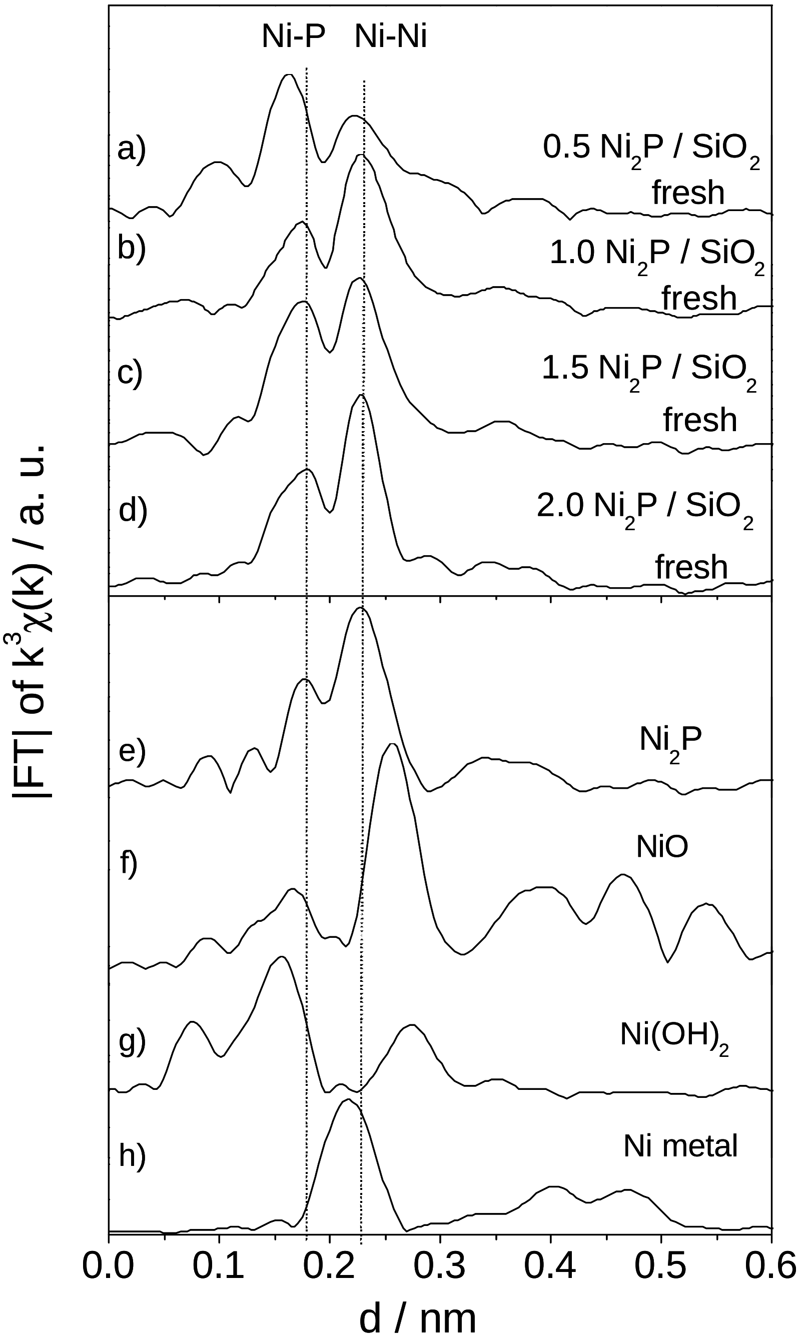

Figure 4.8. Comparison of Nickel K edge EXAFS for the fresh samples with loading ratio as 0.5, 1.0, 1.5, 2.0, and Ni_2P, NiO, $Ni(OH)_2$ and nickel metal.

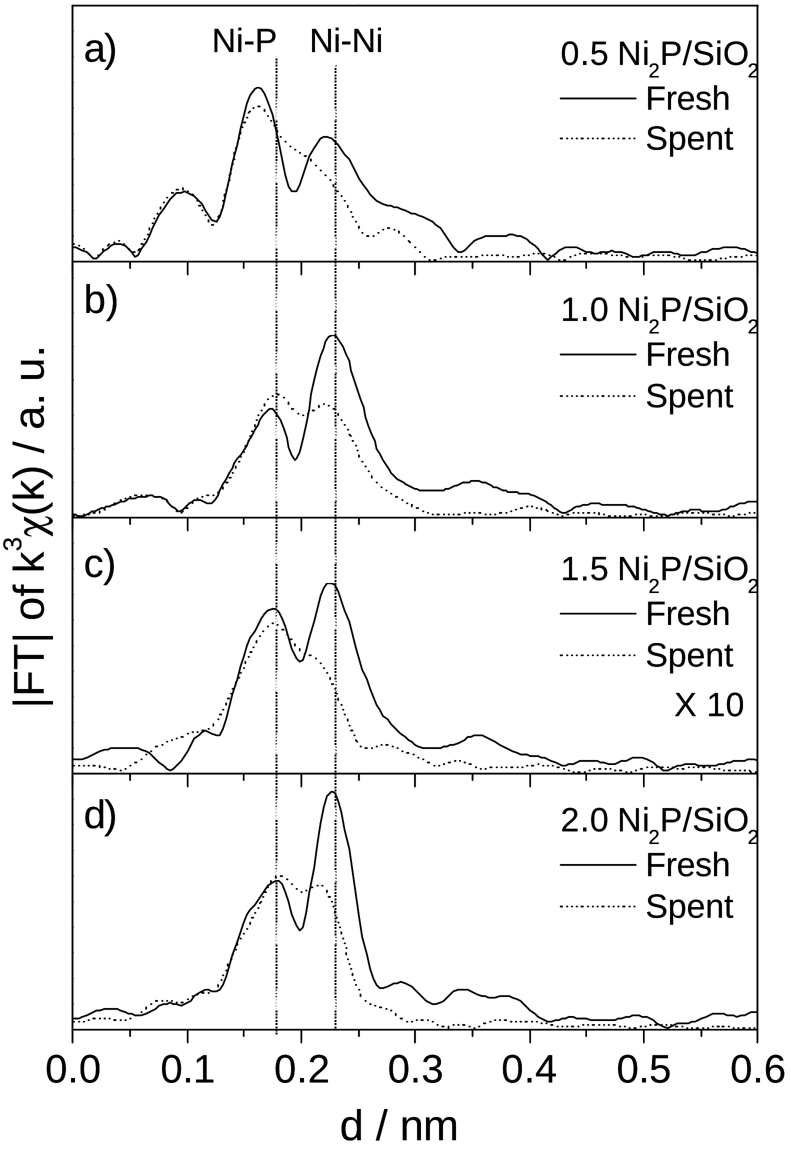

Figure 4.9. Nickel K edge EXAFS of the fresh and spent samples with different loading (12.23 wt.% here was used as loading 1.0), a) o.5; b) 1.0; c) 1.5; d) 2.0

Ni K-edge EXAFS spectra for the fresh samples with loading levels of 0.5, 1.0, 1.5 and 2.0 were compared with those of bulk Ni_2P, NiO, $Ni(OH)_2$ and Ni metal (Fig. 4.8). The Fourier Transforms (FT) for the supported Ni_2P samples are characterized by two prominent peaks in the bonding region (> 0.13 nm) (Fig. 4.8a-d). For the higher loading levels of 1.0 and above (Fig. 4.8b-d), the position of the peaks correspond to the Ni-P and Ni-Ni distances in bulk Ni_2P (Fig. 4.8e). The relative intensity of the peaks also are close to those of bulk Ni_2P, although the sample with the highest loading level 2.0 shows enhanced intensity (Fig. 4.8d) at the Ni-Ni peak.

For the lowest loading level of 0.5 (Fig. 4.8a), the FT peaks shifted to lower distances from those of Ni_2P. The Ni-Ni distance was displaced toward that of metallic Ni (Fig. 4.8h), whereas the shorter distance peak was displaced toward that of a Ni-O bond in NiO (Fig.8f) or $Ni(OH)_2$ (Fig. 4.8g). It appears that incomplete phosphidation occurred in this sample, and that as the material was reduced some Ni-Ni and Ni-O bonding contributions were formed. This is consistent with the XRD patterns, which gave very weak signals for Ni_2P for this sample, and the calculations for P_2O_5 volatilization (Table 4.1), which showed least retention of phosphorous.

Ni K-edge EXAFS results for both the fresh and spent samples are compared in Figure 4.9. The features of the fresh samples (solid lines) and the spent samples (dashed lines) were different, especially in the Ni-Ni peak region. The intensity of the Ni-Ni peak decreased after hydrotreating for all the samples, and it is likely that some other nickel compounds were formed as a consequence of the reaction.

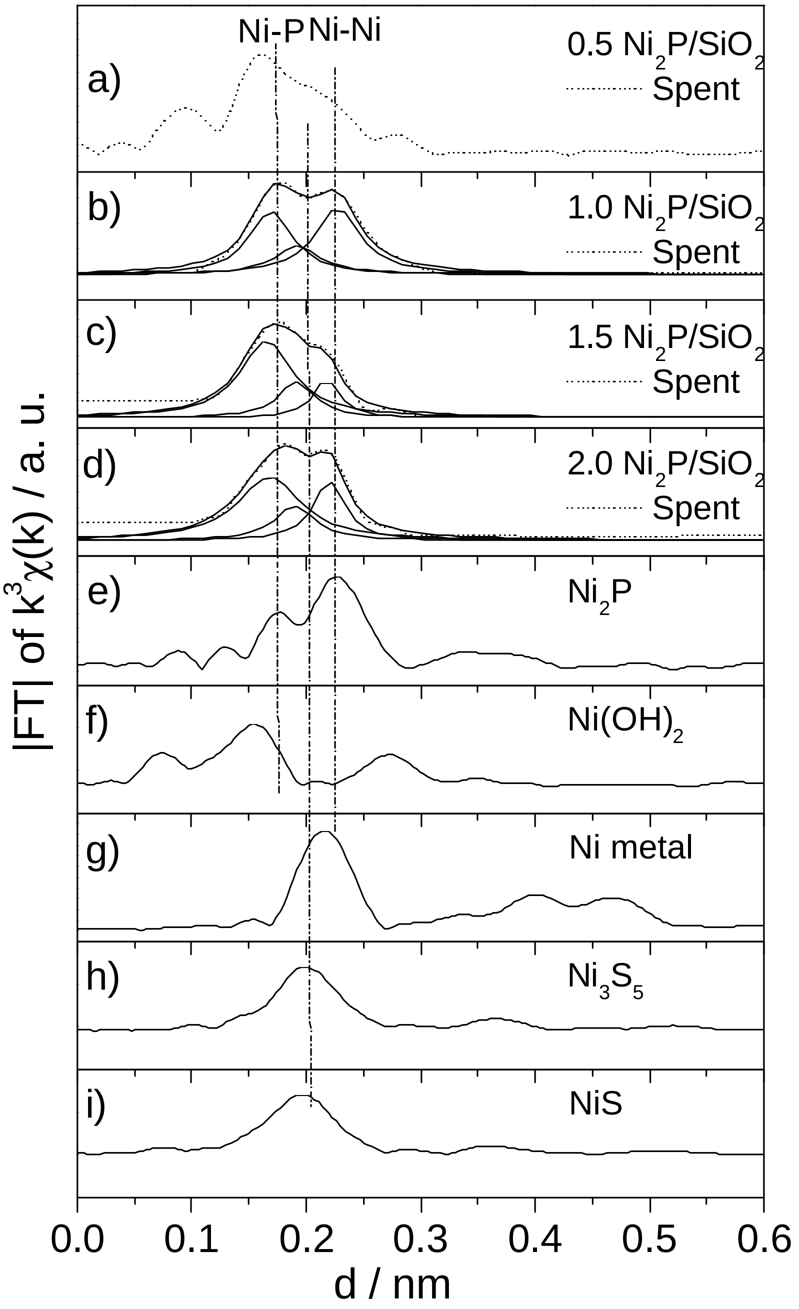

Figure 4.10. Comparison of Nickel K edge EXAFS for the spent samples with loading ratio as 2.0, 1.5, 1.0, 0.5 and Ni_2P, $Ni(OH)_2$, nickel metal, Ni_3S_5, and NiS

The EXAFS results of the spent samples (Fig. 4.10 a-d) were compared with some reference compounds (Fig. 4.10e-i) to identify the newly formed phase. The diminution in the intensity of the Ni-Ni peak in Ni_2P for the samples (Fig. 4.10a-d) seemed to be accompanied with a shift to lower distance. The Ni-P peak itself remained strong, though slightly diminished in distance. The result could be due to the formation of some phosphorous deficient Ni phase, but also could be due to development of intensity in the Ni-S distance region. Even though no distinct Ni-S peak is seen, a feature in that region would give rise to the broad signal actually observed. Fig. 4.10c-d shows just such a fit to three Lorentzian line shapes for the higher loading samples.

In order to check the possibility of formation of a phosphorus-deficient phase, calculation of the EXAFS of $Ni_{12}P_5$ were carried out. In a previous study of Ni_2P/SiO_2 of different Ni/P ratios an XRD peak that could be due to $Ni_{12}P_5$ was observed for a spent sample with Ni/P = 1/1. First, the applicability of FEFF calculations was checked with Ni_2P. The FEFF simulation of Ni_2P produced a similar EXAFS oscillation compared to the experimental result of Ni_2P (Fig. 4.11a). In the higher k-region (> 80 nm^{-1}), the amplitude of the calculated oscillation was stronger than that of the experimental spectrum. However, the periods of both EXAFS oscillations were quite similar. A comparison of the Fourier transforms of bulk Ni_2P and the FEFF simulation also showed good agreement (Fig. 4.11b). The first and second nearest neighbors corresponding to Ni-P, and Ni-Ni bonds in bulk Ni_2P were identical to those obtained in the FEFF simulation (Table 4.4). Moreover, the third and fourth shells of the Fourier transforms also showed good agreement. This indicates that the FEFF simulation is able to account for the essential elements of the bulk Ni_2P structure.

Table 4.4. Summary of structural parameters used in FEFF simulation

	Ni_2P			$Ni_{12}P_5$	
Bonding	Coordination number	Distance / nm	Bonding	Coordination number	Distance / nm
Ni-P	**2**[a]	**0.22090**[a]	Ni-P	**1**[d]	**0.22294**[d]
	2[b]	**0.22662**[b]		**1**[e]	**0.22504**[e]
	2	0.37042		1	0.24245
	4	0.40393		1	0.24625
Ni-Ni	2	0.26050	Ni-Ni	1	0.25249
	2	0.26131		1	0.25451
	4[c]	**0.26783**[c]		1	0.25472
	2	0.33820		1	0.25720
	4	0.38260		1	0.25955
	4	0.42739		**2**[f]	**0.26347**[f]
	4	0.43339		1	0.27031
				2	0.36280
				2	0.36492
				2	0.36632
				4	0.48636

*a-f : the major contribution in the simulation.

The synthesis of $Ni_{12}P_5$ as a reference material was attempted by the ampoule technique (heating stoichiometric amounts of Ni metal and phosphorous powder in a sealed quartz ampoule at 1073 K for 100 h), but was unsuccessful. Therefore, resort was made to a FEFF simulation. The results are shown in Fig. 4.11c,d. The simulation clearly shows that slightly reduced Ni-Ni and Ni-P distances compared to Ni_2P are to be expected for $Ni_{12}P_5$. This is an indication of the possible contribution of this phase to the spectra. However, the results are not unequivocal. They do not explain the retention of a strong Ni-P EXAFS signal and the Ni_2P XRD pattern, both of which should be diminished with reduced P amounts. What the data strongly suggest though is that Ni-Ni bonds are disrupted in favor of the formation of some Ni-S linkages. Thus, the active catalyst in these materials is probably a Ni-P-S surface phase. The presence of three elements in different arrangement causes the activity of the catalysts in the HDN and HDS reactions to be affected differently.

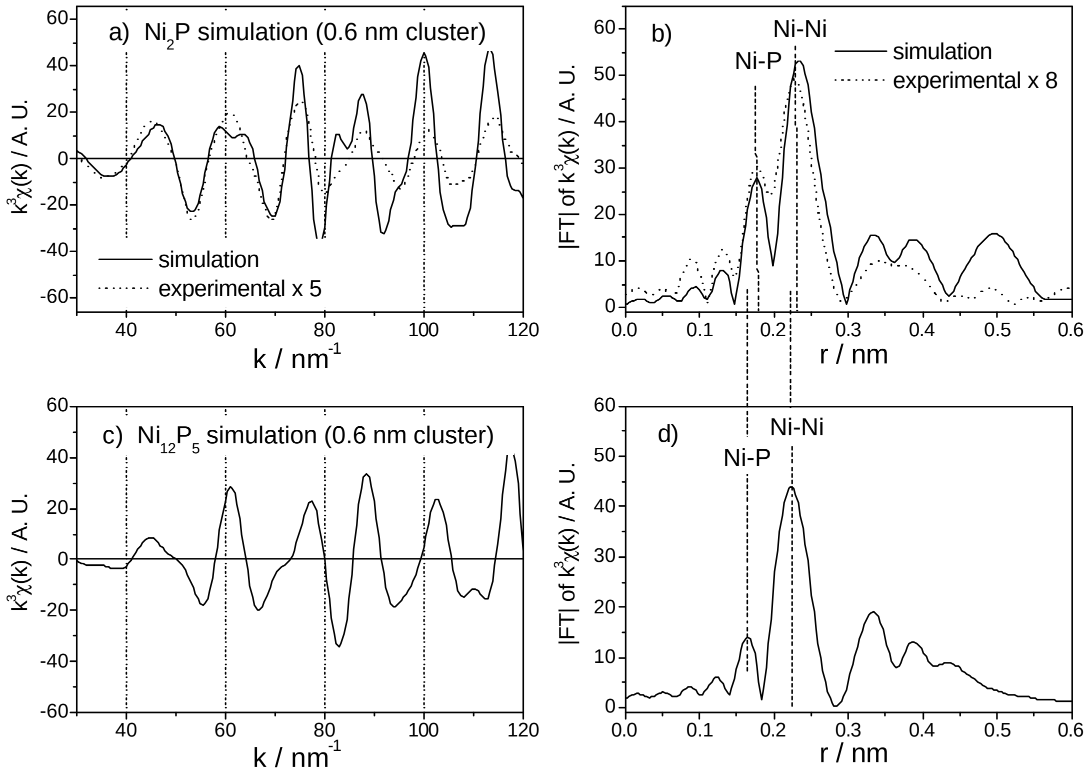

Figure 4.11. FEFF simulations for Ni_2P and $Ni_{12}P_5$.

Based on the influence of surface properties on the activity, Boudart categorized reactions as ‘structure-sensitive’ and ‘structure-insensitive’ (11,12). This proves to be a valuable concept for these new catalysts. The results shown in this chapter and in the previous chapter are consistent with the HDN reaction of quinoline being structure-sensitive, and the HDS reaction of dibenzothiophene being structure-insensitive.

4.4 Conclusions

The effect of loading on the structure and hydroprocessing behavior of Ni_2P/SiO_2 was investigated. The loading amount of Ni_2P on silica was optimized with the best reactivity results obtained at a Ni_2P loading of 18 % to give an HDS conversion of 99 %, and an HDN conversion of 91 %. These were much higher than those of a commercial catalyst which gave an HDS conversion of 76 % and an HDN conversion of 38 %. XRD and EXAFS showed the formation of Ni_2P phase on all the fresh samples. The spent samples experienced phase changes. The surface properties obtained from the BET surface area and CO uptake measurements indicated the occurrence of crystallite agglomeration on the higher loading samples. The loading effect and Ni/P composition effect on the reactivities of the catalysts indicated again that the HDN reaction of quinoline is structure sensitive, while the HDS reaction of dibenzothiophene is structure insensitive.

References

---

1. Wang, X., Oyama, S. T., Requejo, F., *J. Catal.*, submitted.

2. Oyama, S. T., Wang, X., Requejo, F., Sato, T., Yoshimura, Y., J. Catal. In press.

3. Cullity, B.D., “Elements of X-Ray Diffraction”, 2nd Ed., p. 102, Addison-Wesley Publishing Company, Menlo Park, California, 1978.

4. Ankudinov, A.,L., Ravel, B., Rehr, J., J., Congradson, S., D., Phys. Rev. B 58, 7565 (1998)

5. Larson, E., *Arkiv. Kemi.*, **23**, 335(1965).

6. Larson, E., *Arkiv. Kemi.*, **23**, 345(1965).

---

7. Ramanathan, S., Oyama, S. T., New catalysts for Hydroprocessing: Transition Metal Carbides and Nitrides, J. Phys. Chem., Vol.99, No.44, 1995, 16365-16372
8. Rundqvist, S., *Acta Chem. Scand.* **16**, 992 (1962).
9. Powder Diffraction Data Files, JCPDS International Center for Diffraction Data, Swathmore, PA, 1992.
10. Clark, P., Wang, X., Oyama, S. T., Pentylamine mechanism study.
11. Boudart, M.; Djega-Mariadasson, G, “Kinetics of Heterogeneous Catalytic Reactions”. USA. (1984), 222 pp., Princeton University Press, Princeton, N. J.
12. Thomas, J. M.; Thomas, J. W.; Editors, “Principles and Practice of Heterogeneous Catalysis”. Germany. (1996), 553 pp. VCH, Weinheim, Germany

Chapter 5

Mechanism of Hydrodenitrogenation on Supported Nickel Phosphide (Ni_2P/SiO_2)

5.1 Introduction

Stricter environmental laws (1,2) and a decreasing quality of available petroleum feedstocks are placing high demands on hydrotreating technology, a set of processes used to remove pollutants, such as S, N, O and metals in refinery streams (3). This has led to intensive research in the development of improved catalysts with enhanced activity for hydrodesulfurization (HDS) and hydrodenitrogenation (HDN). Recently, a new catalyst, nickel phosphide Ni_2P, has been reported (4,5,6) with outstanding performance in simultaneous HDN and HDS. The purpose of this work is to investigate the mechanism of HDN on Ni_2P supported on silica. This topic is important because nitrogen compounds inhibit HDS (7) strongly and so their removal is key for obtaining ultra-low sulfur products.

Hydrodenitrogenation (HDN) of compounds in oil fractions is more difficult than hydrodesulfurization, requiring more severe conditions and greater hydrogen consumption (8). In most cases the prefered pathway for the HDN of heterocyclic molecules involves hydrogenation of aromatic rings associated with nitrogen atoms because it is easier to break C(sp^3)-N bonds than C(sp^2)-N bonds. Thus, quinoline undergoes complete hydrogenation of its heterocyclic and benzenic rings before removal of nitrogen (9,10,11), indole is hydrogenated to octahydroindoline (12) and pyridine is hydrogenated to piperidine (13,14,15). For this reason saturated compounds such as piperidine and its derivatives have been the subject of considerable study (16). The work is described in a comprehensive discussion of the mechanism of piperidine HDN by Hadjiloizou, et al. (17), an in-depth review of catalytic denitrogenation by Perot (18), and a more recent insightful monograph by Prins (19). In many cases for sulfides (20), carbides (21), and nitrides (22,21), the C-N bond cleavage proceeds by a β-elimination mechanism catalyzed by a Brønsted acid - Lewis base sites (23,24). Although there is some uncertainty about the rate-limiting step (20,21,25), there is agreement that HDN involves a multi-functional mechanism with hydrogenation and C-N cleavage carried out on different active sites (26,27,28,29) depending on the structure of the nitrogen containing heterocyclic compound, the reaction conditions, and the type of catalyst.

In this work, the mechanism on Ni_2P/SiO_2 was studied using piperidine and several of its derivatives to determine the effect of amine structure on reactivity, and hence, reaction pathway. Piperidine, $C_5H_{10}N$, is a saturated cyclic secondary amine obtained by the hydrogenation of pyridine. The HDN of piperidine involves the cleavage of two C-N bonds and its conversion is representative of the reaction of other cyclic nitrogen compounds. The work is important because there are many pyridine derivatives in petroleum and their HDN pathway involves hydrogenation to piperidine intermediates. It was found that the result could be explained by either a dual mechanism involving S_N2 and E2 pathways or by a single mechanism involving activation of the carbon atoms in α and β positions relative to the N atom in the ring. This work also employed a simpler amine, ethylamine, as a reactant and spectroscopic probe of the reaction pathways. Infrared studies allowed the determination of the structure of the reaction intermediate and the possible mechanisms of reaction.

5.2 Experimental

5.2.1 Materials

The support used in this study was a fumed silica (Cabosil, L90). The catalyst precursors were nickel nitrate, $Ni(NO_3)_2 \cdot 6H_2O$ (Aesar, 99 %) and ammonium orthophosphate $(NH_4)_2HPO_4$ (Aldrich, 99 %). The chemicals utilized in the study of the mechanism were dibenzothiophene (Aldrich, 99.5 %), quinoline (Aldrich, 99.9 %), benzofuran (Aldrich, 99.9 %), tetralin (Aldrich, 99.5 %), tetradecane (Jansen Chimica, 99 %), piperidine (Aldrich, 99.9 %), 2-methyl piperidine (Aldrich, 99.9 %), 3-methyl piperidine (Aldrich, 99.9 %), 4-methyl piperidine (Aldrich, 99.9 %), 2,6-dimethyl piperidine (Aldrich, 99.9 %), octane (Acros, 99%), dimethyl disulfide (Aldrich, 99 %), and ethylamine (Aldrich, 97 %), The chemicals used as gas chromatography reference samples were 1,4-pentadiene (Aldrich, 99.9 %), pentane (Aldrich, 99.9 %), 1-pentene (Aldrich, 99.9 %), 3-methyl-1,4-pentadiene (Aldrich, 99.9 %), 4-methyl-1-pentene (Aldrich, 99.9 %), 3-methyl-1-pentene (Aldrich, 99.9 %), 2-methyl-1-pentane (Aldrich, 99.9 %), hexane (Aldrich, 99.9 %), 3-methyl-1-pentane (Aldrich, 99.9 %), 2-methyl-1-pentene (Aldrich, 99.9 %), 1-hexene (Aldrich, 99.9 %), trans-2-hexene (Aldrich, 99.9 %), 1,4-hexadiene (Aldrich, 99.9 %), 3-methyl-1,3-pentadiene (Aldrich, 99.9 %), trans-2-heptene (Aldrich, 99.9 %), heptane (Aldrich, 99.9 %), pyridine (Aldrich, 99.9 %), 2-picoline (Aldrich, 99.9 %), 3-picoline (Aldrich, 99.9 %), 4-picoline (Aldrich, 99.9 %), 2,6 –lutidine (Aldrich, 99.9 %). The gases employed were He (Airco, Grade 5), CO (Linde Research Grade, 99.97 %), 0.5 % O_2/He (Airco, UHP Grade), H_2 (Airco, Grade 5), N_2 (Airco, 99.99 %), 10 % (v/v) H_2S/H_2 (Air Products, 99.999 %) and 30 % N_2/He (Airco, UHP Grade).

5.2.2 Synthesis of the catalyst

The catalyst used in this study was a nickel phosphide supported on silica, Ni_2P/SiO_2, prepared with excess phosphorus (Ni/P=1/2) and a loading of 1.16 mmol Ni / g support (12.2 wt.% Ni_2P/SiO_2). Previous studies (5,6) had shown that this composition and loading level gave high activity and stability in hydroprocessing reactions. The synthesis of the catalyst involved two steps and was described elsewhere (4, 5). Briefly, in the first step, a supported nickel phosphate precursor was prepared by incipient wetness impregnation of a solution of nickel and phosphorus components, followed by calcination. In the second step, the phosphate was reduced to a phosphide by the method of temperature-programmed reduction (TPR).

5.2.3 Characterization

The synthesized material was characterized by CO chemisorption, N_2 physisorption, and x-ray diffraction (XRD) measurements. In addition, the surface properties of the catalyst were studied using temperature programmed desorption (TPD) and diffuse reflectance infrared Fourier transform (DRIFT) measurements of the probe molecule ethylamine ($CH_3CH_2NH_2$).

Irreversible CO uptakes and surface area measurements were obtained using a flow technique (4,5). The catalyst was reduced at 723 K for 2 h in a H_2 flow prior to the measurements. Measurements on a typical spent sample were carried out after collecting the material from the reactor, washing with hexane, and reducing the catalyst as for the fresh sample. Powder XRD patterns were acquired with a Scintag XDS-2000 powder diffractometer operated at 45 kV and 40 mA, using Cu K_α monochromatized radiation (λ = 0.154178 nm).

DRIFT spectra of ethylamine adsorbed on the Ni_2P/SiO_2 and blank SiO_2 were collected using a Fourier transform infrared spectrometer (Bio-Rad Model FTS 60A) equipped with a heatable diffuse-reflectance flow cell (Spectratech Model HTEC-0030-103). Studies of the effect of temperature were performed on these samples to determine the identity and stability of the adsorbed species on the catalyst surface. The samples were finely grounded prior to loading in the high temperature environmental chamber, and were pretreated in a H_2 flow at 723 K for 2 h in the same manner as before the hydrotreating reactivity measurements. In order to simulate the chemical environment in which the reactivity and mechanism tests were performed, the spectra were measured on the samples pretreated with a gas mixture of H_2S and H_2 at conditions of reaction (sulfur concentration of 3000 ppm, 553 K) and the differences with the spectra of reduced, sulfur-free samples were analyzed. Following pretreatment, the samples were cooled to room temperature in a helium flow, and IR spectra were collected (1024 scans in the region 4000 – 400 cm^{-1}). Then pulses (~ 20 μmol) of ethylamine in a helium carrier were introduced onto the sample at room temperature. To determine the effect of temperature, the spectra were obtained after the sample was soaked for 300 s at a certain temperature (298 K, 323 K, 333 K, 343

K, 353 K, 363 K, 373 K) then cooled down to room temperature. The sample spectra were normalized with a background spectrum acquired using a blank KBr sample. The final spectra were calculated after subtraction of a reference spectrum from the one obtained before the catalysts were exposed to the ethylamine gas.

Temperature programmed desorption (TPD) of ethylamine was measured on samples pretreated in H_2S using a similar procedure as was employed in the FTIR experiments. After pretreatment, the samples were saturated with pulses (35.4 μmol) of the ethylamine at room temperature, and purged with the carrier gas for one hour before starting the temperature program. The amount of adsorption was calculated by the same method as the CO uptake measurements by integrating the areas of the pulses and calculating the differences with pulses at saturation. The temperature was raised from room temperature to 1273 K at a heating rate of 0.1368 K s^{-1} (8.2 K min^{-1}). The mass spectrometer was used to monitor the masses (2, 4, 15, 17, 18, 27, 28, 30, 31, 44) in the effluent gas during heating. The amounts of the desorbed species were calibrated by injection of known amounts of pure gases (NH_3, CH_2CH_2, $CH_3CH_2NH_2$).

5.2.4 Reactivity studies

The reactivity of piperidine and its derivatives was measured in a three-phase trickle bed reactor with a feed liquid containing 2000 ppm wt. nitrogen (piperidine or derivatives), 3000 ppm wt. sulfur (dimethyl disulfide), 2000 ppm wt. internal standard (octane), and balance aliphatics (tetradecane). The system was operated at 3.1 MPa and various temperatures with an inlet liquid flow rate of 5 cm^3/h and a hydrogen flow rate of

100 μmol s^{-1} (150 cm^3 NTP min^{-1}) corresponding to a gas-liquid ratio of 9800 SCF H_2/barrel. The detailed description of the testing system is reported elsewhere (30). Quantities of catalysts loaded in the reactor corresponded to the same amount of *ex situ* CO uptake (70 μmol). Prior to reactivity measurements, the catalyst samples were pretreated in exactly the same manner as before the CO chemisorption measurements. The experiments were long (~ 300 h). For each change in temperature, the reaction system was allowed to run for 48 h to establish steady-state. Samples were collected every 2 or 3 hours during daytime in sealed septum vials and were analyzed off-line with a gas chromatograph (Hewlett Packard, 5890A) equipped with a 0.32 mm i.d. x 50 m fused silica capillary column (CPSIL-5CB, Chrompack, Inc.) and a flame ionization detector. The results of several measurements were averaged. After several changes of operating conditions, the reactivity of the catalyst was tested at a previous condition to verify that no deactivation occurred.

Reaction products were identified by matching retention times to standards injected separately. The peak areas were calibrated with the same method described elsewhere (21). The mass balance acquired using this method was close to 100 ± 5 %.

5.3 Results

5.3.1 Properties of the catalyst

The XRD patterns of the fresh and spent samples together with the reference patterns of SiO_2, bulk Ni_2P, and a powder diffraction file standard (Ni_2P, PDF 3-953), are shown in Figure 5.5.1. The figure reveals that the fresh sample consisted of amorphous silica and finely dispersed Ni_2P (31) with a hexagonal structure (Space group: $P_{\bar{6}2m}$). The intensities of the XRD lines for the spent sample were somewhat stronger that those of the fresh material. The line-broadening of the x-ray peaks was used to calculate the average crystallite size of the samples after reaction using the Scherrer method as described elsewhere (4). Table 5.1. summarizes the characteristics of catalyst, including the specific surface area and CO uptakes of the samples.

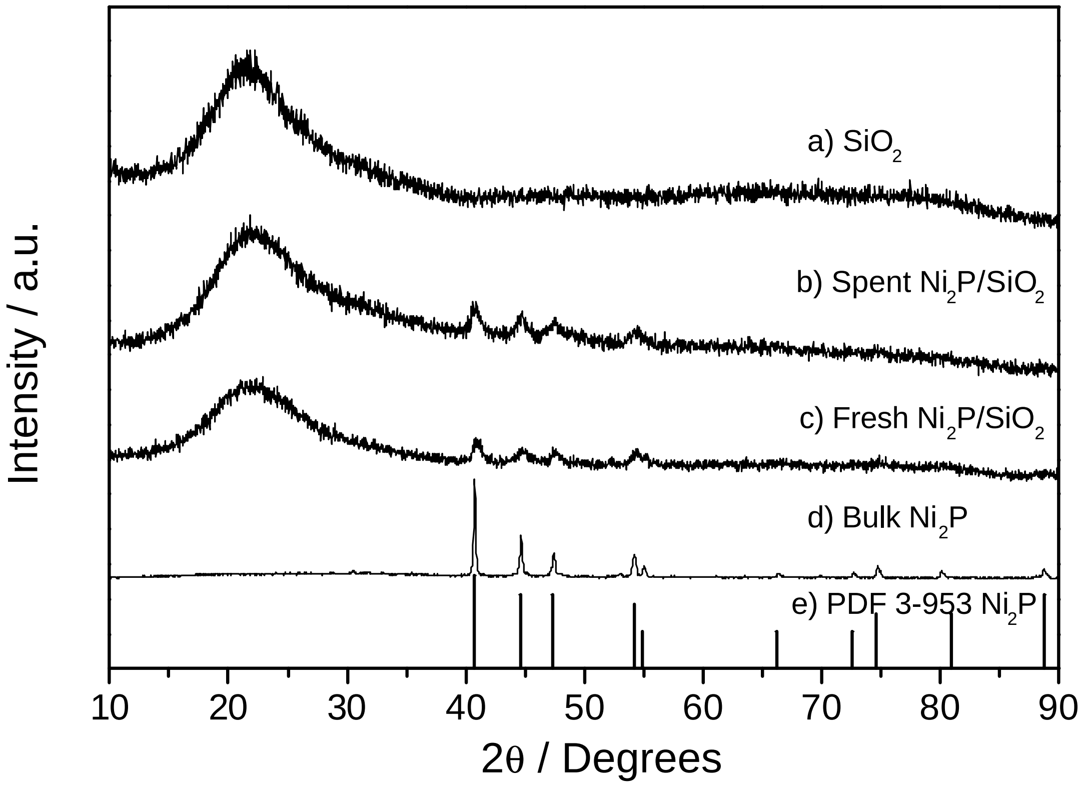

Figure 5.1. XRD patterns of both the fresh and spent Ni_2P/SiO_2

Table 5.1. Characteristics of Ni_2P/SiO_2

Ni:P Ratio	Sample	Surface area $m^2\ g^{-1}$	CO uptake $\mu mol\ g^{-1}$	D_c nm
1/2	Fresh	97	28	-
	Spent	89	24	8.7

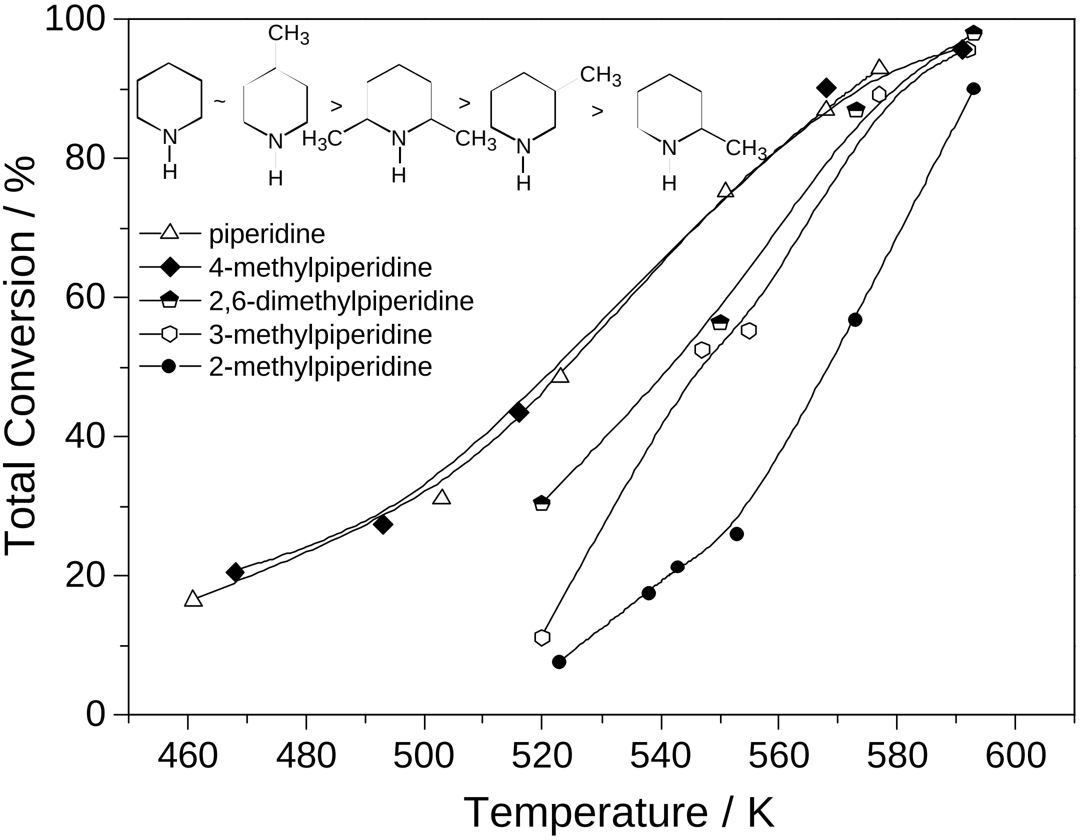

Figure 5.2. Conversion of piperidines

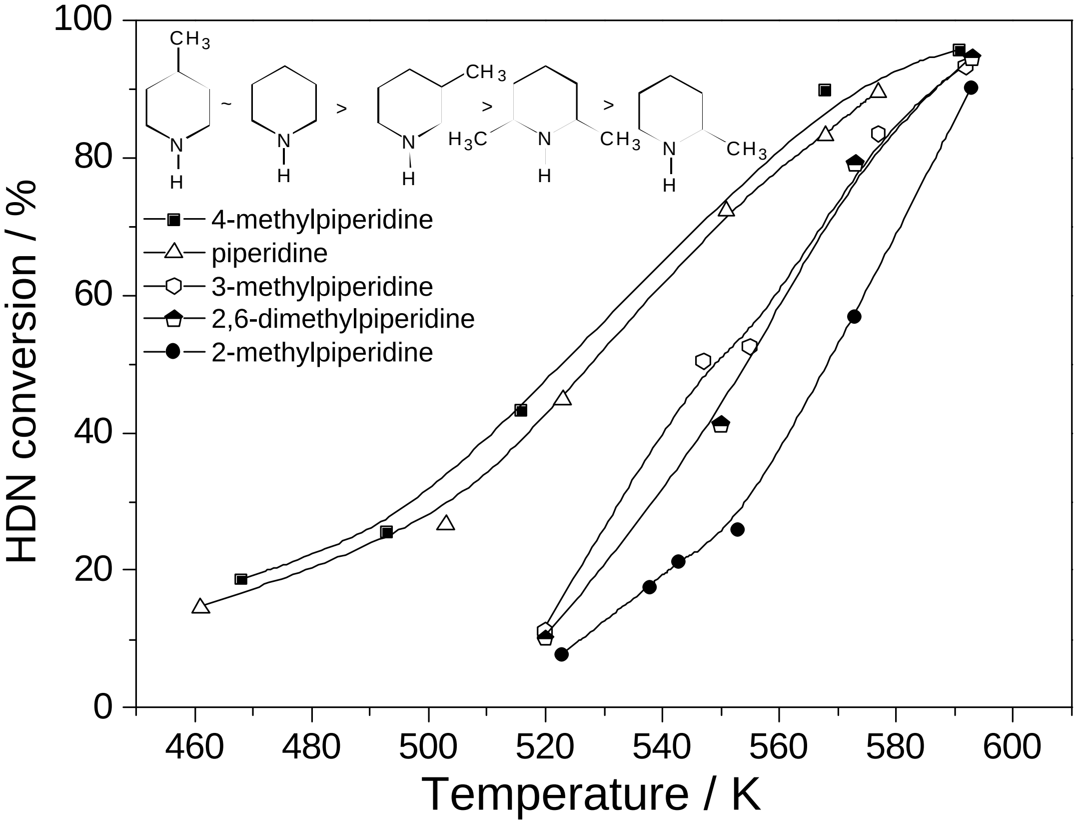

Figure 5.3. HDN of piperidines

5.3.2 Reactivity of piperidines

The total conversion of piperidines is presented as a function of temperature in Figure 5.2. The figure shows that the conversion sequence followed the order: 4-methylpiperidine ~ piperidine > 3-methylpiperidine > 2,6-dimethylpiperidine > 2-methylpiperidine. The HDN reactivity (Fig. 5.3) followed a similar sequence, with a slightly higher HDN for 4-methylpiperidine.

The selectivity and product distribution for each molecule are presented as a function of temperature in Figures 5.4-8. Figure 5.4 shows that the total conversion, HDN selectivity and product selectivities for piperidine. The conversion increased with temperature and the main product was n-pentane. The side products consisted of small amounts 1-pentene, i-C_5 compounds, C_6 compounds, condensed products, the dehydrogenation product (pyridine), and some other hydrocarbons ($< C_5$). The identification was made through comparison of retention times with model compounds. The selectivity to the HDN product increased with temperature, as expected from thermodynamic equilibrium considerations, as condensation products are not favored at higher temperature (21). The selectivity to the main hydrocarbon product pentane also increased with temperature, as expected from sequent hydrogenation reactions.

Figure 5.5 presents the total conversion, HDN selectivity and product selectivities for 4-methylpiperidine. As for piperidine, both the total conversion and HDN selectivity increased at higher temperatures. The main hydrocarbon product was 3-methylpentane while the dehydrogenation product was 4-picoline. In this case other i-C6 alkene and diene products were observed which were tentatively identified as indicated in the figure. The reference standards were not available for these, but the retention times of homologous compounds were used as guides.

Figure 5.6 presents the total conversion, HDN and product selectivities for 3-methylpiperidine. Again, conversion increased with temperature and here the HDN selectivity was uniformly high with the main hydrocarbon product being 2-methylpentane, and some of its alkene derivatives. Small amounts of its dehydrogenation product 3-picoline and condensed products were observed.

Figure 5.7 presents the total conversion, HDN and product selectivities for 2,6-dimethylpiperidine. Here, again both total conversion and HDN selectivity increased with temperature. The main product was n-heptane, but some dehydrogenation product, 2,6-lutidine was observed at low temperature. Also observed were small amounts of 1- or 2-heptene and i-C_7 compounds.

Figure 5.8 presents the total conversion, HDN and product selectivities for 2-methylpiperidine. Once again conversion increased at higher temperature and the selectivity to HDN product was uniformly high, with the main product being n-hexane. . Small amounts of 1-hexene and some i-C_6 products were also found.

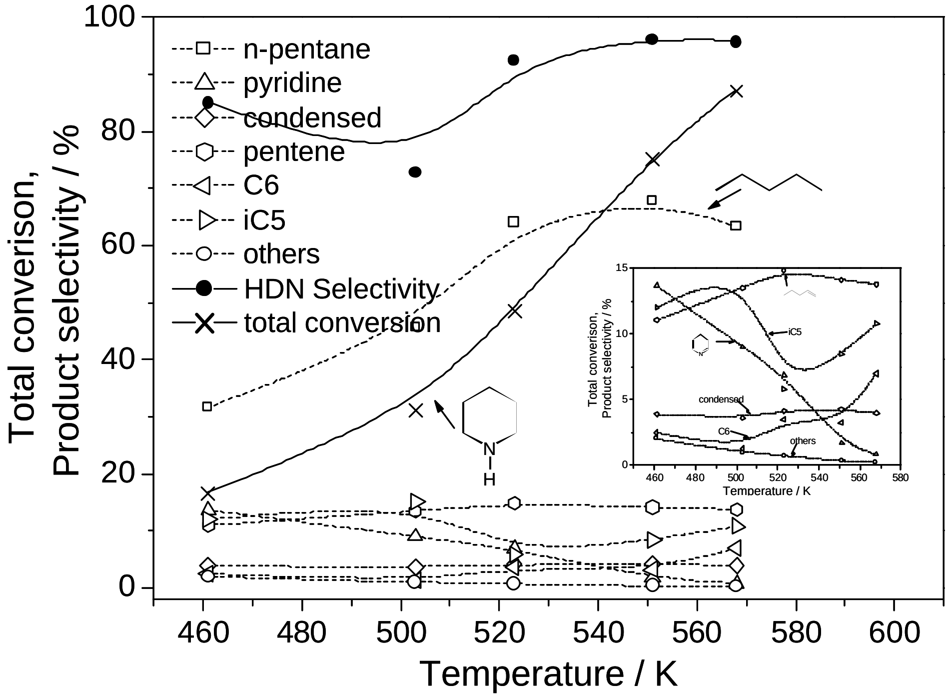

Figure 5.4. Selectivity and product distribution of piperidine on Ni_2P/SiO_2

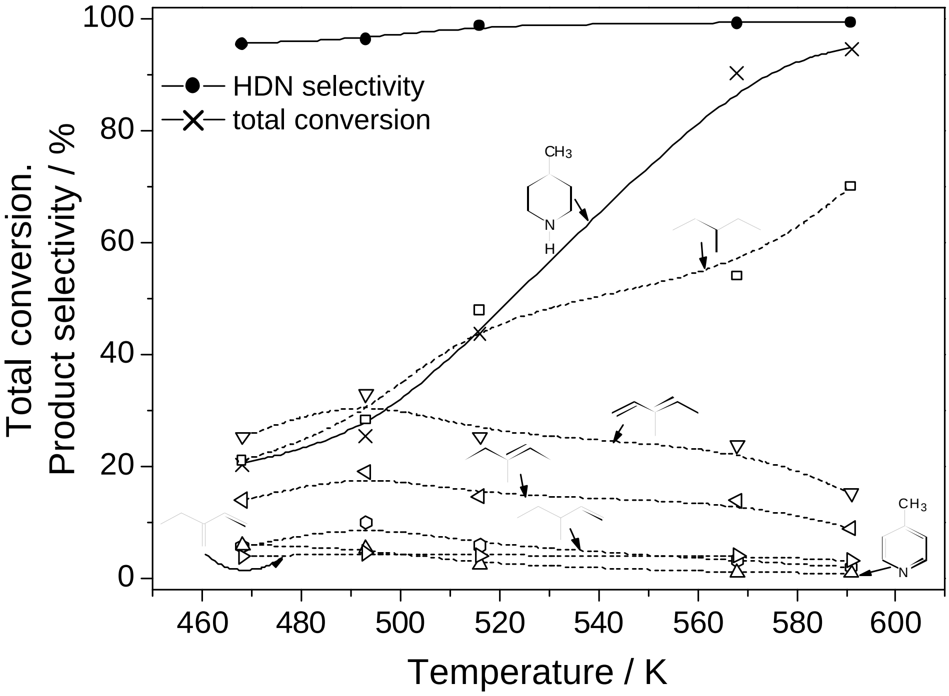

Figure 5.5. Selectivity and product distribution of 4-methylpiperdine on Ni_2P/SiO_2

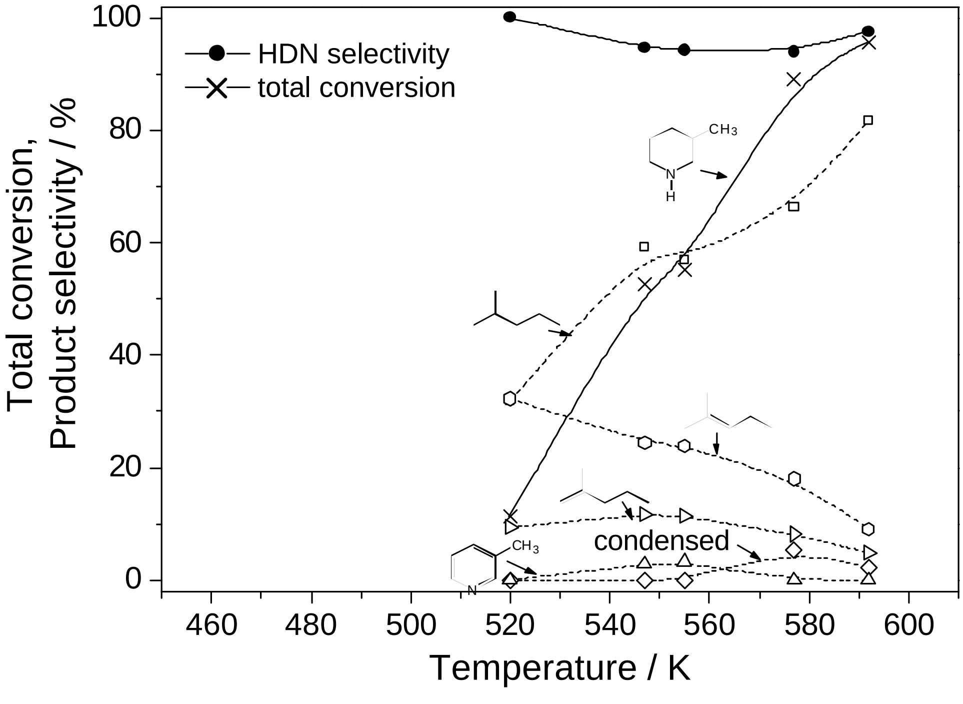

Figure 5.6. Selectivity and product distribution of 3-methylpiperdine on Ni_2P/SiO_2

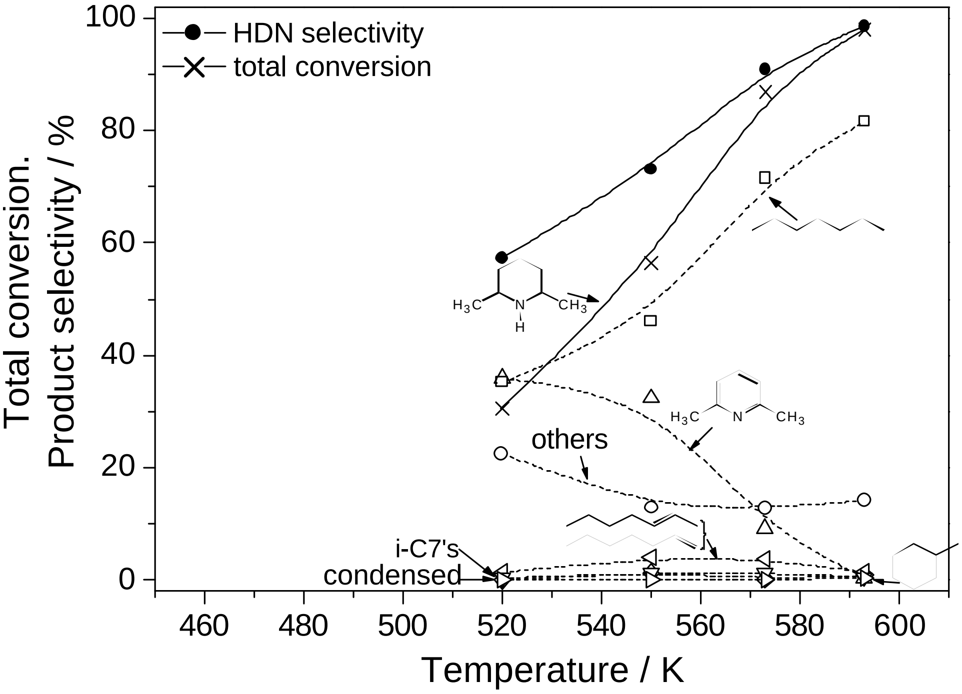

Figure 5.7. Selectivity and product distribution of 2,6-dimethylpiperdine on Ni_2P/SiO_2

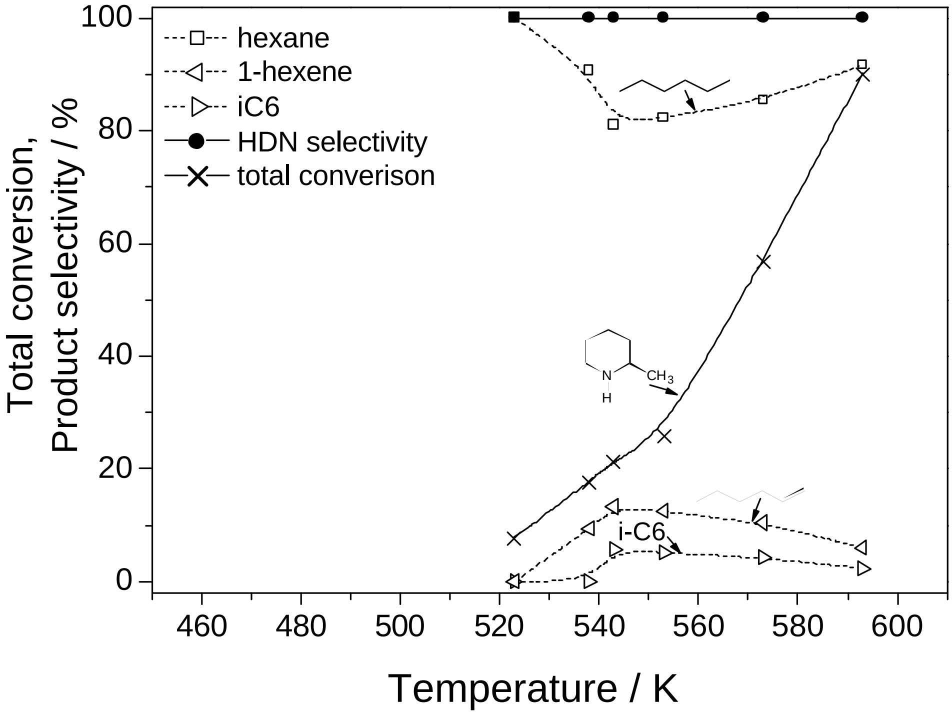

Figure 5.8. Selectivity and product distribution of 2-methylpiperdine on Ni_2P/SiO_2

5.3.3 Ethylamine FT-IR spectra

Figure 5.9 shows the spectra of ethylamine adsorbed on the blank SiO_2 support without H_2S pretreatment. The main spectral features at temperatures lower than 333 K were found between 3000-2700 cm^{-1}(2978, 2943, 2882, 2750 cm^{-1}), which correspond to CH stretching modes (32). A very weak feature was also visible at around 3340 cm^{-1} which lay in the NH stretching region. Figure 5.10 shows the spectra of the ethylamine adsorbed on the H_2S-pretreated silica support. The main spectral features were the same as those of the non-pretreated sample. The intensity of the features for both samples decreased with increasing temperature.

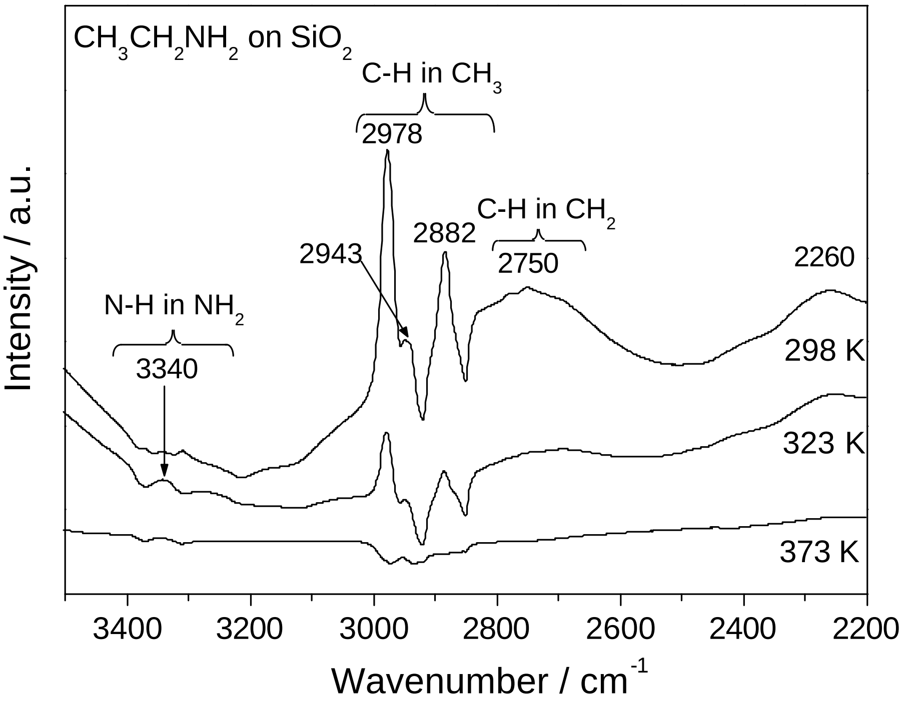

Figure 5.9. FTIR spectra of ethylamine on SiO_2 without H_2S pretreatment

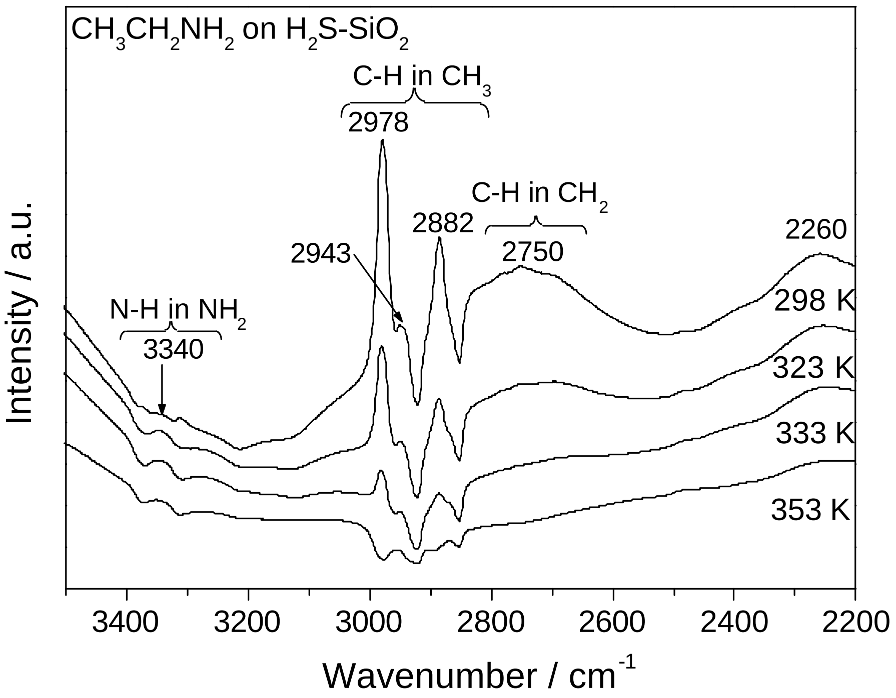

Figure 5.10. FTIR spectra of ethylamine on SiO_2 with H_2S pretreatment

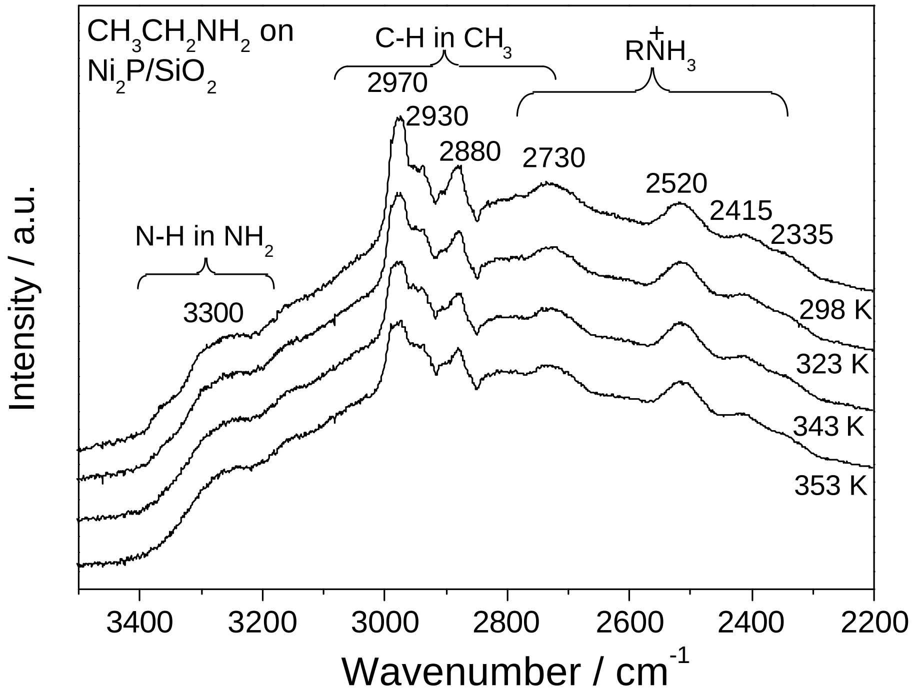

Figure 5.11. FTIR spectra of ethylamine on Ni_2P/SiO_2 without H_2S pretreatment.

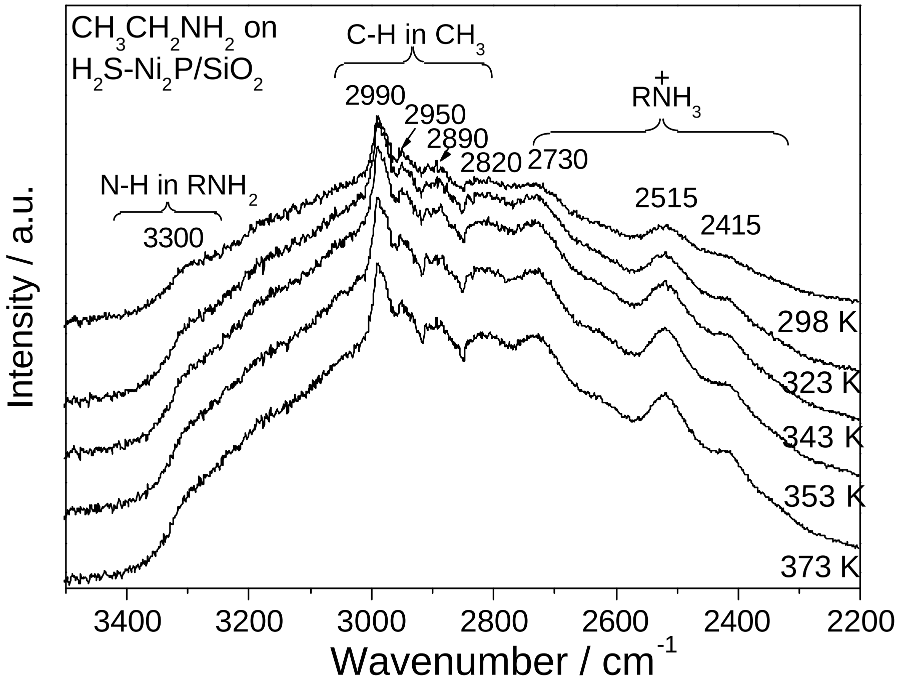

Figure 5.12. FTIR spectra of ethylamine on Ni_2P/SiO_2 with H_2S pretreatment

The results for the spectra of the ethylamine adsorbed on the Ni_2P/SiO_2 catalyst without and with H_2S pretreatment are shown in Figures 5.11 and 12, respectively. In contrast to the results on the plain SiO_2 support, from both figures it is easily seen that the spectra remain intense even above 353 K. There was a weak broad feature around 3300 cm^{-1}, which appeared to be composed of contributions from signals at 3360, 3300, and 3260 cm^{-1}. A major difference with the results on the SiO_2 support was the presence of strong bands at lower frequencies (2730, 2515, and 2415 cm^{-1}). As will be discussed, these correspond to quaternary ammonium modes (RNH_3^+) which appear between 2140-3200 cm^{-1} (33).

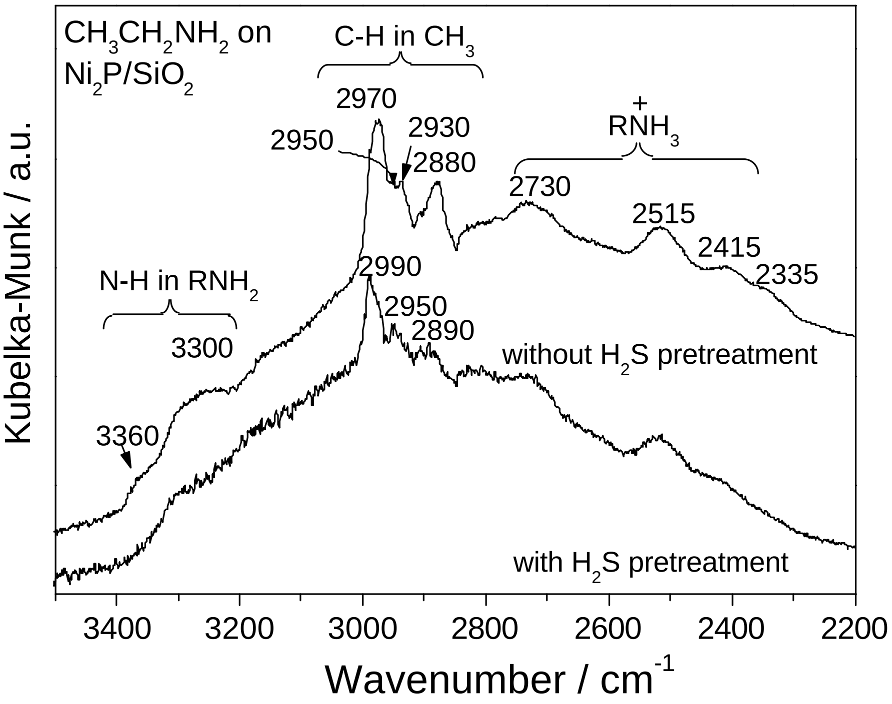

Figure 5.13. Comparison of FTIR spectra of ethylamine on Ni_2P/SiO_2 without and with H_2S pretreatment.

A direct comparison of the IR spectra at room temperature for H_2S pretreated and non-pretreated Ni_2P/SiO_2 samples is presented in Figure 5.13. It shows that the pretreated sample had much weaker features compared to the non-pretreated sample. Because of the decrease in the intensity of the spectra for the H_2S-pretreated sample it is difficult to make an exact determination, but it appears that the same spectral features are retained after the H_2S pretreatment. Peaks are observed at 3360, 3300, 2970, 2950, 2890, 2730, 2515, and 2415 cm^{-1}.

5.3.4 Ethylamine TPD result

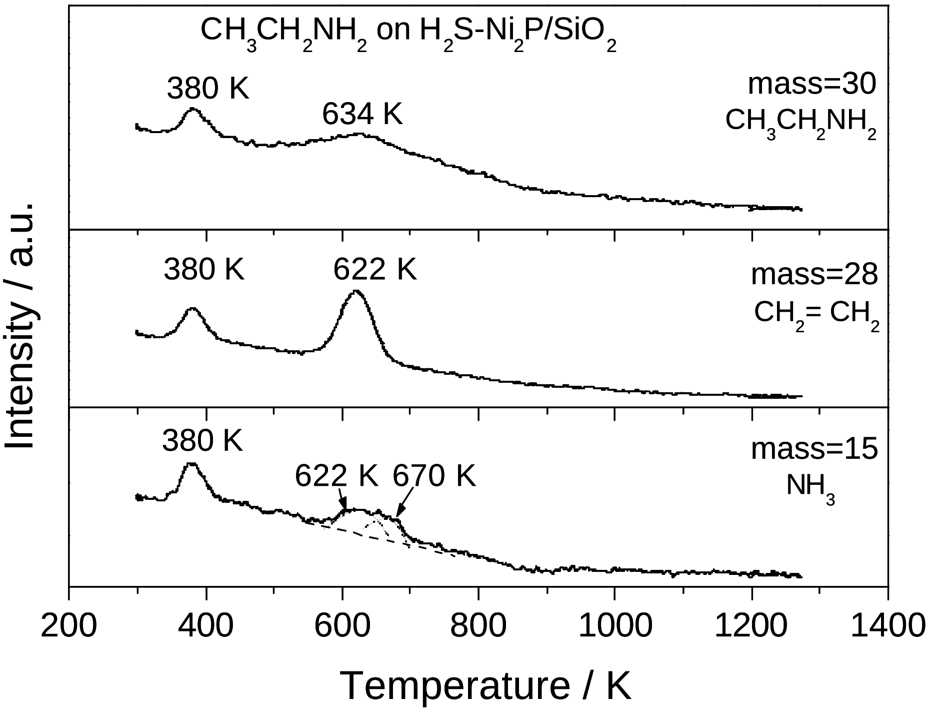

Figure 5.14. TPD curves of ethylamine on Ni_2P/SiO_2 (without H_2S pretreatment. With He as carrier gas)

Ethylamine TPD results on Ni_2P/SiO_2 are presented in Figure 5.14. The signals for mass 30, 28 and 15 were used to follow the evolution of ethylamine, ethylene and ammonia, respectively. Figure 5.14 presents the TPD result on a sample with H_2S pretreatment and H_2 as carrier gas. The conditions here were close to the actual conditions used for the reactivity study. From this figure it can be seen that the desorption features for the three masses are slightly different from each other. There are two main features at 380 K and 634 K for mass 30, two main features at 380 K and 622 K for mass 28, and three features at 380 K, 634 K and 670 K for mass 15. Integration of the peak areas and comparison to the signals for pure ethylamine, ethylene, and ammonia allowed quantitation of the desorption features. The total amount of ethylamine adsorption was determined to be 133 μmol/g catalyst. For ethylamine the contribution by physisorption was around 25 μmol/g and that by chemisorption was around 108 μmol/g. The desorbed amounts of ethylene and ammonia were 110 μmol/g and 120 μmol/g, respectively, with a ratio of 0.92.

5.4 Discussion

5.4.1 Review of reaction mechanisms for piperidine hydrodenitrogenation

HDN is a process which comprises many nitrogen removal reactions and is relatively more difficult than HDS. Generally, the hydrodenitrogenation of heterocyclic nitrogen compounds does not occur directly and is preceeded by the hydrogenation of aromatic nitrogen heterorings, before the hydrogenolysis of C-N bonds (18).

Nelson and Levy (23), Ho (11), Ledoux (34), and Hadjiloizou, et al. (17) describe several mechanisms by which amines can react. In the case of piperidine in the E2 binuclear elimination mechanism the molecule is first protonated to a quarternary ammonium species and subsequently undergoes attack by a nucleophile (B^-) on a β-hydrogen atom to form a primary amine and an olefin functionality (Scheme 5.1). The olefin is subsequently hydrogenated. This mechanism is a generalized form of the Hofmann degradation (exhaustive methylation), which involves pyrolisis of a quarternary ammonium hydroxide to form a tertiary amine and an olefin (35). The elimination occurs with an *anti* configuration between the β-hydrogen atom and the leaving amino group (29).

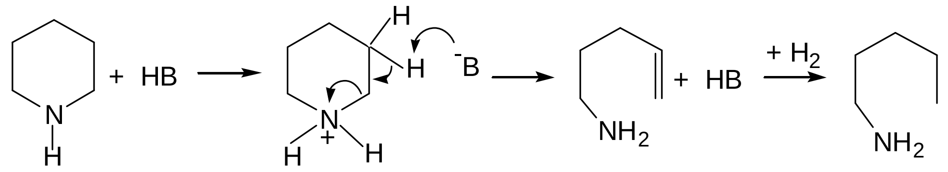

Scheme 5.1. E2 Elimination mechanism

The direct hydrogenolysis of the C-N bond in alkylamines is unlikely to occur, as the easier C-C bond hydrogenolysis reaction is not observed (19). Also the hydrogenolysis does not explain the positive effect of H_2S that has been reported in a number of HDN studies, notably by the group of Satterfield (9,36,37), but also by others (10,14,16,38). Instead, the primary amine reacts further by either another E2 elimination or, more likely, by a displacement reaction by a sulfhydryl species (Scheme 5.2). The resulting thiol does undergo a facile C-S hydrogenolysis reaction (19).

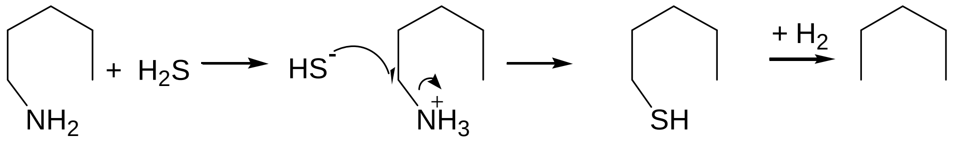

Scheme 5.2. Amine displacement mechanism

Piperidine can also react by a substitution mechanism in which attack by the nucleophile occurs on the α-carbon (Scheme 5.3). This is a binuclear nucleophilic substitution (S_N2) and results in a primary amine and incorporation of the nucleophile. The amine and the nucleophile, usually a sulfhydryl species, are subsequently removed as in Scheme 5.2.

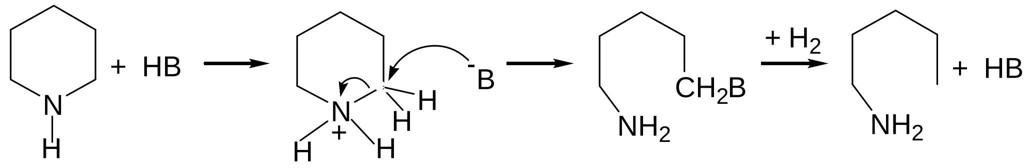

Scheme 5.3. S_N2 Nucleophilic substitution mechanism

Other possible pathways for piperidine activation are the mononuclear analogs of Scheme 5.1 and 5.3, namely the E1 and S_N1 reactions (Scheme 5.4). The reactions again start with the protonation of the nitrogen atom, but then the molecule undergoes an internal rearrangement to form a ring-opened carbocation. Loss of a proton produces the E1 product and attack by an external nucleophile (B^-) then produces the S_N1 product. Clearly, formation of the free carbocation intermediate requires a highly substituted α-carbon next to the nitrogen atom.

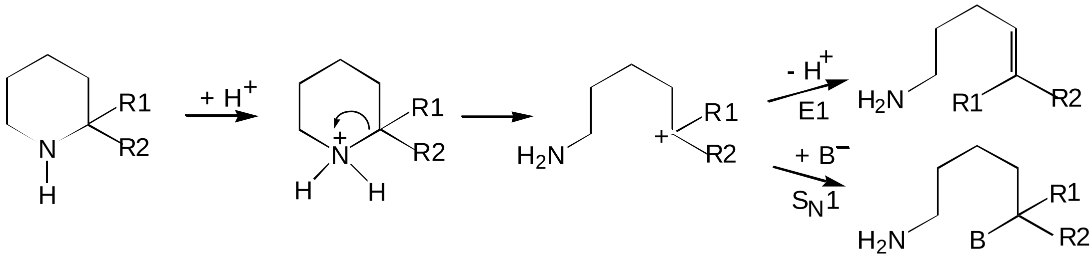

Scheme 5.4. E1 or S_N1 mechanism

The elimination and substitution mechanisms discussed above require a proton donor, and appear to be of an acid-base type. However, it has been found that pure acidic sites are not able to perform the same kind of HDN chemistry. For example, Fish, et al.

(39) reported that a zeolite was inactive for C-N bond cleavage in 1,2,3,4-tetrahydroquinoline and Ledoux and Sedrati (40) found that denitrogenation of piperidine occurred on alumina but only at elevated temperatures (651 K) and resulted in cracking reactions.

An alternative to the elimination and substitution mechanisms was proposed by Laine (41,42,43), who suggested the involvement of reactions typical of homogeneous transition metal complexes. Two pathways were proposed for piperidine ring opening. The first formed a cyclic metal alkyl species via a metalloazocyclopropane (aziridinium ring) intermediate (Scheme 5.5). This metal alkyl species can undergo hydrogenation and two reductive eliminations to restore the metal catalyst and produce pentylamine.

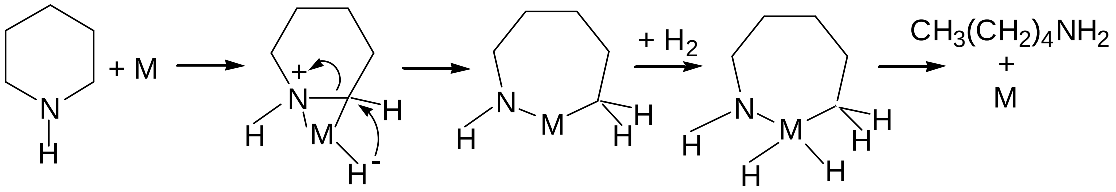

Scheme 5.5. Metalloazocyclopropane formation mechanism

The second organometallic pathway involved the formation of a metal carbene species via an iminium complex intermediate (Scheme 5.6). In this Scheme and the previous the negative charge is depicted to reside on the hydrogen atom attached to the metal to indicate the hydride nature of the complex.

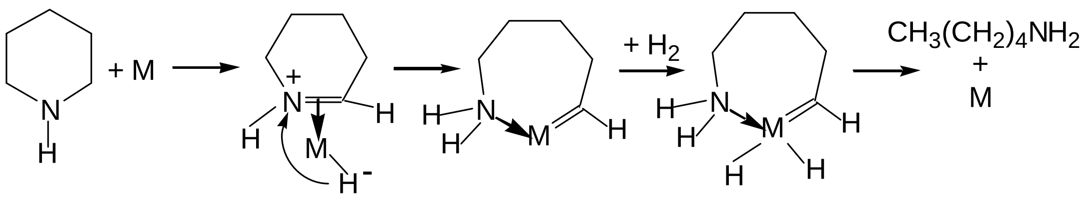

Scheme 5.6. Iminium ion complex formation mechanism

Mentioned was made earlier of the positive effect of H_2S on the HDN reaction. This was accounted for by Lane through nucleophilic attack on the iminium complex intermediate to form a thiohemiaminal (Scheme 5.7). The ring opened product can readily form the alkane.

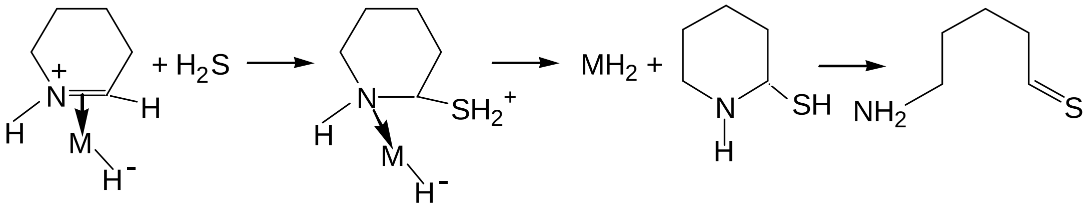

Scheme 5.7. Thiohemiaminal formation mechanism

A complication in the study of the mechanism of piperidine HDN is the occurrence of condensation side reactions. For example, Hadjiloizou, et al. (17) found considerable N-containing byproducts using a Co-Mo-S/USY-SiO_2-Al_2O_3 catalyst, although this was partly due to reactions on the highly acidic support. A number of studies report the formation of N-pentylpiperidine (44). Portefaix et al. (45) suggest the following Scheme for its formation involving an adsorbed activated piperidium complex which undergoes nucleophilic attack by a second piperidine molecule (Scheme 5.8).

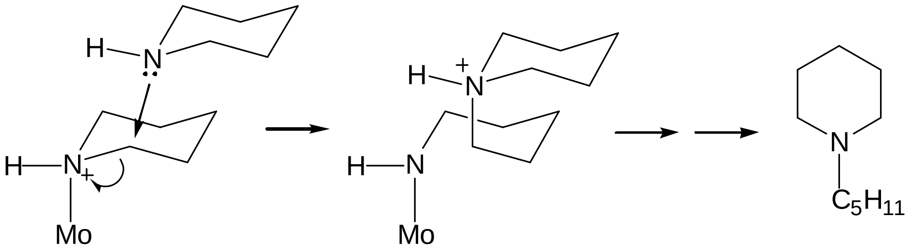

Scheme 5.8. N-pentylpiperidine formation mechanism

The intermediate on the surface that leads to condensation products can also be a Schiff's base complex (Scheme 5.9) (41,46). This can react with a surface olefin intermediate to form 2-*n*-pentylpiperidine.

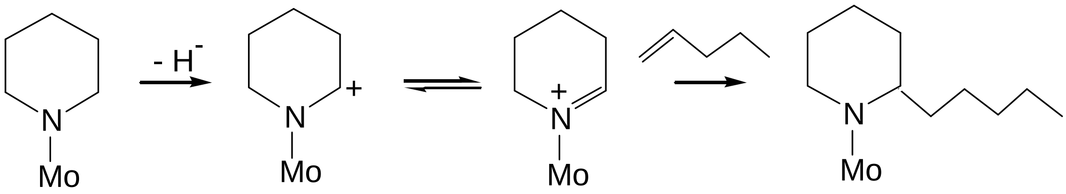

Scheme 5.9. 2-*n*-Pentylpiperidine formation mechanism

5.4.2 Test of mechanism types

The main reaction types described in the previous section can be probed by the use of substituted piperidines. There are two types of these compounds, piperidines with pendant alkyl groups (usually methyl groups), and piperidines with attached ring structures. The discussion here will be restricted to the former compounds.

A comparison of the gas-phase reactivity of several methyl-substituted piperidines was carried out by Portefaix, et al. (45). The catalyst employed was a commercial Ni-Mo-

S/Al_2O_3 and the reaction conditions were 20 bar and 548 K with 1.3 mol % of the piperidine reactant. It was found that in the presence of sulfur (1.7 mol %) the rate of formation of HDN products followed the order below (Scheme 5.10):

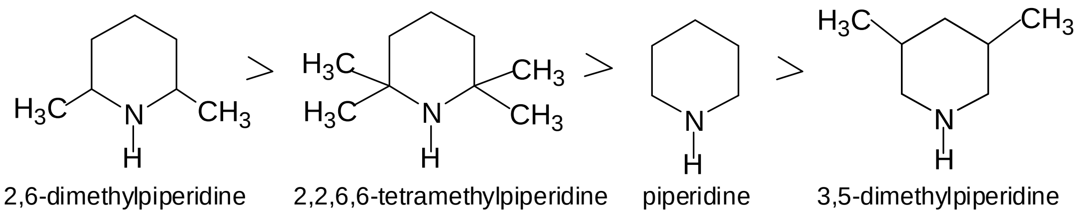

Scheme 5.10. Reaction order of methyl-substituted piperidines in sulfides

In the absence of sulfur the rate of formation of the HDN products was only slightly lower, and the same order was retained. The authors concluded that the reactivity was dominated by the number of β-hydrogen atoms in the reactant amine, and that inductive effects by the electron-donating methyl groups or steric effects were secondary. The authors suggested that HDN proceeded by a nucleophilic attack on a β-hydrogen in an elimination process (Scheme 5.1). The nucleophile could be an S^{2-} or SH^- group on the surface.

Some condensation products were observed, but except for the case of unsubstituted piperidine, these were not identified or quantified. It was qualitatively found that condensation did not correlate with the number of β-hydrogen atoms, and the authors suggested that the reaction could be bimolecular with the amine itself taking the role of the nucleophile.

5.4.3 Characterization of the catalyst

The XRD analysis of the catalyst before and after reaction indicates that the Ni_2P phase is stable at the hydrotreating conditions. Previous studies with the EXAFS technique showed a slight sulfidation of the sample (5,6), which suggested that the active surface phase during the hydrotreating reactions was probably a complex containing both S and P components.

Ni_2P/SiO_2 has been shown to be a high activity, novel hydroprocessing catalyst (4,5,6). Understanding the behavior of the adsorbed species on this sample is desirable for elucidating information about the reaction mechanism. For this purpose, FTIR measurements of ethylamine adsorption were performed on the silica support and the H_2S pretreated and non-pretreated states of this catalyst.

The FTIR results on the plain support show that ethylamine interacts only weakly with SiO_2, with most of the adsorbed species desorbing by 373 K on both the unpretreated and H_2S-treated samples (Figs. 9,10). The main bands detected are in the C-H stretching region at 2978, 2943, 2882, and 2750 cm^{-1}, with a weak band due to N-H stretching observed at 3340 cm^{-1} and a combination band at 2260 cm^{-1}(32). Previous work has shown that the N-H stretching modes are the dominant features for the ethylammonium ion, while the C-H stretching modes are the most intense features for ethylamine (47). Therefore, it is concluded that there are nearly no ethylammonium ion species adsorbed on the silica and that ethylamine is present in physisorbed molecular form. This shows that silica is a good choice as the support as it is unreactive even in presence of H_2S.

The FTIR spectra of ethylamine adsorbed on the Ni_2P/SiO_2 catalyst show little diminution of intensity with heating to 373 K, indicating a stronger interaction than with the SiO_2 support (Fig. 11). The spectra show features at low and high wavenumbers not present in the spectra from the SiO_2. At high frequency the feature close to 3300 cm^{-1} can be assigned to molecularly adsorbed ethylamine. The peaks at 2970, 2930, 2880 and 2730 are characteristic of symmetric and asymmetric C-H stretching vibrations in CH_3 and CH_2 groups (32). The peaks at 2730, 2520, 2415 and 2335 cm^{-1} are attributed to quaternary ammonium species (RNH_3^+) formed from the interaction of ethylamine with Brø nsted acid sites. The feature at 2730 cm^{-1}, which also falls in the region of C-H stretches, could be due to an N-H stretch in $R\text{-}NH_3^+$ (33). The other absorption features have been described as combination bands enhanced by Fermi resonance involving the deformation vibration of NH_3^+. Treatment with H_2S (Fig. 5.12) generally reduced the intensity of all peaks, but those due to the quaternary ammonium species persisted, and this indicates that they were the dominant species in the presence of H_2S. The overall decrease in the quantity of adsorbed species could be due to blockage of adsorption sites by sulfur.

The TPD results of ethylamine on the H_2S-treated Ni_2P/SiO_2 catalyst show features at low and high temperature corresponding to physisorbed and chemisorbed species, respectively. The physisorbed species desorb at 380 K and according to the FTIR results, probably originate from the SiO_2 support. The correspondence of the signals from mass 28 and 15 to that of mass 30 indicate that these are the result of fragmentation of the parent ethylamine molecules. At higher temperature ethylamine desorbs molecularly in a broad peak centered at 638 K. Ethylene forms a well-defined desorption peak at 622 K, whereas ammonia presents a signal with components at 634 K and 670 K. Because of the low intensity and breadth of the high-temperature ethylamine feature and overlap in desorption temperatures, the fragmentation contribution to the mass 28 and 15 signals are not clearly visible. The overall results indicate that ethylene and ammonia are desorbed sequentially with ethylene coming off first. Quantitation of the peaks indicates that the amounts of ethylene and ammonia are close to 1:1. Overall, the conclusion from this part of the paper is that ethylamine is adsorbed on the H_2S-treated Ni_2P/SiO_2 surface as an ethylammonium species which undergoes reactions. This will be related to the work on piperidines in the last section.

5.4.4 Reactivity

As presented in the review of the literature, the HDN sequence for piperidine involves two steps, first a C-N bond cleavage to form an aliphatic amine, and second, an amine group elimination to form a hydrocarbon species. The pathways available for the opening of the ring are binuclear E2 elimination (Scheme 5.1), binuclear S_N2 substitution (Scheme 5.3), mononuclear E1 elimination (Scheme 5.4), mononuclear S_N1 substitution (Scheme 5.4), and mechanisms involving metal atom mediation (Schemes 5, 6). In order to distinguish between the different routes, use was made of piperidine derivatives of different structure. As mentioned earlier the method was employed by Portefaix, et al. (45), using a different set of substituted piperidines.

Table 5.2 lists the piperidine derivatives, their properties, and the main products formed. The table shows (row 2) that the molecules differ in the number of α-H atoms they contain. Starting on the left side of the table, the first three compounds have 4 α-H’s, and the last two compounds have 2 and 3 α-H's, respectively. The table also shows that the molecules have different numbers (row 3) and types (row 4) of β-H atoms. The first two compounds each have 4 secondary β-H's, the 3-methylpiperidine has 1 tertiary and 2 secondary β-H's, the 2,6-dimehtylpiperidine has 4 secondary and 6 primary β-H's, and the 2-methylpiperidine has 4 secondary and 3 primary β-H's.

Table 5.2. Analysis of experimental results

Molecule reactivity	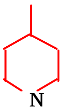	~	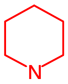	>	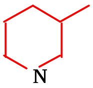	>	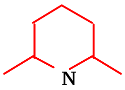	>	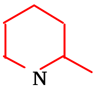
# α-H	4		4		4		2		3
# β-H	4		4		3		10		7
β-H activity	4 x 2° RH_2		4 x 2° RH_2		1 x 3° RH 2 x 2° RH_2		4 x 2° RH_2 6 x 1° RH_3		4 x 2° RH_2 3 x 1° RH_3
Steric hindrance	low		low		low		high		moderate
Carbocation stability	low		low		low		moderate		moderate
Main product	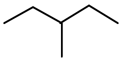		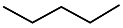		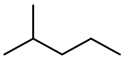		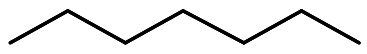		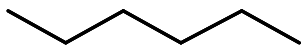

Table 5.2 also displays the degree of steric hindrance (row 5) and the stability of the carbocation formed (row 6) if the α-H were to be ionized. As can be seen, the steric hindrance around the N-atom is low for the first three compounds, but increases in the last two compounds. The stability of the carbocation is low for the first three compounds and increases for the last two compounds.

As indicated in Table 5.2 and summarized in Fig. 5.3, the order of reactivity was 4-methylpiperidine ~ piperidine > 3-methylpiperidine > 2,6-dimethylpiperidine > 2-

methylpiperidine. A number of conclusions can be derived from this order, which give considerable insight about the mechanism of denitrogenation in this class of compounds. First, it is evident that the reactivity of the compounds does not depend directly on the numbers of α-H atoms. Again, starting from the left of Table 5.2, the first three compounds have 4 α-H's, the next one has 2 α-H's, and the last one has 3 α-H's, and three molecules do not relate to the order of HDN. The reactivity of the piperidines also does not depend simply on the total numbers of β-H atoms or their type. The first two compounds have 4 β-H's, and the next compounds have 3, 10 and 7 β-H's, and irrespective of their type (1^o, 2^o or 3^o), their quantity again does not relate to the observed sequence of HDN. Clearly, the explanation for the order must lie elsewhere.

A property that would have been expected to have a large influence on reactivity is steric hindrance, but interestingly, it does not. The first three compounds have the least substitution around the N atom and duly have high activity, but the 2,6-substituted piperidine, surprisingly has a higher reactivity than the singly-substituted 2-methylpiperidine. Actually, such a result was observed earlier on sulfides by Portefaix, et al (45), who reported that 2,6-dimethylpiperidine and 2,2,6,6,-tetramethylpiperidine are more reactive than unsubstituted piperidine (Scheme 5.9). This was explained by the occurrence of exclusively and E2 mechanism.

Finally, it is clear that the experimental sequence is unrelated to the stability of the carbocations formed from ionization of the α-carbon atoms next to the nitrogen atoms. The first three compounds would form relatively unstable secondary carbocations, and the last two would form stable tertiary carbocations, but the ability to form these does not follow the trend in reactivity.

Although none of the properties described in Table 5.2 can alone account for the observed reactivity sequence, the interesting set of results described above can be explained in two manners. The first is a competition between two separate classic reactions, the S_N2 substitution and the E2 elimination. The second is a single mechanism involving activation of piperidine at both the α- and β- positions.

The first explanation rests on the assumption that the mechanism of reaction depends on the structure of the amine reactant. For unhindered molecules such as piperidine or 4-methylpiperidine reaction can proceed by a facile S_N2 substitution reaction (Scheme 5.11) to yield a ring-opened product which can subsequently undergoes denitrogenation by a route such as shown in Scheme 5.2. Substitution at the 4-position does not affect reactivity and both molecules have very similar conversion profiles. This reaction is relatively simple, requiring just the right orientation for the nucleophilic species, and is considered to occur at a high rate.

For hindered molecules with substitution at the 2- and/or 6-positions like the last two compounds in Table 5.2, the binuclear E2 elimination becomes more important. This reaction is favored by a greater number of abstractable β-H atoms, so 2,6-dimethylpiperidine which has 10 β-H's is more reactive than 2-methylpiperidine, which has only 7 β-H's. This was essentially the conclusion of Portefaix, et al (45) in their study over the sulfide catalyst. A reaction pathway is shown in Scheme 5.12.

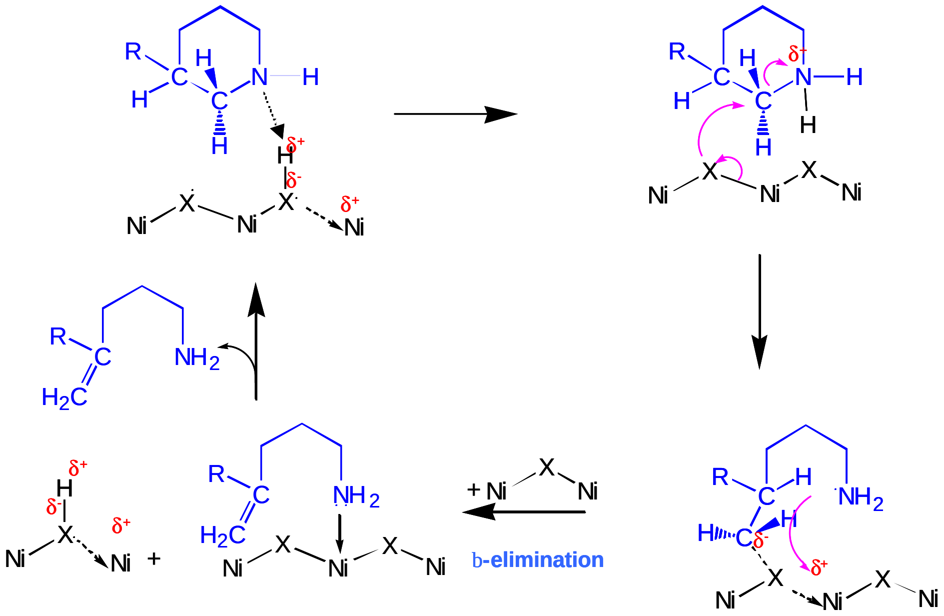

X: S or P

Scheme 5.11: S_N2 Mechanism for Piperidine on Ni_2P/SiO_2

The E1 and S_N1 mechanism do not come into play for these molecules because none can produce a tertiary carbonium ion in the α-position relative to the nitrogen (Scheme 5.4). The question arises then, what lowers the reactivity of the middle compound, 3-methylpiperidine, which should undergo as easy an S_N2 substitution as the first two compounds? The answer could be that the methyl group in the 3-position interacts with the catalyst surface causing an abstruction of the α-carbon that would normally be susceptible to nucleophilic attack. This reduces the rate of the S_N2 reaction. At the same time the H atom at 3-postiion may be made subject to abstraction. Due to its strong ionizability, as it is the only 3^o H in the whole series, the E2 reaction can proceed at a high rate. Thus, the reactivity of 3-methylpiperidine is similar to that of 2,6-dimethylpiperidine, despite the larger number of β-H's in the latter molecule.

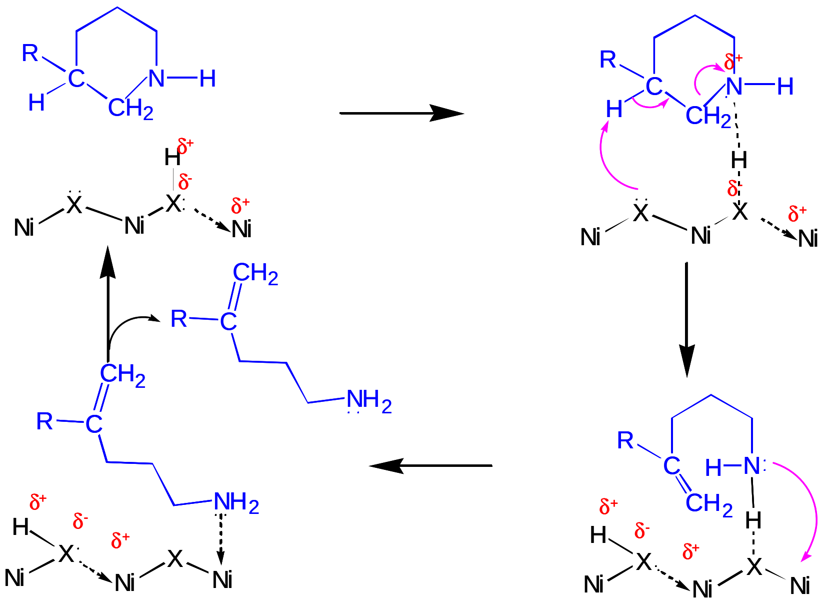

X: S or P

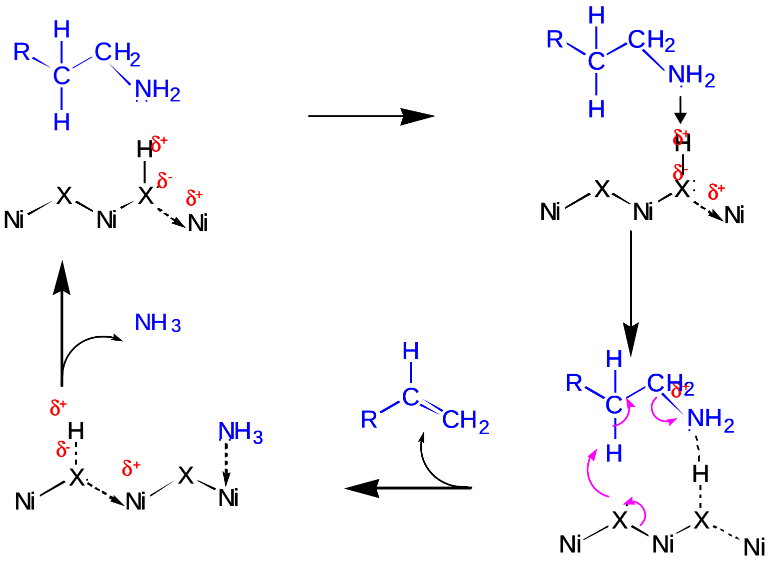

X: S or P

Scheme 5.12. E2 mechanism for piperidine and alkylamine on Ni_2P/SiO_2

The product distribution obtained with the various piperidines are all consistent with the pathways outlined above. Thus, in all cases, the primary olefins expected from the elimination of ammonia from the ring-opened products are observed. These undergo subsequent hydrogenation to the parafins, which are the most plentiful products. Where dictated by the backbone structure, various conjugated dienes or isomerization products are sometimes produced.

The interpretation of the results above is consisted with all the known facts of the reactions. However, it suffers from the drawback of requiring two separate pathways (S_N2 and E2) and of using an *ad - hoc* explanation for the reactivity of the 3-methylpiperidine. An alternative possibility is a hybrid but single mechanism operating on all reactants. This could involve the formation of one of the intermediates suggested by Laine by an α-H activation (Scheme 5.5 and 6). Such an initial step would immediately differentiate the first three unhindered molecules in Table 5.2 from the last two. The last two compounds would be the least reactive because of the smaller numbers of α-H's. The initial activation step at the α-carbon could be followed by a surface E2 elimination with reactivity depending on the numbers of β-H's and their type ($3^o > 2^o > 1^o$), and would explain the observed order. For the first three compounds the reactivity of the tertiary H would need to be higher than that of a secondary H, but not enough to overcome the statistical weight of 4 versus 2 secondary H's. For the last two compounds the reactivity would be governed by the number of 1^o H atoms alone, which is higher in the 2,6-dimethylpiperidine than in the 2-methylpiperidine.

The second explanation also fully accounts for the reactivity results. However, it is not consistent with the observation by FTIR of a quaternary ammonium ion species formed on a Brønsted site on the surface. Of course, the probe molecule in the FTIR studies was ethylamine, and its behavior on the surface may be different from that of piperidine. Clearly, a study with piperidine itself is needed to resolve this question and the measurement probably need to be done at reaction conditions. Regardless of the interpretation of the mechanism, one of the fundamental findings of this study is that the behavior of the nickel phosphide catalyst is distinct from that of the sulfides. Like the sulfides the phosphide is well able to carry out the E2 mechanism, but the phosphide also has the capability of activating the α-H's next to N atoms either by S_N2 mechanism or by a direct metal mediated reaction. This difference may account for its remarkable activity in HDN in the presence of sulfur compounds (4,5,6).

5.5 Conclusion

The mechanism of hydrodenitrogenation (HDN) of saturated nitrogen ring compounds was studied over a silica-supported nickel phosphide catalyst (Ni_2P/SiO_2, Ni/P = 1/2) in a three-phase trickle-bed reactor operated at 3.1 MPa and 450 – 600 K. The mechanism was probed by comparing the reactivity of piperidine and several of its derivatives in the presence of 3000 ppm S. The relative elimination rates depended on the structure of the molecules, and the type and number of β-hydrogen atoms, and followed the sequence: 4-methylpiperidine ~ piperidine > 3-methylpiperidine > 2,6-dimethylpiperidine > 2-methylpiperidine ,

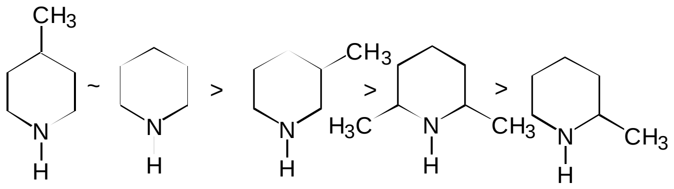

It was found that elimination of β-H atoms attached to tertiary carbon atoms occurred faster than those attached to secondary carbon atoms, and the greater the number of β-H atoms, the higher were the elimination rates. The reaction of the substituted piperidines could be explained by a dual mechanism involving S_N2 substitution for unhindered piperidines or E2 elimination for hindered piperidines. Alternatively, the results could be rationalized by a single mechanism involving activation of both α- and β- centers relative to the N atom in the ring.

Temperature-programmed desorption (TPD) and Fourier transform infrared spectroscopy (FTIR) of the probe molecule ethylamine was used to investigate the nature of the intermediates involved in the elimination step. The FTIR spectra showed that ethylamine interacted with Brønsted-acid sites on the surface to form an ethylammonium quaternary species. The effect of H_2S pretreatment suggested that sulfur species are involved in the HDN reaction. The possible mechanisms involving different sites for the piperidine HDN reaction are discussed based on the combination of reactivity data and spectroscopic evidence. It is concluded that the mechanism of HDN on nickel phosphide is different from that on sulfides and may account for the extremely high activity of this new catalyst.

References

---

1. US Environmental Protection Agency, *Press Release*, May 1, 1999, December 21, 2000.
2. Federal Register, Vol. 65, No. 28, Thursday, Feb. 10, 2000.
3. Topsøe, H., Clausen B. S., Massoth F. E., “Hydrotreating Catalysis, Science and Technology, (Anderson, J. R. and Boudart, M., Eds.), Catalysis - Science and technology”, Vol.11, Springer-Verlag Berlin Heidelberg, New York, 1991
4. Wang, X., Clark, P., Oyama, S. T., J. Catal. 2002, in press.
5. Wang, X., Requejo. F., Oyama, S. T., J. Catal. 2001, submitted
6. Wang, X., Chun W., Asakura, K., Oyama, S. T., Loading effect, in preparation
7. Whitehurst, D. D., Knudsen, K., G., Wiwel, P., Zeuthen, P., *J. Catal.*, In press.
8. Katzer, J. R., Sivasubramanian, R., *Catal. Rev.-Sci. Eng.* **20**, 155 (1979).
9. Satterfield, C. N., Modell, M., Hites, R. A., Declerck, C. J., *Ind. Eng. Chem. Proc. Des. Dev.* **17**, 141 (1978).
10. Olalde, A., Perot, G., *Appl. Catal.* **13**, 373 (1985).
11. Ho, T. C., *Catal. Rev.-Sci. Eng.* **30**, 117 (1988).
12. Kim, S. C., Massoth, F. E., *Ind. Eng. Chem. Res.* **39**, 1705 (2000).
13. McIlvried, M. G., *Ind. Eng. Chem. Proc. Des. Dev.* **10**, 125 (1971).
14. Hanlon, R. T., *Energy & Fuels* **1**, 424 (1987).
15. Kherbeche, A., Hubaut, R., Bonnelle, J. P., Grimblot, J., *J. Catal.* **131**, 204 (1991).
16. Cerný, M., Collec. *Czech. Chem. Commun.* **47**, 928 (1982).
17. Hadjiloizou, G. C., Butt, J. B., Dranoff, J. S., *Ind. Eng. Chem. Res.* **31**, 2503 (1992).
18. Perot, G., *Catal. Today* **10**, 447 (1991).

---

19. Prins, R., *Adv. Catal.* **46**, 399 (2001).

20. Cattenot, M., Portefaix, J., Afonso, J., Breysse, M., Lacroix, M., Perot, G., J. of Catal., 173, 366 (1998)

21. Schwartz, V., da Silva, V. T., Oyama, S. T., J. Mol. Catal. A, 163, 251 (2000)

22. Lee, K. S., Abe, H., Reimer, J. A., Bell, A. T., J. Catal., 139, 34 (1993).

23. Nelson, N., Levy, R. B., J. catal. 58, 485 (1979).

24. Marzari, Jorge A.; Rajagopal, S.; Miranda, Raul, Prepr. - Am. Chem. Soc., Div. Pet. Chem. (1993), 38(3), 669-70.

25. Clark, P., Wang, X., Oyama, S. T., in press

26. Marzari, J. A., Rajagopal, S., Miranda, R., J. Catal., 156, 255 (1995).

27. Jian, M., Prins, R., J. Catal. 179, 18 (1998).

28. Rota, F., Prins, R., J. Mol. Catal. A, 162, 359 (2000).

29. Rota, F., Ranade, V., S., Prins, R., J. Catal. 200, 389 (2001).

30. Ramanathan, S., Oyama, S. T., *J. Phys. Chem*., **99** (44), 16365 (1995).

31. Rundqvist, S., *Acta Chem. Scand.* **16**, 992 (1962).

32. Lin-Vien, D., Colthup, N., B., Fateley, W., G., Grasselli, J., G., The Handbook of Infrared and Raman Characteristic Frequencies of Organic Molecules, Academic Press, Boston, 1991, pp 155-178.

33. Willard, H. H.., Merritt, L. L., Jr., Dean, J. A., Settle, F. A., Jr., Instrumental Methods of Analysis, Sixth Edition, D. Van Norstrand Company, New York, 1981, Chapter 7. Page 181

34. Ledoux, M. J., in Catalysis, Vol. 7, The Chemical Society, London, 1988, pp. 125-148.

35. Hofmann, A. W., *Ber. Dtsch. Chem. Ges.* **14**, 659 (1881).

36. Satterfield, C. N., Gültekin, S., *Ind. Eng. Chem. Proc. Des. Dev.* **20**, 62 (1981).

37. Yang, S. H., Satterfield, C. N, *J. Catal.* **81**, 168 (1983).

38. Perot, G., Brunet, S., Canaff, C., Toulhoat, H., *Bull. Soc. Chim. Belg.* **96**, 865 (1987).

39. Fish, R. H., Michaels, J. N., Moore, R. S., Heinemann, H., *J. Catal.* **123**, 74 (1990).

40. Ledoux, M. J., Sedrati, M., *J. Catal.* **83**, 235 (1983).

41. Laine, R. M., *Catal. Rev.-Sci. Eng.* **25**, 459 (1983).

42. Laine, R. M., *J. Molec. Catal.* **21**, 199 (1983).

43. Laine, R. M., *Ann. N. Y. Acad. Sci.* **415**, 271 (1983).

44. Sonnemans, J., Neyens, W. J., Mars, P., *J. Catal.* **34**, 230 (1974).

45. Portefaix, J. L., Cattenot, M., Guerriche, M., Thivolle-Cazat, J., Breysse, M., *Catal. Today* **10**, 473 (1991).

46. de Angelis, F., Grgurina, I., Nicoletti, R. A., *Synthesis* **1**, 70 (1979).

47. Parrillo, D. J., Adamo, A. T., Kokotailo, G. T., Gorte, R. J., Appl, Catal., 67(1), 1990, 107-118

Chapter 6

Conclusions

A new series of hydrotreating catalysts, iron group phosphides in bulk and silica supported forms, were synthesized by means of temperature-programmed reduction (TPR) of the corresponding phosphates. The activity of the silica-supported catalysts were tested for hydrodenitrogenation (HDN) and hydrodesulfurization (HDS) with a model feed liquid. The reactivity study showed that these phosphides have great potential in the hydrotreating field. In particular, Ni_2P/SiO_2 showed better HDS reactivity than a $Ni\text{-}Mo\text{-}S/Al_2O_3$ commercial catalyst.

One important finding of this work is using excess P to modify the properties of nickel phosphide catalyst. The effect of Ni/P ratio on the structure and hydrotreating activity were studied. The results revealed that phosphorus content had a strong influence on the structure and activity of the catalysts. The crystallite size decreased with increase in P content. Both HDS and HDN were affected with P content, with the maximum value at the a Ni/P ratio of 1/2. The effect of Ni_2P loading on the silica support was also investigated in this work. The sample with a loading amount of around 18 wt.% showed the better activity.

The studies of P content and Ni_2P loading amount indicated that these quantities had a strong effect on the HDN reaction, but only a minor effect on the HDS reaction. Therefore, it is duly to conclude that the HDN reaction is structure-sensitive, while the HDS reaction is structure-insensitive.

Both XRD and Ni K-edge EXAFS were employed to identify the phases for both the spent and fresh catalysts. The results for both techniques demonstrated that Ni_2P

phase was formed, and the sample experience a small phase change after prolonged exposure to the hydrotreating test conditions. Although XPS did not reveal any S species on the spent samples, the EXAFS comparison of the spent sample and sulfide references indicated the presence of some sulfur probably on the surface of the catalysts.

The mechanism of hydrodenitrogenation (HDN) over a silica-supported nickel phosphide (Ni_2P/SiO_2) catalyst was studied in a three-phase trickle bed reactor operated at 3.1 MPa and various temperatures. The mechanism was probed by comparing the reactivity of piperidine and several of its derivatives in the presence of 3000 ppm S. It was found that piperidine activation involved α-H's in the molecule but nitrogen removal proceeded mainly by means of a β-elimination (E2) mechanism. The relative elimination rates depend on the type and number of β-hydrogen atoms. Elimination of β-H atoms attached to tertiary carbon atoms occurred faster than those attached to secondary carbon atoms. Also, the greater number of the β-H atoms, the higher were the elimination rates. Temperature-programmed desorption (TPD) of ethylamine was used to probe the acid properties of Ni_2P/SiO_2 catalysts with and without pretreatment in H_2S. The chemisorbed amount of the ethylamine and the strength of the ethylamine interaction with the acid centers on the surface of the catalyst decreased with the H_2S pretreatment. Fourier transform infrared spectroscopy (FTIR) indicated that H_2S pretreatment decreased the amount of both Brønsted and Lewis acid-sites. The effect of H_2S pretreatment suggested that sulfur species were involved in the HDN reactions. It was concluded that both Brønsted and nucleophilic sites participated in the HDN reactions. In this work, a possible mechanism involving different sites was proposed for the piperidine HDN reactions.